金属粒子を担持した酸化亜鉛粒子の生成と有機染料分解機能の評価

Generation of metal-supported ZnO-based particles and evaluation of photocatalytic properties for organic dye treatment

金属粒子を担持した酸化亜鉛粒子の生成と有機染料分解機能の評価

A Thesis Presented to the Faculty of Engineering

Muroran Institute of Technology

by

Young-Jun LEE

September 2021

Abstract

Synthetic dyes are used in industries such as petrochemical, dyeing, paper, and pulp, but contain harmful substances that can damage the natural environment. The main consumption industry of synthetic dyes is the textile industry, and a large amount of dye is lost to wastewater during the coloring process of the textile. As the global population increases and the demand for textiles increases, the amount of wastewater discharged from synthetic dyes is also increasing, which is a major cause of the recent pollution problem. Because synthetic dyes have various chemical properties, it is not easy to treat with conventional wastewater treatment methods such as adsorption, filtration, coagulation, membranes, etc. Therefore, the development of eco-friendly, high-efficiency, low-cost organic pollutant treatment methods has become an important task for researchers.

Recently, photocatalytic oxidation of organic pollutants has been proposed as a promising alternative. Photocatalytic oxidation treatment can photodegrade organic pollutants into H_2O, CO_2, and inorganic substances without generating toxic secondary substances, as well as remove odors and disinfect them. However, the main drawback of semiconductor photocatalysts is the reduced efficiency due to the rapid recombination of excited electron-hole pairs. When a noble metal is supported on a photocatalyst, a noble metal acts as an electron sink and delays the recombination of the excited electrons and holes, so the efficiency of the photocatalyst can be improved. Moreover, another drawback of photocatalytic treatment is that it is very difficult to recover photocatalysts after removing organic pollutants from wastewater, and reuse is greatly limited. Therefore, in this study, an experiment was performed to improve the photocatalytic properties by supporting Ag or Au on the ZnO photocatalyst, and the magnetic properties of the particles were also observed through Fe_3O_4 support.

Nanoparticles show good photocatalytic efficiency because of their large specific surface area but have the disadvantage of being difficult to recover after use. In addition, the wet method requiring post-treatment may reduce the photocatalytic efficiency due to agglomeration between particles. Therefore, there was a need for a method that could produce submicron-level particles without agglomeration in a single process. In addition, there was a need for a generation method that could increase the efficiency of the photocatalyst by supporting the noble metal as a single crystal. The ultrasonic spray pyrolysis method is a method that meets these requirements. Therefore, in Chapter 2, Au/ZnO particles were generated using the ultrasonic spray pyrolysis method. The Au/ZnO

particles produced using the USP method showed structural patterns of ZnO and Au. TEM images showed dark spots dispersed throughout the Au/ZnO particles. EDX mapping and STEM images confirmed that the dark spots corresponded to nano-sized Au particles dispersed throughout the ZnO particles. The photolysis of organic Rhodamin B (RhB) aqueous solution was investigated under UV light irradiation. Under all conditions, Au/ZnO particles showed better photocatalytic activity than ZnO particles. The best photocatalytic activity was observed in particles with a 0.1 mass% Au supported on ZnO particles. Moreover, the USP could simply generate particles in one step. Although decomposition experiments on actual wastewater were beyond the scope of this study, the potential of purifying organic pollutants using this material was confirmed.

Precious metals such as Au are expensive, so industrial applications can have significant limitations. Therefore, relatively inexpensive Ag carrying research is attracting attention. Therefore, in Chapter 3, Ag/ZnO particles were generated using the ultrasonic spray pyrolysis method. The resulting Ag/ZnO particles were spherical and had a size of 0.5 to 1.0 μm, and there was no change in shape by the Ag support. ZnO and Ag crystal peaks were observed in all Ag/ZnO particles. In the TEM image, dark spots dispersed in Ag/ZnO particles were confirmed, and the size of the dark spots varied according to the concentration of added silver nitrate. EDX mapping and STEM images confirmed that these dark spots correspond to Ag particle nanoparticles dispersed throughout the ZnO particles.The photocatalytic activity of the generated particles was investigated by photolysis of the RhB aqueous solution under UV irradiation. All Ag/ZnO particles showed better photocatalytic activity than ZnO particles. Particularly, the particles with 0.2 mass% silver nitrate supported on ZnO particles showed 2 times better photolysis activity than P25. It was observed that the particles generated could not only be recovered simply by gravity sedimentation after the photolysis experiment but also had a slow deterioration rate. Using the USP method, we were able to easily generate submicron-level complex particles and confirmed the possibility of purifying and reusing organic pollutants.

The application of photocatalyst to organic dye treatment is that it is difficult to recover fine photocatalyst particles from photolysis treated wastewater. Methods such as filtration or centrifugation for particle recovery can cause destruction and loss of particles, resulting in high operating costs and secondary pollution. Therefore, there is a need for a study that can simply recover the particles. The combination of photocatalyst and magnetic particles can be a reliable solution. When the photocatalyst and magnetic particles such as magnetite (Fe_3O_4) are combined, not only can

the particles be easily recovered through the magnetic separation process, but also can be recycled. Several methods are used for the synthesis of ZnO/Fe_3O_4. In Chapter 4, the synthesis of ZnO/Fe_3O_4 and ZnO/Fe_3O_4/Ag composite materials was attempted through ultrasonic spray pyrolysis and co-precipitation methods, and the physical properties of the resulting particles were confirmed.

When the ultrasonic spray pyrolysis method was used as a single method, crystal peaks of the target products ZnO and Fe_3O_4 were not observed. However, under certain conditions, a single crystal peak of $ZnFe_2O_4$ was identified. Because the metal reactivity of Zn and Fe is similar, it precipitated as $ZnFe_2O_4$ single crystal during pyrolysis process. Studies on $ZnFe_2O_4$ particles have been reported, but due to the low bandgap, it is not suitable for organic matter treatment. When the ultrasonic spray pyrolysis and co-precipitation methods were used together to generate particles, crystals of the target products, ZnO and Fe_3O_4, were observed. Although the magnetic properties of the particles were observed, uncoated ZnO particles were identified. Therefore, it was confirmed that the surface modification using sodium citrate is not suitable for the formation of ZnO/Fe_3O_4 composite particles. When co-precipitation was used as a single method, crystals of the target products ZnO, Ag, and Fe_3O_4 were observed. In the photolysis experiment, it was confirmed that the photolysis properties of the ZnO/Fe_3O_4 composite particles were not good compared to the pure ZnO particles. However, although the ZnO/Fe_3O_4/Ag composite particles contained Fe_3O_4, the photodecomposition properties were superior to those of pure ZnO particles. The optimal condition was when 0.2 mass% silver nitrate was added, which is consistent with the results of Chapter 3. The co-precipitation single method confirmed some agglomeration of particles, but it was judged to be most suitable for the generation of ZnO/Fe_3O_4 and ZnO/Fe_3O_4/Ag composite particles.

Generation of metal-supported ZnO-based particles and evaluation of photocatalytic properties for organic dye treatment

by Young-Jun LEE

Chapter 1 Introduction

1.1. Background

Natural dyes extracted from fruits, vegetables, flowers, insects, etc. have been used since 3500 BC and are also found in historical records. However, natural dyes could not meet the required demand due to the limited color spectrum and production. Thus, in 1856, W. H. Perkins developed synthetic dyes with a broader spectrum of colors and providing lighter shades to replace natural dyes and are still in use today [1]. These synthetic dyes are used in industries such as petrochemical, dyeing, paper, and pulp, but contain harmful substances that can damage the natural environment [2-3]. For example, wastewater containing synthetic dyes mainly contains carcinogens such as nitro, sulfo, chloro, naphthalene, benzamine, and other aromatic compounds, which adversely affect human health, the environment, and aquatic ecosystems [2, 4-6]. The main consumption industry of synthetic dyes is the textile industry, and a large amount of dye is lost to wastewater during the coloring process of the textile. It is estimated that more than 15,000 dyes and pigments are produced worldwide, and more than 900,000 tons are used [7]. Due to the inefficiency of the dyeing process, 200,000 tons of dye, which is about 1-20% of the world's dye production, are discharged into wastewater [2, 7, 8]. Therefore, the International Organizations for Environmental Protection has set an acceptable standard for environmental emission of organic dyes at a level of a few micrograms per liter [9].

As the global population increases and the demand for textiles increases, the amount of wastewater discharged from synthetic dyes is also increasing, which is a major cause of the recent pollution problem. This is because conventional wastewater treatment methods such as adsorption, filtration, coagulation, membranes, etc. cannot decompose pollutants, but also cause secondary pollution by simply moving organic pollutant molecules to another medium [3, 8, 10]. It is also very difficult to treatment synthetic dyes with high thermal and light stability [2, 8]. Therefore, the development of eco-friendly, high-efficiency, low-cost organic pollutant treatment methods has become an important task for researchers.

About 72 toxic chemicals have been identified in wastewater from the textile industry, of which 30 cannot be removed [1]. If the wastewater contains a high concentration of dye, the oxygen saturation of the water decreases and sunlight is blocked, which interferes with photosynthesis of aquatic plants such as algae [1, 10]. In particular, because these dyes are not biodegradable, they accumulate in

ecosystems and aquatic organisms. So it could potentially be a problem for human health as well [11]. Because of these hazards, it is necessary to separate and remove residual dyes from wastewater and actively work in industrial sites. However, because synthetic dyes have various chemical properties, it is not easy to treat with conventional treatment methods. In particular, toxic substances can be produced by weathering organic dyes in wastewater through oxidation, hydrolysis or other chemical reactions [8].

1.2. Type of organic dye

In general, dyes can be divided into three categories: anionic (acidic and reactive dyes), cationic (alkaline dyes) and nonionic (disperse dyes). A large number of chemically different dye groups such as azo, disperse, acidic, alkaline and triphenylmethane were used for textile dyeing. Among them, azo dyes (anionic) with nitrogen-nitrogen double bonds (N = N) are considered the most used organic dyes, but their treatment is complicated due to their aromatic structure and difficult decomposition properties. Examples of some of the dyes mainly used commercially are shown in Table 1-1.

1.2.1. Congo red (CR)

These are the most used azo dyes worldwide. The CR is a benzidine-based anionic azo dye containing nitrogen-nitrogen double bonds (-N = N-). The complex aromatic molecular structure of CR dyes provides optical, thermal, and physicochemical stability, so their main applications are in the textile, printing, dyeing, paper, rubber, and plastics industries. The toxic of CR benzidine could cause mutagenicity and carcinogenicity in humans. Also, frequent touch of this dye can cause an allergic reaction. Therefore, it is very important to remove the remnants of the CR before mixing it with the water source. Although CR dyes have been banned in many countries due to health concerns, they are still widely used in many countries [12].

1.2.2. Crystal violet (CV)

Crystal Violet, a triphenylmethane-based dye, is widely used in the textile processing industry and in biological dyeing in human medicine. However, since CV is a recalcitrant dye, it remains in the environment for a long time and is therefore toxic to terrestrial and aquatic organisms. The CV has been reported to cause problems in the reproductive system of rabbits and fish, and is known as a powerful carcinogen that promotes tumor growth in biological cells. Inhalation of CV can cause

irritation of the respiratory tract, and ingestion can cause gastrointestinal problems. It can be seen from the chemical structure of the dye that there is an aromatic ring in three directions attached to the central carbon atom, and it has a maximum absorption peak of 584 nm, so it is purple. The CV is widely used in analytical chemistry laboratories as a pH indicator for testing the pH range from 0 to 1.6. At low pH, the CV turns yellow and becomes blue-violet at the alkaline end [13-14].

1.2.3. O-Phenylenediamine (OPD)

O-Phenylenediamine (OPD) called 1,2-diaminobenzene or 1,2 phenylenediamine, is an aromatic amine used as a dyeing material for polymers, drugs, and textiles. However, OPD has been shown to be harmful by ingestion, inhalation, and eye contact and can cause cancer cells. Therefore, excessive exposure to OPD can damage the respiratory, digestive and liver and lead to cancer. These OPD are considered one of the serious environmental pollutants due to their toxicity and carcinogenicity. Because OPD is water soluble, it can easily contaminate ground and surface water, and it is very important to monitor OPD in drinking and environmental waters [15-16].

1.2.4. Rhodamine 6G (Rh6G)

Rhodamine-based dye, a highly recalcitrant textile dye, commonly used for coloring cotton, wool, silk, and paper. In addition, Rh6G is also used as a diagnostic tool to detect antigens and has excellent staining properties in dark reddish purple. The Rh6G is also used in fluorescence microscopy and fluorescence correlation spectroscopy in biotechnology. However, water with rhodamine dye causes irritation to human skin, eyes, and respiratory system. And, unfortunately, Rh-6G is toxic and carcinogenic to cells and tissues in organisms, and is associated with mutagenicity and teratogenicity. Some studies have demonstrated that drinking water contaminated with R6G causes serious damage to retinal ganglion cells [17-18].

1.2.5. Rhodamine B (RhB)

It is a reddish-purple powder of xanthene class with high water solubility used under the brand name D & C Red No. 19. The RhB is widely used as a colorant. However, if swallowed by humans and animals, it is harmful and causes irritation to the skin, eyes and respiratory system. It has been medically proven that drinking water contaminated with RhB dye can cause highly carcinogenic tumors. In recent years, carcinogenicity, reproduction, development, neurological and chronic toxicity

to humans and animals have been intensively investigated and proven [19-21].

1.2.6. Phenol red (PR)

It exists as red crystals and is a textile dye that belongs to the triphenylmethane dye class. A commonly known synonym for phenol red is phenol sulfonephthalein. Since it is stable in water and air and has a pH range of 6.8 (yellow) to 8.2 (bright pink), it is often used as a reagent for measuring the pH of water and cell biology laboratories. It has been reported that PR inhibits the growth of renal epithelial cells and has a lethal toxicity that causes mutations in muscle fibers. In addition, direct or indirect contact may cause skin, eye, and respiratory irritation [22-23].

1.2.7. Methylene blue (MB)

It is a dark green cationic dye, and the aqueous solution has a blue color. It is widely used for dyeing paper, coloring, wool, silk leather, and paper coatings. Although MB is considered harmless compared to other synthetic dyes, it can also cause some detrimental effects such as cyanosis, vomiting, increased heart rate, limb paralysis, shock, jaundice and human tissue necrosis [24].

1.2.8. Malachite green (MG)

In addition to being used in the dyeing process, it has also been used as an antibacterial agent to prevent fungal infections in fish farms. However, it can persist for a long time in edible fish tissues and bioaccumulate in terrestrial and aquatic ecosystems, which has a detrimental effect on the environment and human health. Also, due to its toxicity and carcinogenic effects, the U.S. Food and Drug Administration (FDA) designated MG as the preferred chemical for carcinogenicity testing by the National Toxicology Program in 1993. The use of MG has been banned worldwide since 2002, but it is still used in some environments [24-26].

1.2.9. Other dyes

In addition, Janus Green B (JGB), Janus Green B (JGB), Alizarin Red S (ARS), methyl orange (MO), methyl red (MR), methyl red (MR), indigo carmine (IC), eriochrome black T (EBT), eriochrome blue black T (EBBT), alizarin cyanin green (ACG), victoria blue B (VBB), methyl violet (MV), reactive red 195 (RR-195), etc. Likewise, toxicity has been reported.

Table 1-1 Some Examples of Commercial Dyes.

Dyes	Structure	Chemical formula	M_w
CR	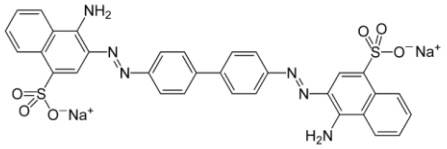	$C_{32}H_{22}N_6Na_2O_6S_2$	696
CV	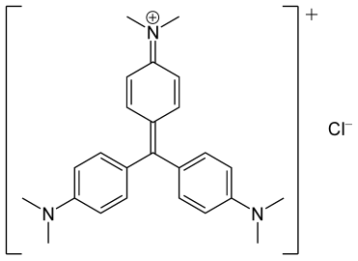	$C_{25}H_{30}ClN_3$	408
OPD	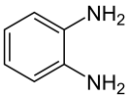	$C_6H_4(NH_2)_2$	108
Rh6G	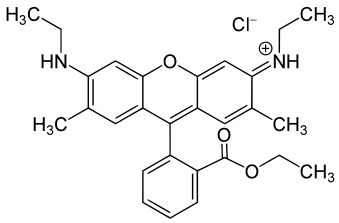	$C_{28}H_{31}N_2O_3Cl$	497
RhB	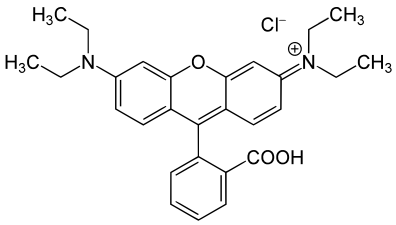	$C_{28}H_{31}ClN_2O_3$	497
PR	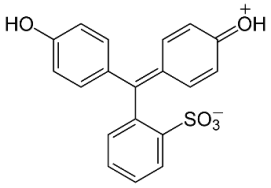	$C_{19}H_{14}O_5S$	354
MB	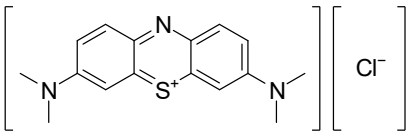	$C_{16}H_{18}N_3SCl$	320
MG	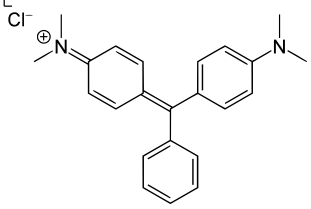	$C_{23}H_{25}ClN_2$	365

1.3. Conventional removal method for synthetic dyes

Wastewater treatment methods can be classified into physical, chemical, and biological methods as shown in Table 1-2. Proprietary treatment by one of these three methods has proven insufficient to remove organic dyes from textile wastewater. The same process may not apply to other types of colored wastewater, even if some processes have reported successful decolorization of certain wastewater [1]. Some processes, such as electrochemical technology and ion pair extraction, are relatively new treatments for textile wastewater treatment, while others have long been used in the industry. Each process has its own limitations in terms of cost, feasibility, reliability, stability, environmental impact, sludge treatment, operational difficulties, pretreatment requirements, organics removal range and potential toxic by-products.

Table 1-2 Wastewater treatment method.

Physical	Chemical	Biological
Absorption	Oxidation	Aerobic
Filtration	Reduction	Anaerobic
Reverse Osmosis	Catalysis	
Membrane Treatment	Ion Exchange	
	Electrocoagulation	
	Coagulation	
	Chlorination	
	Ozonation	

1.3.1. Physical and chemical removal method

1.3.1.1. Absorption

Removal of organic dyes by adsorption has been regarded as one of the best existing methods. The most used activated carbon is known for its excellent adsorption capacity for a variety of aqueous and gaseous pollutants. In addition, porous materials such as ceramic, fly ash, sepiolite, hydrogel, clay minerals, hydrotalcite, perlite, biopolymers such as chitosan, and agricultural by-products can be used to move pollutants to the surface of the adsorbent. The adsorption capacity and cost of adsorbents differ for each material, and the adsorption capacity differs depending on the surface area, PH, and temperature. In addition to the most widely used activated carbon, agricultural waste such as sugar cane, rice husk, and wood sawdust can be used and has an adsorption efficiency of 40-90%. These materials can be used extensively because of their low cost, but they are less efficient than activated

carbon and require large amounts [22, 24, 27-28].

The use of activated carbon systems, including the regeneration of adsorbents, is too expensive. Particularly, large dye molecules adsorbed on the surface of the adsorbent are difficult to desorb due to the strong chemical bond between the adsorbent and the dye, so regeneration cost is high and impractical. Therefore, disposal of used adsorbent creates additional problems. Also, certain adsorbents can only be applied to certain types of dyes. For example, negatively charged adsorbents have a high adsorption capacity for cationic dyes. Therefore, using only one type of adsorbent is difficult to deal with the complex composition of dye waste.

1.3.1.2. Filtration process

Ultra-filtration (UF) [28-30]

Ultra-filtration can remove macromolecules and large particles, but does not completely remove contaminants such as dyes. Even in the best case, the quality of the treated wastewater does not allow reuse for sensitive processes such as fabric dyeing. The Ultra-filtration can be used for pretreatment for reverse osmosis or in conjunction with biological reactors. The UF membranes are made of polymeric materials such as polysulfone, polypropylene, nylon-6, polytetrafluoroethylene (PTFE), polyvinyl chloride (PVC), acrylic copolymer, etc.

Micro-filtration (MF) [28-30]

Micro-filtration can also be used as a pretreatment for nanofiltration or reverse osmosis. The suspended solids, macromolecules and colloids floating in wastewater can be separated. The MF membrane is made of specific polymers such as Poly (Ether Sulfone), Poly (Vinylidiene Fluoride), Poly (Sulfone), Poly (Vinylidene Difluoride), Polycarbonate, Polypropylene, Poly Tetrafluoroethylene (PTFE), etc. Ceramic, glass, carbon, zirconia coated carbon, alumina and sintered metal membranes with excellent chemical resistance have been used where high temperature operation is required.

Nano-Filtration (NF) [28-30]

Nano-Filtration membranes are usually made of cellulose acetate and aromatic polyamide, and

inorganic materials such as ceramics, carbon-based membranes, and zirconia are also used to make NF and RO membranes. Dyeing wastewater treatment by NF is one of the rare applications that can handle highly concentrated and complex solutions. However, since it is very sensitive to contamination by macromolecules, the influent water needs pretreatment.

Reverse Osmosis (RO) [28-30]

Reverse Osmosis can remove most types of ionic compounds, reactive dyes, and chemical agents in a single step. The osmotic pressure becomes more important the higher the concentration of dissolved dye. Therefore, more energy is required for the separation process. The RO, like NF, is also very sensitive to contamination and the influent must be carefully pretreated. The RO membranes are usually made of cellulose acetate and aromatic polyamides, as well as inorganic materials.

1.3.1.3. Oxidation with sodium hypochlorite

Sodium hypochlorite discharges chlorine gas in aqueous solution, and dyes are decolorized and removed by the discharged chlorine gas. Increasing the chlorine concentration favors the dye removal and decolorization process and also reduces the pH. Dyes containing amino or substituted amino groups in the naphthalene ring are most susceptible to chlorine bleaching. This treatment is not effective for discoloration of disperse dyes, and the frequency of use is decreasing due to the negative effect of the emission of organic halogens during the treatment [28].

1.3.1.4. Oxidation by Ozonation

As is well known, ozone is a powerful oxidizing agent and can decompose synthetic dyes. Ozone molecules act as electron acceptors and can convert hydroxide ions into hydroxyl free radicals (·OH) that react with organic and inorganic pollutants. Therefore, at a pH with a high dissolution amount of hydroxyl ions (OH-), the formation of hydroxyl radicals (·OH) may be promoted, and the oxidation of organic dyes may become active. The input of H_2O_2 or UV can produce more ozone, and as a result, more OH radicals can be produced, which can improve the rate of decolorization. The advantage of ozonation is that it directly decomposes organic pollutants, so no other secondary pollution occurs. However, instability due to temperature and PH and high facility installation cost remain disadvantages. The oxidation process of many dyes and other organic pollutants (RH) by ozone is as follows [29,31-32]:

$$H_2O+O_3 \rightarrow HO_3^+ + OH^- \quad (1\text{-}1)$$

$$HO_3^+ + OH^- \rightarrow 2HO_2 \quad (1\text{-}2)$$

$$O_3 + HO_2 \rightarrow HO\cdot + 2O_2 \quad (1\text{-}3)$$

$$HO\cdot + HO_2 \rightarrow + H_2O + O_2 \quad (1\text{-}4)$$

$$RH + HO\cdot \rightarrow R\cdot + H_2O \quad (1\text{-}5)$$

1.3.1.5. Coagulation

The addition of chemicals or coagulants is required to speed up the agglomeration or particle growth of organic matter in wastewater. Coagulants include inorganic coagulants such as lime, ferrous sulfate, ferric sulfate, ferric chloride, aluminum sulfate, aluminum chloride, and organic coagulants such as polyelectrolytes. Organic coagulants are cationic, anionic, and nonionic, all three being used extensively in wastewater treatment. When a coagulant is added, ions of organic matter can be neutralized and stable colloids can be produced. Organic coagulants such as polyelectrolytes can provide adsorption and crosslinking between particles. As a result, particle clusters are formed and can be precipitated or filtered under gravity. However, using it alone for dye wastewater treatment is relatively inefficient. For example, only 50% can be removed by using alum or ferrous sulfate for an azo active yellow dye. However, the downside to this treatment is that the sludge is finally produced and there is an additional cost for the treatment of the sludge [33].

1.3.1.6. Electrocoagulation (EC)

EC generate metal ions in wastewater by using electric current and sacrificial anodes (such as Fe and Al). When metal ions with opposite charges are provided to wastewater, organic matter can be neutralized to form colloids. In other words, since the metal hydroxide released from the anode acts

as a coagulant, colloids are formed and easily rise to the surface by H_2 generated at the cathode. And it has been found that the external addition of coagulant improves the processing efficiency. However, since iron hydroxide sludge is generated on the electrode surface, its use is limited. In general, in EC treatment, the decolorize efficiency was found to be 90-95%, and COD removal was found to be 30-36% under optimal conditions. In addition, factors that affect electrochemical performance include current strength, number and spacing of electrodes used, pH, temperature, properties of electrolytes, surface tension and flow rates of wastewater, and properties of dyes. The mechanism of electrocoagulation is as follows [29, 34]:

Anode $$4Fe \leftrightarrow 4Fe^{2+} + 8e^{-}$$ (1-6)

Solution $$4Fe^{+} + 10H_2O + O_2 \leftrightarrow 4Fe(OH)_3 + 8H^{+}$$ (1-7)

Cathode $$8H^{+} + 8e^{-} \rightarrow 4H_2$$ (1-8)

1.3.1.7. Ionic exchange

Ion exchange has not been widely used in wastewater treatment containing dyes. This is because ion exchangers cannot accommodate a wide range of dyes. The colored wastewater is passed through the ion exchange resin until the available exchange sites are saturated. Using this method, cationic and anionic dyes can be successfully removed from wastewater. One major drawback is the high operating cost [28, 31].

1.3.2. Biological treatment method

1.3.2.1. Aerobic biological treatment

Currently, the most used biodegradation method involves aerobic microorganisms, which use molecular oxygen as a reducing equivalent receptor in the respiratory process. The microorganisms used depend on the dye, and fungi such as lignolytic fungi, Phanerochaete chrysosporium,

Geotrichum candidum, Trametes versicolor, Bjerkandera adusta, Penicillium sp., Pleurotus ostreatus, Pycnoporus cinnabarinus, and Pyricularia oryzae are used for aerobic decomposition. In addition, bacterial strains of Pseudomonas stutzeri, Acetobacter liquefaciens and Klebsiella pneumonia are also used. Wastewater treatment plants are not a natural habitat for microorganisms, so special care must be taken to establish these fungi in wastewater treatment systems.

In general, most azo dyes in conventional aerobic sewage treatment plants are not decomposed by bacteria. Therefore, conventional aerobic sewage treatment systems are not useful for decolorization of wastewater containing azo dyes. In addition, about 50 to 150 mg of each dye/l has the disadvantage of taking a little time because it takes 5 to 10 days to decolorize [11, 28, 35-36].

1.3.2.2. Anaerobic biological treatment

Azo dyes make up 60 ± 70% of all textile dyes, but in aerobic sewage treatment plants, most azo dyes are not easy to degrade. On the other hand, anaerobic biological purification can decolorize azo and other water-soluble dyes. Anaerobic microorganisms capable of decolorizing include Pseudomonas, Bacillus, and Clostridium, and the degree of decolorizing depends on the type of dye, substituent, and molecular weight. Decolorization is reported to involve oxidation-reduction reactions with hydrogen rather than oxygen, as in aerobic systems, and to produce methane, carbon dioxide, hydrogen sulfide, and other gaseous compounds. In anaerobic systems, azo dyes break azo bonds and decolorize, but toxic amines are formed. Anaerobic decomposition only results in azo reduction and no mineralization occurs. While many microbes can break the chromophores of some dyes, few microbes can mineralize dyes into CO_2 and H_2O. Obviously, this is due to the complex structure of the dye. The amines produced by reduction of azo dyes are colorless, but very resistant to further degradation under anaerobic conditions. Therefore, careful monitoring is required before the treated wastewater is discharged into the waterway. It also has the disadvantage of storing wastewater in large tanks because the biological treatment process requires a long time [8, 11, 28, 35].

1.4. Semiconductor photocatalyst

As shown in Table 1-3, the existing wastewater treatment technology has disadvantages such as cost, stability, slurry, pretreatment, and slow decomposition rate. [3, 8, 10].

Table 1-3 Disadvantages of the existing wastewater treatment.

Processes	Disadvantages
Absorption	Cost of activated carbon Difficult to recycle
Ultra-filtration	Insufficient quality of the treated wastewater Formation of sludge
Micro-filtration	Insufficient quality of the treated wastewater Formation of sludge
Nano-Filtration	Pretreatment required for removal of macromolecules
Reverse Osmosis	Pretreatment required for removal of macromolecules High pressure
Oxidation with sodium hypochlorite	Release of aromatic amines
Oxidation by Ozonation	Short half-life (20 min) High equipment cost
Coagulation	Formation of sludge Production of sludge blocking filter
Electrocoagulation	Formation of sludge
Ionic exchange	Not effective for all dyes High operating cost
Aerobic biological treatment	Low biodegradability of dyes Microorganisms used depend on the dye
Anaerobic biological treatment	Low biodegradability of dyes Microorganisms used depend on the dye

Therefore, the development of an eco-friendly, high-efficiency, low-cost organic pollutant treatment method has become an important task for researchers. Recently, photocatalytic oxidation of organic pollutants has been proposed as a promising alternative [4]. Because photocatalytic oxidation treatment can photodecompose organic pollutants into H_2O, CO_2, inorganic substances without generating secondary substances, no slurry is created. In addition, it does not require pretreatment and has excellent characteristics in terms of cost. The process of decomposing organic pollutants using inexpensive eco-friendly metal oxide photocatalysts such as WO_3 [37], Fe_2O_3 [38], ZnO [39-40], TiO_2 [41-42], and SnO_2 [43] has been extensively studied. In addition, because the photocatalytic reaction occurs on the surface of the photocatalyst, nano-sized particles with a large specific surface area are attracting attention [44-45].

As shown in Figure 1-1, it is well known that when ZnO is irradiated with photon energy equal to or greater than the bandgap energy, ZnO absorbs the photon energy so that electrons in the valence band (VB) are excited to the conduction band (CB):

$$ZnO + h\nu \rightarrow ZnO(e^-_{CB} + h^+) \qquad (1\text{-}9)$$

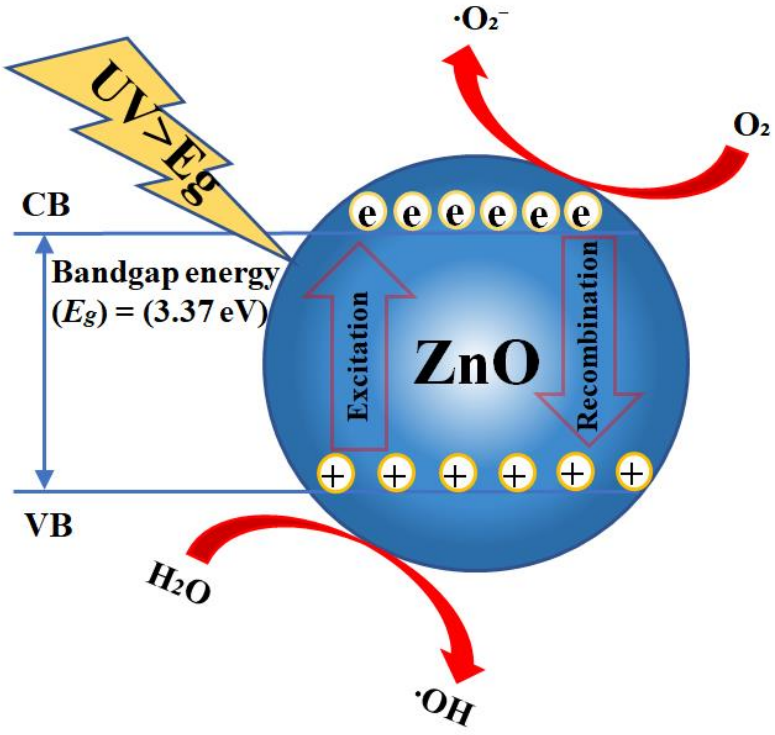

Figure 1-1 Photocatalytic reaction mechanism of ZnO particle.

When the separation of the holes of the VB and electrons of the CB is maintained, the holes and electrons can be moved to the surface of the catalyst and used for the oxidation/reduction reaction. Holes can form hydroxyl radicals (•OH) which react with H_2O or OH^- on the surface of the catalyst and contribute to photodecomposition (Eqs. 1-10 and 11). Free electrons can form superoxide radical anion ($O_2•^-$) which is an active species by oxygen. The superoxide radical anion ($O_2•^-$) reacts with H^+ to form hydrogen peroxide (H_2O_2), and the generated hydrogen peroxide (H_2O_2) is converted into hydroxyl radicals (•OH) by ultraviolet light (Eqs. 1-12,13,14 and 15). The resulting ·OH radical acts as a strong oxidizing agent and converts the organic material or polymer into carbon dioxide (CO_2), water (H_2O) and other less hazardous molecules than the original material (Eq. 1-16) [3, 46-47]: Many organic dyes have benzene rings with high chemical stability as shown in Table 1-1. Therefore, since RhB is often used as a model material for organic dyes, it was also adopted in this study.

$$OH^- + h^+ \rightarrow \cdot OH \quad (1\text{-}10)$$

$$H_2O + h^+ \rightarrow \cdot OH + H^+ \quad (1\text{-}11)$$

$$O_2 + e^- \rightarrow O \cdot_2^- \quad (1\text{-}12)$$

$$O \cdot_2^- + H^+ \rightarrow \cdot OOH \quad (1\text{-}13)$$

$$2 \cdot OOH \rightarrow O_2 + H_2O_2 \quad (1\text{-}14)$$

$$H_2O_2 + h\nu \rightarrow 2 \cdot OH \quad (1\text{-}15)$$

$$\text{Pollutant} + \cdot OH \rightarrow CO_2 + H_2O + \text{degradation product} \quad (1\text{-}16)$$

The main drawback of semiconductor photocatalysts is the reduced efficiency due to the rapid

recombination of excited electron-hole pairs. [3, 10]. For example, semiconductor photocatalysts such as ZnO and TiO_2 have limited photocatalytic activity due to the fast electron-hole recombination rate. To control the electron-hole recombination of a photocatalyst, doping of nanotubes [42], graphene [41], base metals [48], metal oxides [49], metal sulfides [50], polymers [51], and noble metals [52-53] has been studied. In particular, the combination of a noble metal with a semiconductor such as ZnO provides an improved photocatalytic activity by trapping excitation electrons. Figure 1-2 shows the reaction

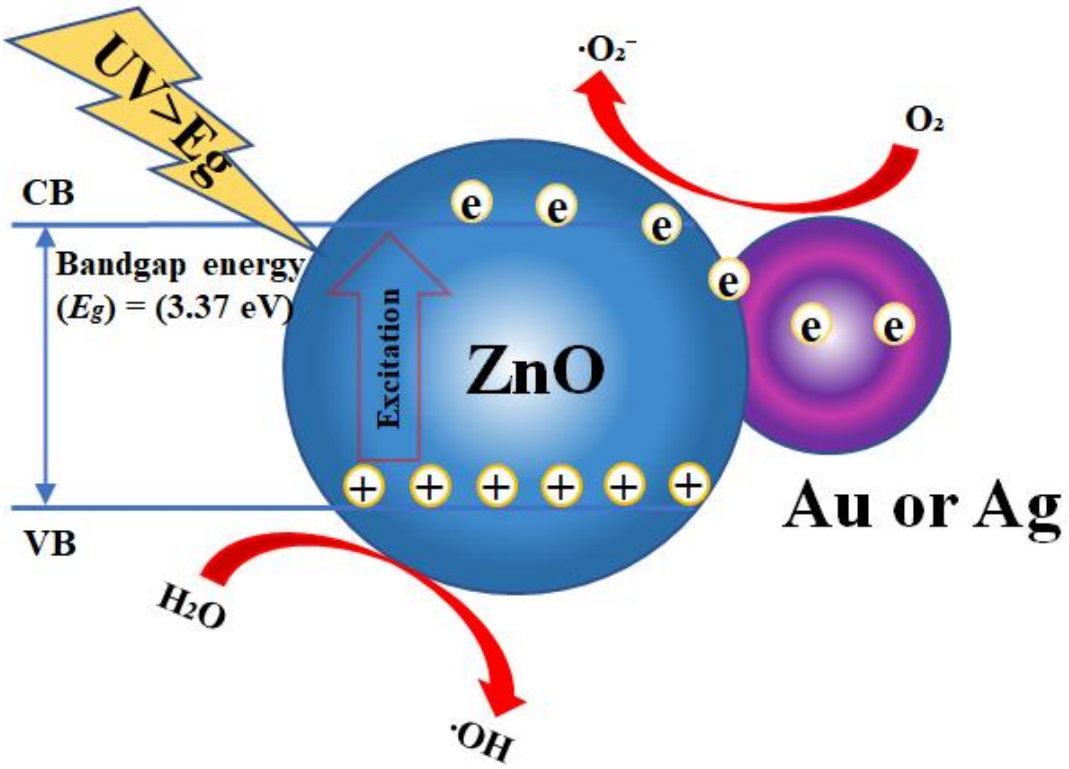

Figure 1-2 Photocatalytic reaction mechanism of Au/ZnO composite particles.

mechanism of a noble metal-supported photocatalyst. When a noble metal is supported on a photocatalyst, a noble metal acts as an electron sink and delays the recombination of the excited electrons and holes, so the efficiency of the photocatalyst can be improved [10]. Among a noble metal, research on supporting Au [54-55], Pt [54, 56], Pd [57], and Ag [3,58-63] is actively underway. Various methods have been developed to synthesize noble metal doped photocatalysts. These include chemical bath deposition [58], photochemical [59], sol-gel [60], solvothermal [61], precipitation-decomposition [62], hydrothermal [63], and flame spray pyrolysis [3].

Moreover, another disadvantage of photocatalytic treatment is that it is very difficult to recover nano-sized photocatalysts after removing organic pollutants from wastewater, and reuse is greatly

limited [8]. The inability to recycle photocatalytic particles not only increases the cost but can lead to new pollution [44]. Therefore, research is being conducted to generate particles with relatively large particle size and high activity or to support magnetic particles.

1.4.1. Zinc oxide (ZnO)

In the semiconductor metal oxide series, II-VI group semiconductors are recognized as applications in solar cells, solar cells, field effect transistors, optoelectronic devices, and photoluminescence appliances [64-66]. Among these semiconductors, ZnO is a direct bandgap semiconductor (3.4eV) with a huge exciton binding energy of 60meV, and has been regarded as a semiconductor having numerous applications in the scientific community since the 1930s [67]. Therefore, in recent years, it is a versatile material that has been used in various applications due to its excellent biocompatibility and low toxicity. Examples include solar cells [68], gas detectors [69], photocatalysts, optoelectronic [70], etc. In addition to this, ZnO is used as an additive in industrial products such as pigments, adhesives, cement, lubricants, glass, paint, rubber, cosmetics, and coatings [71]. Research on composite materials is also reported, and transition metal/rare earth (RE) doped ZnO structure shows superior structural and optical properties such as photoluminescence, transmittance, diffraction, and magnetic behavior than pure ZnO.

In this study, we adopted the spray pyrolysis method to generate submicron particles and support other metals. Along with ZnO, TiO_2 is also widely used as a photocatalyst, but since a water-soluble raw material is used in the spray pyrolysis method, zinc oxide was produced using zinc nitrate, which can be used as a source at a relatively low cost.

1.5. Summary of this thesis

In this paper, two experiments were presented to confirm the photolysis of organic pollutants using a photocatalyst and the reusability of the photocatalyst. First, photocatalytic nanoparticles have a large specific surface area, so they have good photodegradation properties, but have a disadvantage in that they are expensive because they cannot be recovered and recycled. Therefore, relatively large sub-micro-sized particles were simply one-pot synthesized using the spray pyrolysis method, and single-crystal metal particles were doped inside the photocatalyst to enhance the photocatalytic activity. And the possibility of recovery and recycling through gravity sedimentation was confirmed. Second, in

order to simplify the recovery of the photocatalyst particles, a magnetic recovery experiment through magnetite doping was conducted. Micro-sized ZnO/Fe_3O_4 particles were generated using the co-precipitation method, and Ag doping was performed for higher photocatalytic properties. And the possibility of recovery and reuse of particles using magnetism was confirmed.

In Chapter 2, the electron-hole recombination control of the photocatalyst was investigated by loading Au in ZnO (Au/ZnO). Using the Ultrasonic Spray Pyrolysis (USP) method, Au/ZnO particle generation is easily achieved under various conditions. XRD analysis confirms the crystal peaks of ZnO and Au. The EDX mapping and STEM images of the particles show that the Au crystals are well dispersed in the inner and outer portions of ZnO. The photocatalytic decomposition rate of organic dye (Rhodamine-B) is faster than that of ZnO in all Au/ZnO particles, and the best photocatalytic activity occurs in particles with 0.1 mass% Au supported on ZnO particles. In addition, optimal photolysis activity occurs in 100 ml of 5 mg/L RhB aqueous solution and 10 mg dose of Au/ZnO particles.

In Chapter 3, the inhibition of electron-hole recombination was investigated by supporting Ag nanoparticles on a ZnO photocatalyst. Ag/ZnO particles were generated under various conditions using the Ultrasonic Spray Pyrolysis method. Through XRD analysis, the crystal peaks of Ag and ZnO were confirmed in the generated particles. EDX mapping and STEM images show that Ag nanoparticles are well dispersed in ZnO. The photolysis rate of organic dye (Rhodamine-B) was faster than that of ZnO in all Ag/ZnO particles, and particles with 0.2 mass% silver nitrate supported on ZnO particles showed 2 times better photolysis activity than P25. In addition, the optimal photolysis activity was confirmed in 100ml of 5mg/L RhB aqueous solution and 10mg of Ag/ZnO particles, and reusability was also confirmed.

In Chapter 4, synthesis of ZnO/Fe_3O_4 composite particles was attempted using the USP and co-precipitation method under various conditions. When the USP method was used as a single method, the crystal peaks of the target products ZnO and Fe_3O_4 were not observed, and a single crystal peak of $ZnFe_2O_4$ was confirmed under certain conditions. When particles were generated using the USP and co-precipitation method together, the crystal peaks of the target products, ZnO and Fe_3O_4 were observed, and the magnetism of the generated particles was confirmed. However, since the aggregation of particles and uncoated ZnO particles were confirmed, it was confirmed that the surface modification using sodium citrate was not suitable for the generation of ZnO/Fe_3O_4 composite

particles. When co-precipitation was used as a single method, crystal peaks of the target products ZnO, Ag, and Fe_3O_4 were observed, and the magnetism of the generated particles was also observed. In addition, the Ag particles dispersed in the particles could be confirmed with backscattered electron images. In the photolysis experiment, excellent photolysis properties were confirmed in ZnO/Fe_3O_4 composite particles generated by adding 0.2 mass% of silver nitrate.

Final conclusions are presented in Chapter 5.

1.6. References

1. R. Kant, Textile dyeing industry an environmental hazard, Natural Science, 4 (2012) 22-26.
2. V. Vaiano, M. Matarangolo, O. Sacco, D. Sannino, Photocatalytic treatment of aqueous solutions at high dye concentration using praseodymium-doped ZnO catalysts, Applied Catalysis B: Environmental, 209 (2017) 621–630.
3. M.J. Height, S.E. Pratsinis, O. Mekasuwandumrong, P. Praserthdam, Ag-ZnO catalysts for UV-photodegradation of methylene blue, Applied Catalysis B: Environmental, 63 (2006) 305–312.
4. O.J. Hao, H. Kim, P.C. Chiag, Decolourisation of wastewater, Critical Reviews in Environmental Science and Technology, 30 (2000) 449-505.
5. A. Nezamzadeh-Ejhieh, M. Amiri, CuO supported clinoptilolite towards solar photocatalytic degradation of p-aminophenol, Powder Technol, 235 (2013) 279-288.
6. S. Phukan, D. Kakati, Md. Harunar Rashid, Use of invasive weed to synthesize shape-tunable gold nanoparticles and evaluation of their catalytic activities in dye reduction, Current Nanoscience, 14 (2018) 511-519.
7. H. Zollinger, Synthesis, properties and applications of organic dyes and pigments, in Color Chemistry, VCH, New York, NY, USA, 1987.
8. F. Han, V.S.R. Kambala, M. Srinivasan, D. Rajarthnam, R. Naidu, Tailored titanium dioxide photocatalysts for the degradation of organic dyes in wastewater treatment: A review, Applied Catalysis A: General, 359 (2009) 25–40.
9. A. Bhattacharya, A. Gupta, A. Kaur, D. Malik, Efficacy of Acinetobacter sp. B9 for simultaneous removal of phenol and hexavalent chromium from co-contaminated system,

Appl Microbiol Biotechnol, 98 (2014) 9829–9841.

10. T. Welderfael, O.P. Yadav, A.M. Taddesse, J. Kaushal, Synthesis, characterization and photocatalytic activities of Ag–N-codoped ZnO nanoparticles for degradation of methyl red, The Bulletin of the Chemical Society of Ethiopia, 27 (2013) 221–232.

11. W. Sun, L. Chen, J. Tian, J. Wang, S. He, Degradation of a monoazo dye Alizarin Yellow GG in aqueous solutions by gamma irradiation: Decolorization and biodegradability enhancement, Radiation Physics and Chemistry, 83 (2013) 86-89.

12. A. Razavi, H. Rezaei, A. Shahbazi, Removal of Congo red from aqueous solutions using nano-chitosan, Environmental Resources Research, 5 (2017) 25-34.

13. A. Mittal, V. Gajbe, J. Mittal, Removal and recovery of hazardous triphenylmethane dye, Methyl Violet through adsorption over granulated waste materials, Journal of Hazardous Materials, 150 (2008) 364-375.

14. G.K. Parshetti, S.G. Parhetti, A.A. Telke, D.C. Kalyani, R.A. Doong, S.P. Govindwar, Biodegradation of Crystal Violet by Agrobacterium radiobacter, Journal of Environmental Sciences, 23 (2011) 1384-1393.

15. A. Nezamzadeh-Ejhieh, Z. Salimi, Heterogeneous photodegradation catalysis of o-phenylenediamine using CuO/X zeolite, Applied Catalysis A: General, 390 (2010) 110-118.

16. N. Li, Y. Gu, M. Gao, Z. Wang, D. Xiao, Y. Li, R. Lin, H. He, Colorimetric determination of o-phenylenediamine in water samples based on the formation of silver nanoparticles as a colorimetric probe, Spectrochimica Acta Part A: Molecular and Biomolecular Spectroscopy, 140 (2015) 328-333.

17. T. Rasheed, M. Bilal, H.M.N. Iqbal, H. Hu, X. Zhang, Reaction Mechanism and Degradation Pathway of Rhodamine 6G by Photocatalytic Treatment, Water Air Soil Pollut, 228 (2017) 1-10.

18. S. Rajorya, S. Bargole, V.K. Saharan, Degradation of a cationic dye (Rhodamine 6G) using hydrodynamic cavitation coupled with other oxidative agents: Reaction mechanism and pathway, Ultrasonics Sonochemistry, 34 (2017) 183-194.

19. K. Shen, M.A. Gondal, Removal of hazardous Rhodamine dye from water by adsorption onto exhausted coffee ground, Journal of Saudi Chemical Society, 21 (2017) 120-127.

20. D. Glossman-Mitnik, Computational Study of the Chemical Reactivity Properties of the

Rhodamine B Molecule, Procedia Computer Science, 18 (2013) 816–825.

21. R. Jain, M. Mathur, S. Sikarwar, A. Mittal, Removal of the hazardous dye rhodamine B through photocatalytic and adsorption treatments, Journal of Environmental Management, 85 (2007) 956–964.

22. A. Mittal, D. Kaur, A. Malviya, J. Mittal, V.K. Gupta, Adsorption studies on the removal of coloring agent phenol red from wastewater using waste materials as adsorbents, Journal of Colloid and Interface Science, 337 (2009) 345-354.

23. N.A. Abdullah, R. Othaman, I. Abdullah, N. Jon, A. Baharum, Studies on the Adsorption of Phenol Red Dye Using Silica-filled ENR/PVC Beads, Journal of Emerging Trends in Engineering and Applied Sciences (JETEAS), 3 (2012) 845-850.

24. A.K. Kushwaha, N. Gupta, M.C. Chattopadhyaya, Removal of cationic methylene blue and malachite green dyes from aqueous solution by waste materials of Daucus carota, Journal of Saudi Chemical Society, 18 (2014) 200-207.

25. M.S. Rai, P. Rama Bhat, P.S. Prajna, K. Jayadev, P.S.V. Venkatakrishna Rao, Degradation of malachite green and congo red using Aloe barabadensis Mill. Extract, International Journal of Current Microbiology Applied Sciences, 3 (2014) 330-340.

26. C.-H. Chen, C.-F. Chang, S.-M. Liu, Partial degradation mechanisms of malachite green and methyl violet B byShewanella decolorationisNTOU1 under anaerobic conditions, Journal of Hazardous Materials, 177 (2010) 281-289.

27. Sh. Jafari, S. Azizian, B. Jaleh, Adsorption kinetics of methyl violet onto TiO_2 nanoparticles with different phases, Colloids and Surfaces A: Physicochemical and Engineering Aspects, 384 (2011) 618-623.

28. Y. Anjaneyulu, N. Sreedhara Chary, D. Samuel Suman Raj, Decolourization of industrial effluents – available methods and emerging technologies – a review, Reviews in Environmental Science and Bio/Technology, 4 (2005) 245–273.

29. B. Ramesh Babu, A.K. Parande, S. Raghu, T. Prem Kumar, Cotton Textile Processing: Waste Generation and Effluent Treatment, The Journal of Cotton Science, 11 (2007) 141-153.

30. Z. Carmen, S. Daniela, Textile Organic Dyes – Characteristics, Polluting Effects and Separation/Elimination Procedures from Industrial Effluents – A Critical Overview,

Organic Pollutants Ten Years After the Stockholm Convention–Environmental and Analytical Update, 2012, pp.65-86.

31. Y.M. Slokar, A. Majcen Le Marechal, Methods of Decoloration of Textile Wastewaters, Dyes and Pigments, 37 (1998) 335-356.

32. G. Sudarjanto, B. Keller-Lehmann, J. Keller, Photooxidation of a reactive azo-dye from the textile industry using UV/H2O2 technology: process optimization and kinetics, Journal of Water and Environment Technology, 3 (2005) 1-7.

33. C. Zaharia, R. Diaconescu, M, Surpăţeanu, Study of flocculation with PONILIT GT-2 anionic polyelectrolyte applied into a chemical wastewater treatment, Central European Journal of Chemistry, 5 (2007) 239-256.

34. N. Daneshvar, H. Ashassi-Sorkhabi, A. Tizpar, Decolorization of orange II by electrocoagulation method, Separation and Purification Technology, 31 (2003) 153-162.

35. A. Stolz, Basic and applied aspects in the microbial degradation of azo dyes, Appl Microbiol Biotechnol, 56 (2001) 69-80.

36. T. Robinson, G. McMullan, R. Marchant, P. Nigam, Remediation of dyes in textile effluent: a critical review on current treatment technologies with a proposed alternative, Bioresource Technology, 77 (2001) 247-255.

37. D. Chen, J. Ye, Hierarchical WO_3 Hollow Shells: Dendrite, Sphere, Dumbbell, and Their Photocatalytic Properties, Advanced Functional Materials, 18 (2008) 1922–1928.

38. S.W. Cao, Y.J. Zhu, Hierarchically Nanostructured α-Fe_2O_3 Hollow Spheres: Preparation, Growth Mechanism, Photocatalytic Property, and Application in Water Treatment, The Journal of Physical Chemistry C, 112 (2008) 6253–6257.

39. K. Intarasuwan, P. Amornpitoksuk, S. Suwanboon, Effect of the mixing rate on the morphology and photocatalytic activity of ZnO powders prepared by a precipitation method, Advanced Powder Technology, 24 (2013) 999-1005.

40. J. Xie, Y. Li, W. Zhao, L. Bian, Y. Wei, Simple fabrication and photocatalytic activity of ZnO particles with different morphologies, Powder Technology, 207 (2011) 140-144.

41. Q. Zhou, Y.H. Zhong, X. Chen, J.H. Liu, X.J. Huang, Y.C. Wu, Adsorption and photocatalysis removal of fulvic acid by TiO_2–graphene composites, Journal of Materials Science, 49 (2014) 1066–1075.

42. H. Wang, H.L. Wang, W.F Jiang, Z.Q. Li, Photocatalytic degradation of 2,4-dinitrophenol (DNP) by multi-walled carbon nanotubes (MWCNTs)/TiO_2 composite in aqueous solution under solar irradiation, Water Research, 43 (2009) 204-210.

43. S.P. Kim, M.Y. Choi, H.C. Choi, Photocatalytic activity of SnO_2 nanoparticles in methylene blue degradation, Materials Research Bulletin, 74 (2016) 85-89.

44. X.F. Bian, K.Q. Hong, X. Ge, R. Song, L.Q. Liu, M.X. Xu, Functional Hierarchical Nanocomposites Based on ZnO Nanowire and Magnetic Nanoparticle as Highly Active Recyclable Photocatalysts, The Journal of Physical Chemistry C, 119 (2015) 1700–1705.

45. X. Zhang, S. Xu, G.R Han, Fabrication and photocatalytic activity of TiO_2 nanofiber membrane, Materials Letters, 63 (2009) 1761-1763.

46. D. Nipane, S.R. Thakare, N.T. Khati, Synthesis of Novel ZnO Having Cauliflower Morphology for Photocatalytic Degradation Study, Journal of Catalysts, 77 (2013) 1-8.

47. D. Naresh Yadav, K. Anand Kishore, B. Bethi, S.H. Sonawane, ZnO nanophotocatalysts coupled with ceramic membrane method for treatment of Rhodamine-B dye wastewater, Environment Development and Sustainability, 20 (2018) 2065-2078.

48. R. Asahi, T. Morikawa, T. Ohwaki, K. Aoki, Y. Taga, Visible-light photocatalysis in nitrogen-doped titanium oxides, Science, 293 (2001) 269-271

49. P. Sathishkumar, R. Sweena, J.J. Wu, S. Anandan, Synthesis of CuO-ZnO nanophotocatalyst for visible light assisted degradation of a textile dye in aqueous solution, Chemical Engineering Journal, 171 (2011) 136-140.

50. A. Franco, M.C. Neves, R. M.M.L. Ribeiro Carrott, M.H. Mendonça, M.I Pereira, O.C. Monteiro, Photocatalytic decolorization of methylene blue in the presence of TiO_2/ZnS nanocomposites, Journal of Hazardous Materials, 161 (2009) 545-550.

51. S. Ameen, M. Shaheer Akhtar, Y.S. Kim, O.B. Yang, H.S. Shin, An effective nanocomposite of polyaniline and ZnO: preparation, characterizations, and its photocatalytic activity, Colloid and Polymer Science, 289 (2011) 415-421.

52. V. Vaiano, M. Matarangolo, J.J. Murcia, H. Rojas, J.A. Navío, M.C. Hidalgo, Enhanced photocatalytic removal of phenol from aqueous solutions using ZnO modified with Ag, Applied Catalysis B: Environmental, 225 (2018) 197-206.

53. Y.H. Lu, M. Xu, L.X. Xu, C.L. Zhang, Q.P. Zhang, X.N. Xu, S. Xu, K. Ostrikov, Enhanced

ultraviolet photocatalytic activity of Ag/ZnO nanoparticles synthesized by modified polymer-network gel method, Journal of Nanoparticle Research, 17 (2015) 1-15.

54. P. Pawinrat, O. Mekasuwandumrong, J. Panpranot, Synthesis of Au–ZnO and Pt–ZnO nanocomposites by one-step flame spray pyrolysis and its application for photocatalytic degradation of dyes, Catalysis Communications, 10 (2009) 1380–1385.

55. L. Chen, L. Luo, Z. Chen, M. Zhang, J.A. Zapien, C.S. Lee, S.T. Lee, ZnO/Au composite nanoarrays as substrates for surface-enhanced Raman scattering detection, The Journal of Physical Chemistry C, 114 (2010) 93–100.

56. H. Zeng, P. Liu, W. Cai, S. Yang, X. Xu, Controllable Pt/ZnO porous nanocages with improved photocatalytic activity, The Journal of Physical Chemistry C, 112 (2008) 19620–19624.

57. Y. Chang, J. Xu, Y. Zhang, S. Ma, L. Xin, L. Zhu, C. Xu, Optical Properties and Photocatalytic Performances of Pd Modified ZnO Samples, The Journal of Physical Chemistry C, 113 (2009) 18761–18767.

58. Y.F. Wang, J.H. Yao, G. Jia, H. Lei, Optical Prosperities of Ag–ZnO Composition Nanofilm Synthesized by Chemical Bath Deposition, Acta Physica Polonica A, 119 (2011) 451–454.

59. W. Xie, Y.Z. Li, W. Sun, J. Huang, H. Xie, X. Zhao, Surface modification of ZnO with Ag improves its photocatalytic efficiency and photostability. Journal of Photochemistry and Photobiology A: Chemistry, 216 (2010), 149–155.

60. Y. Lu, Y. Lin, D. Wang, L. Wang, T. Xie, T. Jiang, Surface charge transfer properties of high-performance Ag-decorated ZnO photocatalysts, Journal of Physics D: Applied Physics, 44 (2011) 1-7.

61. Y.H. Zheng, L.R. Zheng, Y.Y. Zhan, X.Y. Lin, Q. Zheng, K. Wei, Ag/ZnO heterostructure nanocrystals: synthesis, characterization, and photocatalysis, Inorganic Chemistry, 46 (2007), 6980–6986.

62. B. Subash, B. Krishnakumar, M. Swaminathan, M. Shanthi, Synthesis and characterization of cerium–silver co-doped zinc oxide as a novel sunlight-driven photocatalyst for effective degradation of Reactive Red 120 dye. Materials Science in Semiconductor Processing, 16 (2013), 1070–1078.

63. W. Lu, S. Gao, J. Wang, One-Pot Synthesis of Ag/ZnO Self-Assembled 3D Hollow

Microspheres with Enhanced Photocatalytic Performance, The Journal of Physical Chemistry C, 112 (2008) 16792–16800.

64. M. Grätzel, Photoelectrochemical cells, Materials for Sustainable Energy, 444 (2001) 338-344.

65. R. Janisch, P. Gopal, N.A. Spaldin, Transition metal-doped TiO_2 and ZnO—present status of the field, Journal of physics: condensed matter, 17 (2005) 657-689.

66. K. Nomura, H. Ohta, K. Ueda, T. Kamiya, M. Hirano, H. Hosono, Thin-Film Transistor Fabricated in Single-Crystalline Transparent Oxide Semiconductor, Science, 300 (2003) 1269-1271.

67. Ü. Özgür, Ya.I. Alivov, C. Liu, A. Teke, M.A. Reshchikov, S. Doğan, V. Avrutin, S.J. Cho, H. Morkoç, A comprehensive review of ZnO materials and devices, Journal of Applied Physics, 98 (2005).

68. D.T. Wang, X.H. Zhu, Y.Z. Fang, J.H. Sun, C. Zhang, X.X. Zhang, Simultaneously composition and interface control for ZnO-based dye-sensitized solar cells with highly enhanced efficiency, Nano-Structures & Nano-Objects, 10 (2017) 1-8.

69. A.A. Tomchenko, G.P. Harmer, B.T. Marquis, J.W. Allen, Semiconducting metal oxide sensor array for the selective detection of combustion gases, Sensors and Actuators B, 93 (2003) 126-134.

70. S. Singh, M. Joshi, P. Panthari, B. Malhotra, A.C. Kharkwal, Citrulline rich structurally stable zinc oxide nanostructures for superior photo catalytic and optoelectronic applications: A green synthesis approach, Nano-Structures & Nano-Objects, 11 (2017) 1-6.

71. N. Serpone, D. Dondi, A. Albini, Inorganic and organic UV filters: Their role and efficacy in sunscreens and suncare products, Inorganica Chimica Acta, 360 (2007) 794-802.

Chapter 2 Evaluation of Photocatalysis of Au Supported ZnO Prepared by the Spray Pyrolysis Method

2.1. Introduction

Environmental pollution by residual dyes in the paper, textiles, and other industries is a very serious problem in developing countries as described in Chapter 1. Typically, wastewater is treated using adsorption or chemical coagulation methods. However, these methods only transfer dyes from water to solids, and require further treatment to decompose. Therefore, a better wastewater treatment method is necessary. Photocatalytic oxidation treatment of organic pollutants has recently been proposed as a promising alternative [1–3].

Photocatalytic applications of ZnO and TiO_2 have grown significantly due to their chemical and physical stabilities and low cost. ZnO is a semiconductor material with a wide bandgap energy (3.37 eV) and a large exciton binding energy of 60 meV [4]. Although TiO_2 is a more common photocatalyst than ZnO [5], ZnO can be used as a substitute for TiO_2 because they have similar bandgap energies. In addition, ZnO has a higher reported quantum efficiency than TiO_2 and has attracted attention for the photolysis of pollutants due to its high stability and wide bandgap energy [6-7]. This wide bandgap and large exciton binding energy are not only useful for the photolysis of organic pollutants but can also disinfect and eliminate odors. In addition, ZnO has several potential applications such as gas sensors, solar cells, varistors, and optoelectronic devices [8].

However, as previously explained, semiconductor photocatalysts such as ZnO and TiO_2 have limited photocatalytic activity due to the high electron-hole recombination rate [4, 7]. Therefore, in order to prevent the recombination of the excited electron-hole pairs and improve the photocatalytic properties, a composite material that supports nanotubes [9], graphene [10], base metals [11], metal oxides [12], metal sulfides [13], polymers [14] and noble metals [15-16] on the photocatalyst is being studied. In particular, since there are many applications depending on the type of supported noble metal and the method of synthesizing the particles, various types of supporting studies have been reported. Therefore, various methods are being developed to synthesize photocatalysts supporting noble metals.

Methods of generating particles include combustion, flame spray pyrolysis, sonochemical reaction, and hydrothermal, and the results of generating particles by each method have been reported. Pathak

et al. produced Au/ZnO and Ag/ZnO nanoparticles using the combustion method and evaluated the photocatalytic efficiency using methylene blue dye [17]. Pawinrat *et al*. produced Au/ZnO and Pt/ZnO nanoparticles using flame spray pyrolysis and evaluated the photocatalytic efficiency using methylene blue [18]. Kim *et al*. carried out Au nanoparticles on ZnO nanorods using the hydrothermal method and sonochemical method, and evaluated the photocatalytic efficiency using rhodamine B [19]. These nanoparticles show good photocatalytic efficiency because of their large specific surface area, but have the disadvantage of being difficult to recover after use. In addition, the wet method requiring post-treatment may reduce the photocatalytic efficiency due to agglomeration between particles. Haugen *et al*. confirmed that the size of the doped Au or Ag crystals increased and the photocatalytic activity decreased after calcination of the particles [20]. Therefore, there was a need for a method that could produce submicron-level particles without agglomeration in a single process. In addition, there was a need for a generation method that could increase the efficiency of the photocatalyst by supporting the noble metal as a single crystal.

Recently, Ebins *et al*. confirmed the crystallite size and catalyst characteristics after generating zinc oxide by temperature changes using ultrasonic spray pyrolysis (USP) [21]. The USP method can generate continuous particles in a single process, and it is possible to adjust the particle shape by temperature control. In addition, it was possible to control the crystallite size by the change in the concentration of the raw material solution, and it was possible to dope other substances by adding the target precursor to the aqueous solution of the raw material [22-23]. The USP method consists of four main steps: droplet generation by ultrasonic nebulizer, precipitation by evaporation of solution, chemical reaction of precursor at high temperature, and densification of initial particles [24-25].

In this study, we employ the USP method to generate functional particles with high oxidation characteristics that can be used in the oxidation treatment of organic pollutants. First, we experimentally examine the conditions in which ZnO particles are generated. Then, we prepare Au-doped ZnO (Au/ZnO) particles using chloroauric acid as the noble metal source. Finally, we analyze the structural, morphological, and photolysis characteristics of the obtained particles.

2.2. Experimental equipment and theory

2.2.1. Ultrasonic Spray Pyrolysis

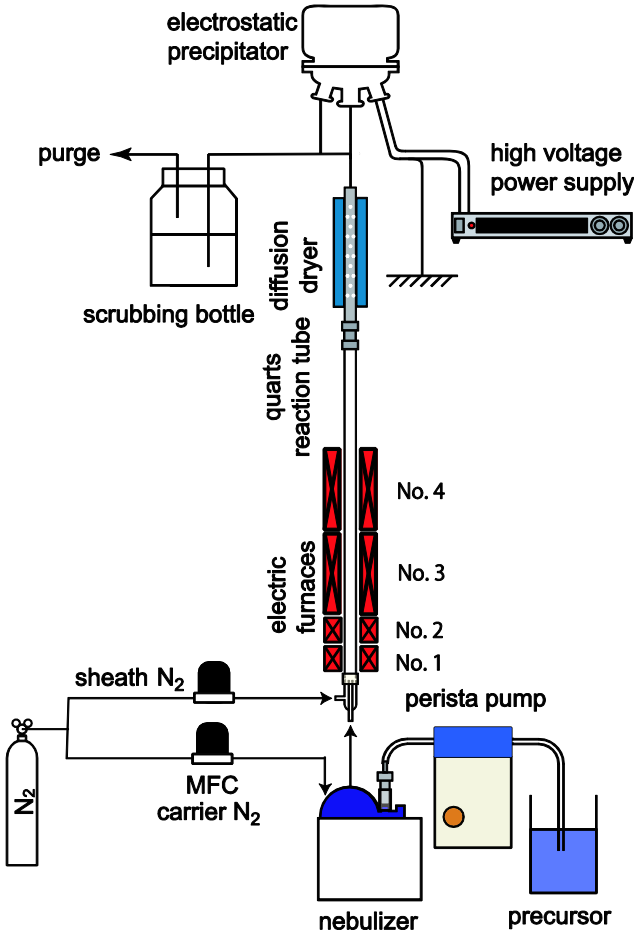

Figure 2-1 Schematic diagram of ultrasonic spray pyrolysis.

Application research on particles with a size of several μm or less is being conducted in electronic materials, catalysts, and analytical chemistry. Particles change their properties by their shape, size, and composition, so a controllable particle generation process is important. In addition, from the point of view of industrial application, the equipment must be simple and continuous operation, high production speed and low cost. Aerosol process, a method for producing particulate materials that combines both liquid and gas phase aerosol processes, may be such a process. Aerosol is a type of colloid in which solid or liquid particles are suspended in the atmosphere. The term "aerosol" is used in the fields of air, health and air pollutants and materials processing.

There are two main routes for particle production by the aerosol process. It is a method of converting from gas to particles and a method of converting from liquid to particles. In gas-particle conversion, particles are synthesized by cooling supersaturated vapors using a method called physical vapor deposition (PVD) or chemical vapor deposition (CVD) [25]. In the PVD method, evaporation of a solid or liquid is a source of vapor, and solid particles are formed via nucleation and condensation of saturated vapor in the cooling step. Many types of reactors, such as flame, furnace, plasma or laser, have been used to generate the vapor of the precursor. In the CVD method, vapors evaporated from a precursor are reacted with other precursor vapors or surrounding gases or pyrolyzed. Target particles are produced by chemical reaction or pyrolysis in the air and undergo condensation and agglomeration.

The main advantages of the gas-particle conversion method are the narrow size distribution, small particle size and high purity of the synthesized particles. However, it is difficult to prepare particulate materials due to the disadvantage that large agglomerates are formed during agglomeration and condensation in the gas phase. Differences in chemical reaction rates, vapor pressures, nucleation and growth rates during particle generation can lead to non-uniform particle synthesis results.

Liquid-to-particle conversion is typically a spray pyrolysis method. Because a solution or sol is used, the spray method is often classified as a liquid method. This method can be used to synthesize functional particles such as multi-component materials. Compared to the gas-to-particle conversion path, the spray method is a simple and inexpensive process, but little is known about the process itself [22].

Evonik's TiO_2 benchmark P25 is a good example of a photocatalyst produced on an industrial scale by vapor-fed aerosol flame synthesis (VAFS). This flame-assisted process involves burning in a flame by supplying a volatile precursor such as titanium tetrachloride ($TiCl_4$) in the gaseous phase. However, finding suitable volatile metal precursors can be limiting. Alternatively, techniques such as ultrasonic spray pyrolysis (USP) can solve this problem. USP can use a water-soluble precursor to generate aerosols using an ultrasonic atomizer and transport aerosol particles into the reactor using a carrier gas. In the USP method, a tube furnace may be used for the combustion or pyrolysis of the precursor [26].

The spray pyrolysis method is used not only in the synthesis of particles, but also in experiments such as thin film deposition and in industrial sites. In general, in the spray pyrolysis method, the

aerosol generated by the spray device is transported to the reactor by the carrier gas, and particles are generated through pyrolysis. Fig. 2-1 shows an experimental apparatus used in this research. The USP apparatus was composed of a nebulizer, a quartz glass reaction tube, electric furnaces, a diffusion dryer, and an electrostatic precipitator. In the USP device, the precursor solution is placed inside the ultrasonic nebulizer, which is a device containing a high-frequency ultrasonic vibrator. The carrier gas is introduced into the ultrasonic nebulizer and the aerosol is transported to the tubular reactor by the gas flow. Particles generated by pyrolysis in the tubular reactor move to the collector (filter, electrostatic precipitator, etc.).

The spray pyrolysis method has the following advantages. (i) The resulting particles are spherical. (ii) The diameter distribution is uniform and controllable from micrometer to submicron. (iii) The product is of high purity. (iv) The process is continuous. Since each sprayed droplet has the same composition, properties can be controlled through chemical control of the precursor solution. It is very promising to apply the spray pyrolysis process to industry because the speed of particle generation is fast and particles can be generated within seconds. Conversely, using conventional solid or liquid phase methods requires post-treatments such as calcination and milling to obtain the desired particle size, which often introduces impurities into the particles.

Figure 2-2 shows the particle formation process in the spray pyrolysis method. When the raw material droplets are heated, the solvent evaporates from the droplet surface, and the solute concentration on the droplet surface increases. Therefore, the solute diffuses toward the center of the droplet where the solute concentration is low, but when heating is performed rapidly, the solvent evaporates rapidly and the solute concentration on the droplet surface rapidly increases, eventually becoming supersaturated and precipitation of salt occurs. Then, the solvent inside the shell evaporates, and hollow particles and ruptured particles are generated. On the contrary, when gentle heating is performed, the evaporation rate of the solvent slows down and the solute diffuses toward the center of the droplet, so that the surface of the droplet does not become supersaturated, and the droplet solvent evaporates only from the surface of the droplet. And solid particles are formed [27]. As precursor solutions, inexpensive materials such as nitrates, chlorides and acetates are commonly used. In general, water or alcohol is used as the solvent.

The properties of the precursor, the carrier gas flow rate and temperature of furnaces are the main parameters that affect the morphology of the particles produced by spray pyrolysis. Hollow or ruptured particles often produced by spray pyrolysis are undesirable for applications. Depending on the production conditions, single crystal or polycrystalline particles are also formed. The average size and size distribution of the final particles can be roughly determined from the droplet size and the initial concentration of the starting solution. Therefore, the size or shape of the final particles produced is determined by the concentration and movement speed of the droplets produced by the nebulizer. Therefore, various spraying methods have been used in spray pyrolysis studies.

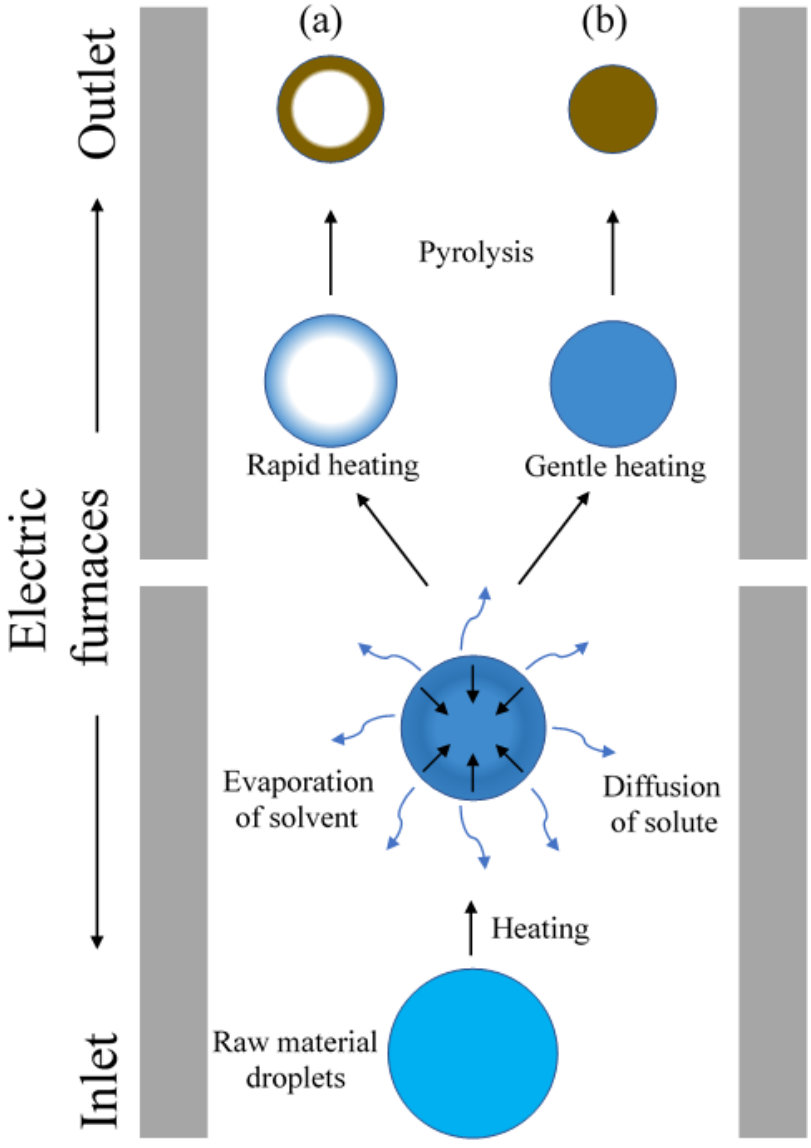

Figure 2-2 Particle formation process in USP method.

2.2.1.1. Atomization

Atomization is a key parameter to determine particle size. In the early stages of particle generation, precursors are supplied to specific atomization equipment to convert them into droplets. Certain skills are required to perform this droplet formation operation. In traditional methods, aerosol generation through temperature assisted evaporation treatment is commonly used. The principle of this method is to vaporize the precursor at a specific temperature to create droplets [28]. This method can produce single and uniform droplets, but cost becomes an issue. To solve this drawback, the use of certain momentum can be used as an alternative technique to traditional methods. Several types of driving force can be used to support the atomization process. For example, pressure, centrifugation, electrostatic and ultrasonic energy are selected depending on the required droplet size [29]. In addition to selecting the sprayer configuration, surface tension, viscosity, density, etc., should be considered in order to control the droplet size and properties of the spray precursor [30].

Table 2-1 Typical droplet sizes of depending on spray method.

Atomizer Type	Average Initial Droplet Size [μm]
Ultrasonic (submerged)	1 to 10 [33]
Ultrasonic (nozzle)	10 to 1000 [33]
Electrospray	15 to 25 [34]
Rotary	10 to 1000 [33]
Pressure	110 to 200 [34] 120 to 250 [35]
Air-blast orchard sprayer	130 to 200 [34]
Two-fluid	5 to 100 [35]
Cold–fogger	8 to 22 [34]
Grooved spinning disc	70 to 150 [34]
Smooth spinning disc	90 to 150 [34]
Knapsack mistblower	100 to 200 [34]

Among the many atomization methods (Table 2-1), ultrasonic atomization devices are widely used because of the high energy efficiency of aerosol generation, ease of use, and fast aerosol generation speed. Therefore, the USP method has been found to be effective in synthesizing various types of

materials and has the advantage of easy scalability [31-32]. In the USP method, when high-frequency ultrasonic waves pass through a liquid precursor solution and collide with the liquid-gas interface, a droplet aerosol of micrometer size is created.

The formation of droplets by ultrasound was first reported by R. W. Wood and A. L. Loomis in 1927, and Lang experimentally confirmed the relationship between ultrasound frequency and average droplet size in 1962. If a single particle is generated without the splitting and combining of droplets of the sprayed raw material solution, the generated droplet size can be estimated as [36]

$$D_{\text{droplet}} = 0.34\left(\frac{8\pi\gamma}{\rho f^2}\right)^{1/3} \tag{2-1}$$

where f is the frequency of the ultrasonic transducer, ρ is the density of the solution, and γ is the surface tension of the solution. Since the experiments are performed in very dilute solutions, the estimated ρ and γ values are equal to those of pure water. Assuming f = 1.7 MHz, γ = 0.0729 N/m, and ρ = 1000 kg/m^3, the droplet size is calculated as D_{droplet} = 2.92 μm from equation (2-1).

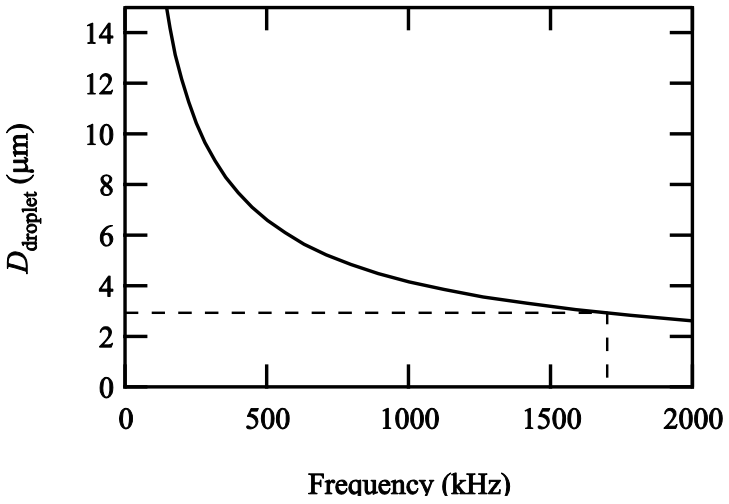

Figure 2-3 Droplet size by ultrasonic frequency intensity.

Laboratory-grade ultrasonic spray pyrolysis using high frequency (approximately 2 MHz) is very useful for fast hypothesis validation and facilitates small-scale synthesis of new materials. However, the intensity of ultrasonic waves on the surface of a high-frequency oscillator is not sufficient to spray solvents or slurries with high viscosity, density, and boiling point. Therefore, commercial devices that generate large amounts of droplets using high-intensity ultrasonic waves are on the market. These ultrasonic nozzles operate at frequencies of 20 to 120 kHz and are capable of producing droplets of different sizes (up to about 10 μm). Even liquids or slurries with high viscosity and low vapor pressure can be sprayed up to about 100 mL/min [33]. The yield and quality of the final product depends on the flow rate of gases and liquids through the reactor, the temperature in the reactor, the ultrasonic output solvent used, and the chemical composition of the precursor mixture. Very high yields can be obtained by changing the experimental parameters. Silica, titania, iron oxide, zinc oxide and various binary/ternary metal oxides can be prepared by all USP [37-41]. Also, Figure 2-3 shows the droplet size as a function of the frequency of the ultrasonic transducer.

2.2.1.2. Electrostatic collector

In the USP method, cyclones, electrostatics, and filters are generally used to collect the generated particles. In this study, an electrostatic collector was used and its schematic diagram is shown in Figure 2-4. Insect specimen stainless steel micro-needle (Shiga Konchu Co., Ltd., manufactured by 0.18 mm) was soldered to the terminal crimp using a special jig, and fixed with screws to be used as discharge electrodes. An aluminum plate was used for the particle collecting electrode of the flat plate. 5.00 kV DC power was applied using a high voltage power supply. Since the tip of the stainless-steel needles were worn by the discharge, the six discharge electrodes in the collector were wired three by three, and the discharge electrodes that applied voltage at 3 h were replaced. This enabled continuous collection for 6 hours. In order to prevent dew condensation inside the collector due to rapid cooling, the electrostatic collector was wrapped by a ribbon heater and the temperature of the collector was kept at 50 °C using a temperature controller.

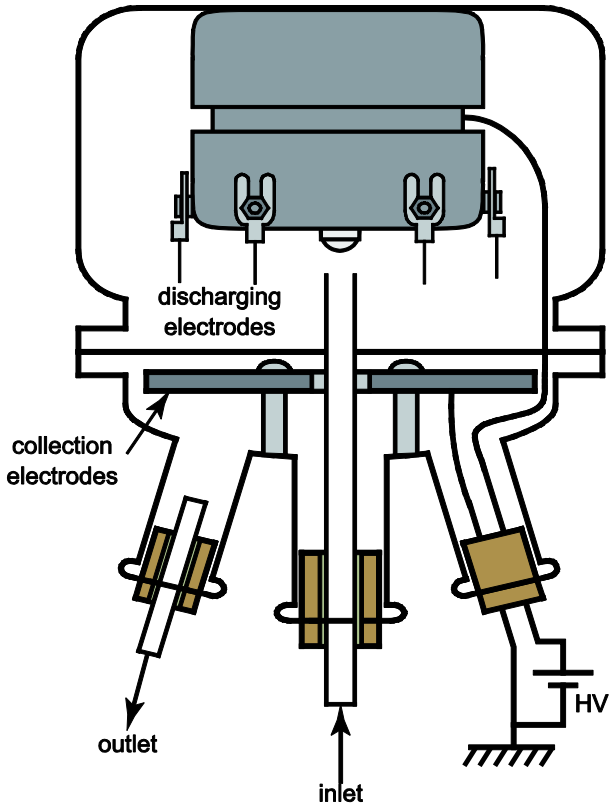

Figure 2-4 Schematic diagram of electrostatic collector.

2.3. Experimental setup and Method

ZnO particles were generated using the USP apparatus in Figure 2-1. $Zn(NO_3)_2\ 6H_2O$ was used as the zinc precursor. The precursor was dissolved to 100 ml distilled water with 2.5 to 10 mass% and the precursor solution was introduced into the nebulizer at a rate of 15 mL/h. An ultrasonic nebulizer (OMRON, NE-U17) with a resonance frequency of 1.7 MHz was used to spray the precursor solution. Droplets were introduced into the quartz glass reaction tube at a rate of 1.0 SLM by the carrier gas. The flow rate of sheath gas was fixed at 0.5 SLM to prevent droplet precipitation. The quartz glass reaction tube was installed inside four electric furnaces with a temperature controller of ±1 °C. And the temperature of the electric furnace was measured at between the inner wall of the furnace and the outer wall of a quartz glass reaction tube by thermocouples. The inner diameter, outer diameter, and length of the quartz glass reaction tube were 15.25, 18.25, and 1208.50 mm, respectively. These electric furnaces were used to heat the quartz reaction tube: two 80-mm preheating furnaces of No. 1 (40 °C) and No. 2 (70 °C), and two 290-nm long heating furnaces of No. 3 (150 °C or 1000 °C) and No. 4 (1000 °C). The particles obtained by decomposition of precursor solution droplets were then dried by a diffusion drier. Finally, particles were collected in the electrostatic precipitator.

2.3.1. Materials

Zinc nitrate hexahydrate ($Zn(NO_3)_2\ 6H_2O$, ≥99.0%) and chloroauric acid ($HAuCl_4$, ≥99.9%) were purchased from FUJIFILM Wako Pure Chemical Industries, and Rhodamine-B ($C_{28}H_{31}ClN_2O_3$, >95.0%) was purchased from Tokyo Chemical Industries. Titanium dioxide nanopowder as a standard photocatalyst (Evonik AEROXIDE® P25, formerly Degussa) was purchased from Sigma–Aldrich. All reagents were used as received without further purification. Distilled water was used in all experiments.

2.3.2. Characterization

The size distribution of ZnO particles was measured by laser diffraction spectrometry (Microtrac, MT3000EX). The size and shape of the ZnO particles were observed using a scanning electron microscope (SEM, JEOL JSM-6380A). X-ray diffraction (Rigaku, Multiflex) using Cu Kα radiation was used to examine the crystallite size and crystalline phase of the generated particles. The mean crystallite size of Au/ZnO composite particles was calculated using Scherrer's equation. The shape,

size, and elemental of Au/ZnO composite particles were observed by a transmission electron microscope (TEM, JEOL JEM-2100F) combined with energy dispersive X-ray spectroscopy (EDXS). The generated Au/ZnO composite particles were dispersed in water, and the UV-vis spectrum was analyzed using a spectrometer with an absorption wavelength of 200–850 nm (SIMAZU, UV-1800).

2.3.3. Photocatalytic activity

The photocatalytic activities of the synthesized powders were evaluated by photolysis of Rhodamine-B (RhB, Tokyo Chemical Industries) dyes. For each condition, 2–15 mg of particles and 100 ml of 5 mg/L RhB aqueous solution were mixed in a 250 ml beaker. The photocatalyst was ultrasonication for 10 minutes in an RhB aqueous solution and left in the dark for 5 minutes to establish an adsorption-desorption equilibrium between the photocatalyst and the dye before photocatalytic decomposition. And during UV light irradiation, the mixture was continuously stirred to maintain full suspension of the particles in the experiments. The photolysis reaction was performed under UV light irradiation from a single 15W lamp of 315–400 nm (TOSHIBA, FL15BL) located horizontally 65-mm above the liquid surface. A lux meter maintained the light intensity of the lamp. A 4-ml aliquot sample was extracted every 30 minutes. The residual dye concentration was measured after removal of the photocatalyst by precipitation. The photocatalyst precipitation process did not involve light irradiation. The change in the RhB concentration was analyzed by measuring the absorbance of the sample aliquots using a UV-Vis spectrophotometer. The concentration of RhB was analyzed by recording the change in the maximum absorption peak of RhB (555 nm).

2.3. Experimental Results and Discussion

2.3.1. Characteristics of ZnO particles

The estimated diameter of the generated ZnO particles can be calculated as

$$D_{\mathrm{ZnO}} = \sqrt[3]{\frac{D_{\mathrm{droplet}}^{3} C_{\mathrm{Zn(NO_3)_2\ aq.}} MW_{\mathrm{ZnO}}}{MW_{\mathrm{Zn(NO_3)_2}} \rho_{\mathrm{ZnO}}}} \tag{2-2}$$

where ρ_{ZnO} is the density of ZnO (5.606 × 10³ kg/m³), $MW_{\mathrm{Zn(NO_3)_2}}$ is the molecular weight of zinc nitrate (297.49 kg/kmol), MW_{ZnO} is the molecular weight of ZnO (81.37 kg/kmol), $C_{\mathrm{Zn(NO_3)_2\,aq.}}$ is the raw material concentration [g/L], and D_{ZnO} is the ZnO particle diameter [m]. The estimated diameter of the particles is calculated as 0.363–0.573 μm from the raw material concentration of 10–2.5 mass%.

The USP method often generates hollow or burst particles [24]. These not only hinder a uniform particle size distribution but are also susceptible to corrosion. Lenggoro *et al*. (2000) suggested that controlling the concentration of the raw material solution and the temperature of the furnace may realize dense particle generation [22]. Therefore, we attempted to generate dense particles by controlling these parameters. Table 2-2 lists the experimental conditions and the particle size distribution. Figure 2-5 shows the SEM observation result of the obtained particles.

Table 2-2 Experimental conditions and particle size distribution of ZnO particles.

Sample	Zinc Nitrate [mass%]	Temp. No.3 [°C]	D_{p10} [μm]	D_{p50} [μm]	D_{p90} [μm]	D_{p90}/D_{p10}	Estimated particle diameter [μm]
1	10	1000	0.415	0.608	1.332	3.21	0.573
2	5	1000	0.570	0.738	1.219	2.24	0.457
3	5	150	0.600	0.747	1.178	1.96	0.457
4	2.5	150	0.574	0.693	1.041	1.81	0.363

Sample 1 has a large particle size distribution (=D_{p90}/D_{p10}) of 3.21. This is consistent with the SEM image, which shows a mixture of dense and hollow particles. Samples 2, 3, and 4, which have a lower concentration of the raw material solution, show a narrower particle size distribution of 2.24, 1.96, 1.81, respectively. The SEM image of sample 4 indicates a distribution of small, dense, and narrow sized particles. Despite the small particle size and narrow size distribution, the particle size obtained under condition 4 is slightly larger than the estimated diameter obtained from equation (2). This slightly larger size is attributed to the generation of some larger particles by the combination of the initial spray droplets or the presence of a small number of hollow particles.

Figure 2-6 shows the XRD pattern of sample 4. All peaks of ZnO [(100), (002), (101), (102), (110), (103), (200) and (112)] are characteristic of the wurtzite (hexagonal) structure (JCPDS Card No:36-1451). Samples 1, 2, and 3 have similar XRD pattern to that shown in Figure 2-6. Additionally, the XRD peak did not change with furnace temperature or concentration.

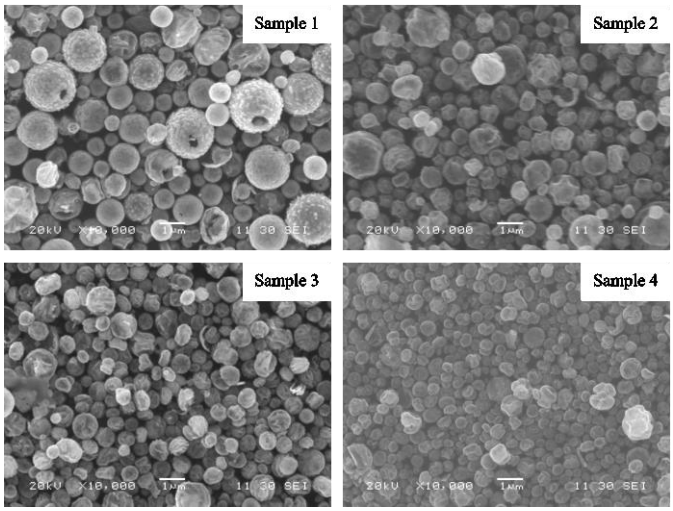

Figure 2-5 SEM images of ZnO particles obtained at different conditions.

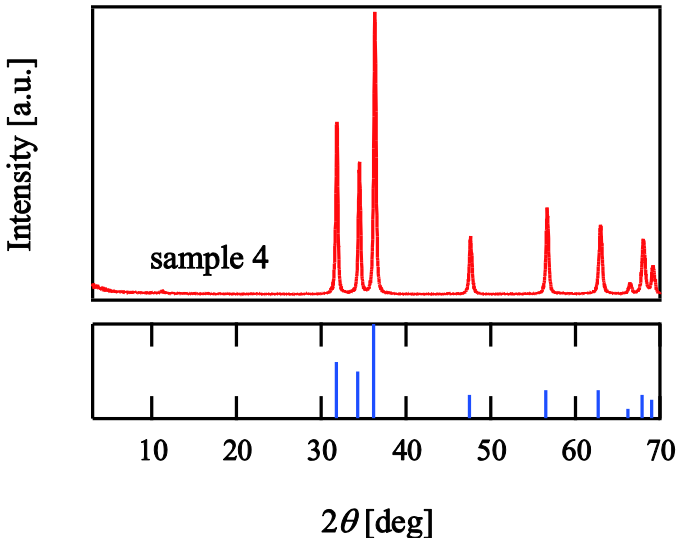

Figure 2-6 XRD pattern of ZnO particle (sample 4).

2.3.2. Characteristics of Au/ZnO particles

The Au/ZnO composite particles were generated using the same procedure as above, except chloroauric acid was added to the precursor solution. Because ZnO particles of sample 4 generated in the previous section were small and dense particles with a narrow size distribution, Au/ZnO particles were prepared using the same conditions as sample 4. Table 2-3 shows the experimental conditions to generate Au/ZnO composite particles and the Au crystallite size.

Table 2-3 Experimental concentrations of Au/ZnO composite particles and crystallite size of Au calculated by Scherrer's equation.

Sample	Concentration [mass%]		Crystallite size of Au (nm)
	$Zn(NO_3)_2$	$HAuCl_4$	
a	2.5	0.025	7.2
b		0.05	10.2
c		0.1	11.7
d		0.2	13.5

Figure 2-7 shows the XRD pattern of the obtained Au/ZnO particles. Similar to the XRD results of the ZnO particles shown in Figure 2-6, all samples display ZnO hexagonal peaks. Regardless of the Zn/Au molar ratio, the face-centered cubic structure of Au (JCPDS Card No:04-0784) appears in all Au/ZnO composite particles, suggesting that the metal form of Au is conserved in the composite particles. The peaks (111), (200), and (220), which are characteristic of the fcc structure of Au, decrease as the addition ratio of chloroauric acid decreases. Based on Scherrer's equation, the crystallite size of Au was calculated using (111) diffraction peak. The crystallite sizes of Au in samples a, b, c, and d are 7.2, 10.2, 11.7, and 13.5 nm, respectively. The small peak at $2\theta = 11$ ° is thought to be the result of the reaction of chlorine, which is separated when chloroauric acid decomposes, with intermediate products during pyrolysis. These results approximately correspond with the results of our previous study, which employed compressed air as the carrier gas [42].

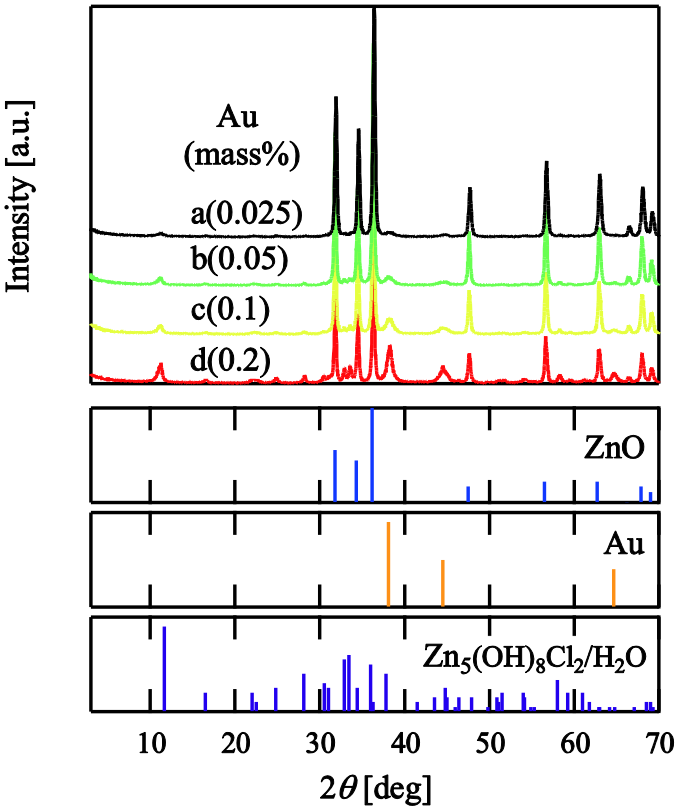

Figure 2-7 XRD pattern of Au/ZnO composite particles.

Figure 2-8 shows TEM images of samples a–d, which were generated at various concentrations of chloroauric acid. Dark spots are dispersed throughout the particle. The size of dark spots depends on the addition ratio of chloroauric acid. Therefore, we used EDX mapping to analyze the particle components.

Figure 2-9 shows the EDX mapping images and STEM image of sample d particle. The mapping image of the Au element and STEM image show that the dark spots on the particle correspond to Au. The presence of Zn and O throughout the particle means that small Au particles are dispersed throughout the ZnO particle. In other words, Figs. 2-8 and 2-9 complement the XRD results and indicate that the Au particles are preserved in the form of metal in the Au/ZnO composite. The Au particles identified by the EDX mapping imades of Sample d were measured through the STEM image. Sizes of about 60 Au particles were measured using a scale ruler in the STEM image, and the arithmetric mean size was 13.2 nm. This was in close agreement with the crystallite size obtained by Scheller's equation in the XRD pattern. This means that Au particles are dispersed as single crystals of metal in Au/ZnO composite.

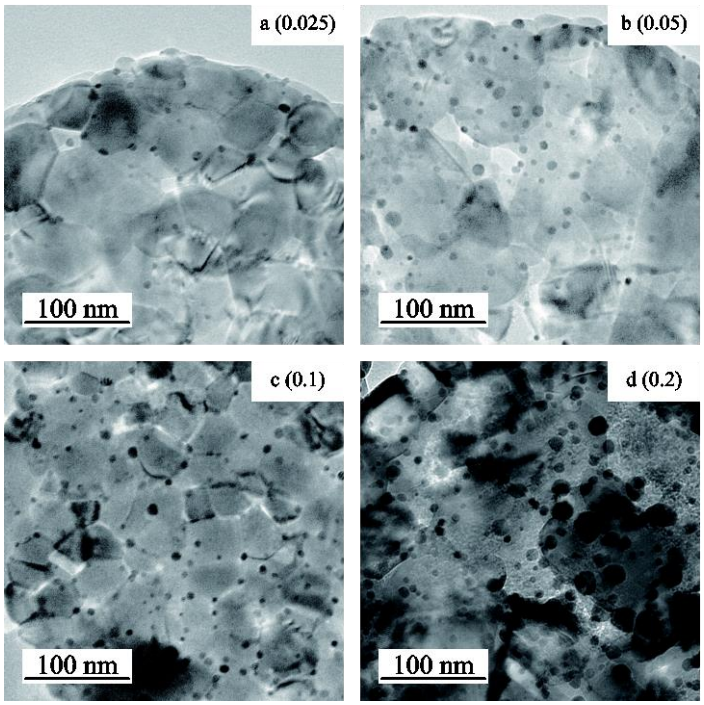

Figure 2-8 TEM images of Au/ZnO composite particles obtained by USP synthesis.

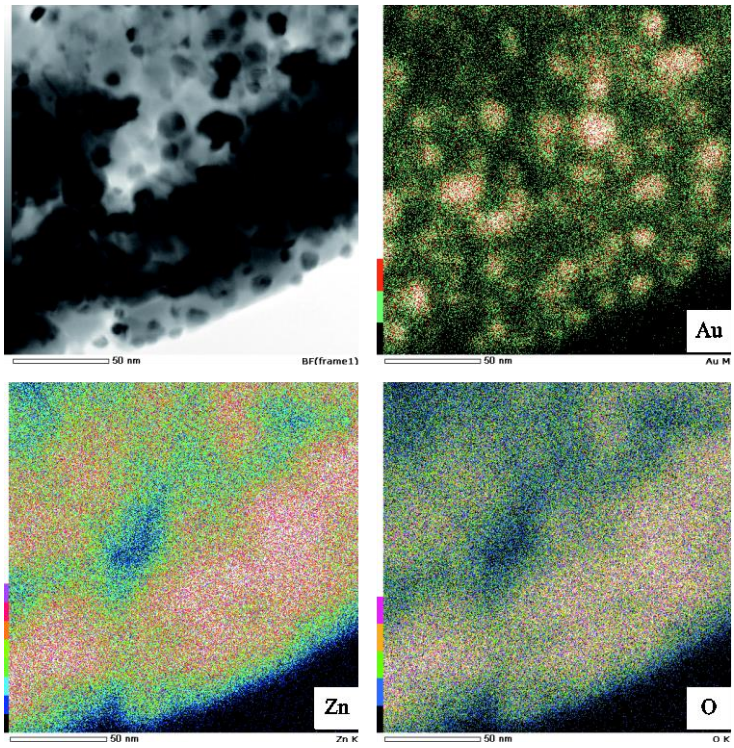

Figure 2-9 STEM image of sample d particle and the corresponding EDX mapping images of the Au, Zn, and O, respectively.

2.3.3. Photocatalytic activity

Assuming that the photolysis reaction of RhB is a first order reaction, the change in RhB concentration c can be expressed as

$$-\ln\frac{C}{C_0} = kt \tag{2-3}$$

where C_0, k, t are the initial concentration of the RhB, rate constant, and time, respectively.

Photocatalysis was performed by adding 5 mg of the photocatalyst in aqueous RhB. Figure 2-10 shows a semilogarithmic plot of the changes in the RhB concentration of ZnO (sample 4) particles and the Au/ZnO composite particles (samples a–d) as a function of UV light irradiation time. P25 was included here as a standard photocatalyst. The negligible concentration change of the RhB aqueous solution without a photocatalyst under UV irradiation for 180 minutes demonstrates that RhB is sufficiently stable in the photocatalytic activity analysis. All Au/ZnO composite particles show a higher photocatalytic activity than pure ZnO particles. However, sample d, which had 0.2 mass% of added chloroauric acid, shows a decreased photocatalytic activity. The removal of organic matter

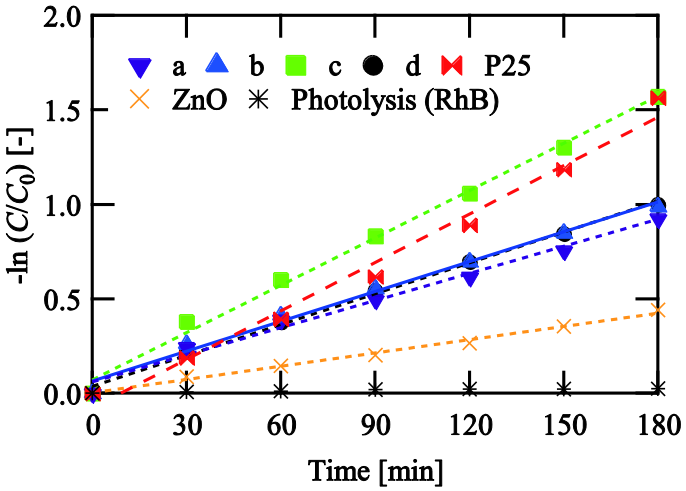

Figure 2-10 Semilogarithmic plot of changes in RhB concentration by UV light irradiation time at ZnO (Sample 4), samples a-d, and P25; initial concentration of RhB: 5mg/L; photocatalyst dose: 5mg; solution volume: 100ml.

using a photocatalyst is an issue in the field of water purification because photocatalyst performance deteriorates over time and toxicity of photocatalysts may be released. Although the decomposition activity of our particles is similar to that of P25, they can be easily removed from water by means of gravitational sedimentation after the decomposition of organic pollutants because the particles produced by the USP method have a relatively large particle size.

Table 2-4 First-order reaction rate constant k and the coefficient of determination R^2 corresponding to the slope of the line.

Samples	Reaction rate constant, k [min^{-1}]	Coefficient of determination, R^2
a	0.00479	0.987
b	0.00527	0.990
c	0.00835	0.994
d	0.00544	0.996
ZnO	0.00234	0.993
P25	0.00855	0.985

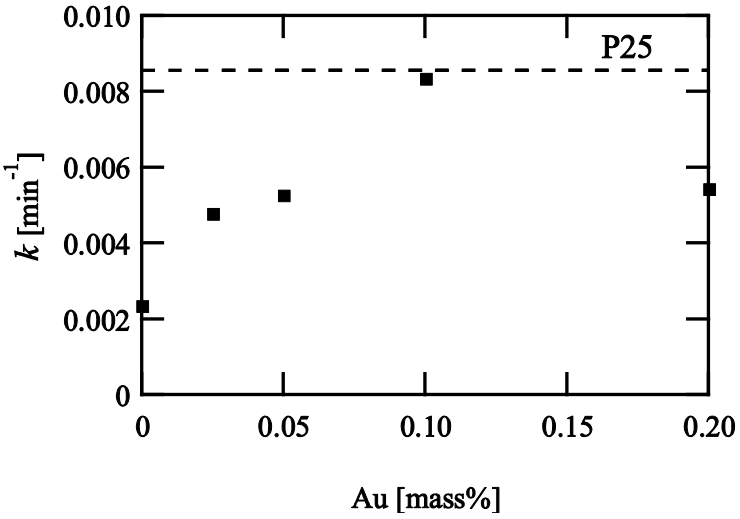

Figure 2-11 First-order reaction rate constant for RhB photolysis using ZnO (Sample 4), samples a-d, and P25 under UV light irradiation; initial concentration of RhB: 5 mg/L; photocatalyst dose: 5 mg; solution volume: 100 ml.

Table 2-4 shows the first-order reaction rate constant k and the coefficient of determination R^2 corresponding to the slope of the line. And the first-order reaction rate constant k is graphically plotted in Figure 2-11. From the result of the coefficient of determination shown in Table 2-4 is close to 1, the photolysis reaction can be considered to be a first-order reaction. Compared to pure ZnO particles, samples a, b, and c have about 2.5 times higher photolysis rate constants, while that for sample c is about 4 times higher. Although sample d had a higher amount of Au than that of sample c, the photolysis rate constant is about half that of sample c. From the TEM analysis of Figure 2-8, the number and particle size of Au nanoparticles deposited on ZnO particles increases as the amount of supported Au increases. However, when an excessive amount of Au nanoparticles is supported onto ZnO particles, Au nanoparticles act as recombination centers for excitation electrons. This leads to a decrease in photocatalytic activity [15, 43].

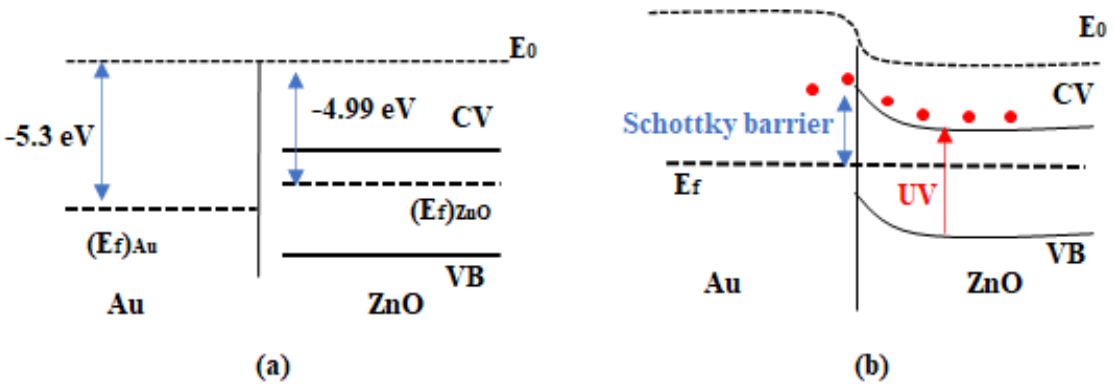

Figure 2-12 (a) Fermi level of ZnO and Au particles before compounding, (b) Fermi level of ZnO and Au particles after compounding. E_0:vacuumlevel; $(E_f)_{Au}$, $(E_f)_{ZnO}$, E_f: Fermi levels of Au, ZnO, and Au/ZnO; CV and VB : conduction band and valence band of ZnO.

This change in photocatalytic activity can be explained by the change in the Fermi level of ZnO and Au nanoparticles. Figure 2-12 shows the change in Fermi level due to contact between ZnO and Au particles. As shown in Fig. 2-12(a), the Fermi levels of ZnO and Au particles before contact differed by -5.3 and -4.99 eV, respectively. When ZnO and Au particles come into contact, it becomes Fermi level as shown in Fig. 2-12 (b), and the Schottky barrier is formed because the Fermi level of ZnO is relatively high. And since the voltage of the excited electrons is higher than the Schottky barrier, they can migrate to the Au particles, and the Au particles can act as a sink for the electrons. However, as the Au particles grow, the Fermi level decreases due to the quantum size effect [44].

Therefore, the larger the Au particle, the higher the Schottky barrier and may decrease the number of excited electrons migrate to the Au particle. That is, when ZnO and Au particles come into contact, a Schottky barrier is created, and if the voltage of the excited electrons is sufficiently higher than the Schottky barrier, the photolytic activity increases with the increase of Au support. However, when an excessive amount of Au nanoparticles is supported onto ZnO particles, the excited electrons cannot pass through the increased Schottky barrier and can recombine. Therefore, the number of excitons decreases, resulting in a decrease in photocatalytic activity.

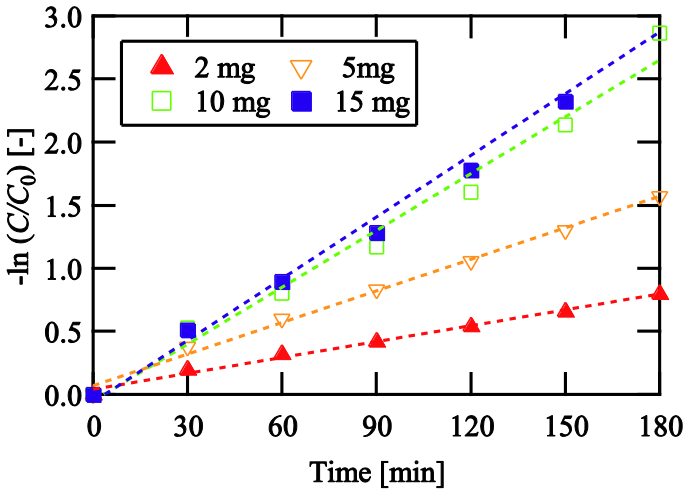

Figure 2-13 Semilogarithmic plot of changes in RhB concentration by UV light irradiation time at different photocatalyst dose of Sample c; initial concentration of RhB: 5 mg/L; solution volume: 100 ml.

To confirm the photolysis rate by the sample c dose, 2−15 mg of the photocatalyst was added to RhB aqueous solution. Figure 2-13 shows the semilogarithmic plot of the changes in the RhB concentration as a function of UV light irradiation time. The first-order reaction rate constant depends on the photocatalyst dose. The first-order reaction rate constant k and the coefficient of determination R^2 are shown in Figures 2-14 and 2-5.

The photocatalytic activity gradually improves with the increased sample c dose. The activity of the photocatalyst increases from 2–10 mg in proportion to the amount of the sample. However, doses above 10 mg (e.g., 15 mg) do not significantly enhance the activity. These results indicate that the turbidity of the suspension affects the photocatalytic activity. The turbidity of the suspension can cutoff the UV light, reducing the excitons, which are important for photocatalytic activity [45–46].

Our study results were compared with the recently reported Au/ZnO particle study in Table 2-6, and it indicates that our particles have a competitive performance compared to other studies. Because the USP method employed in this study is possible to generate particles in one step without post-treatment, it has the advantage of less agglomeration between particles compared to other methods such as the wet method. We succeeded in producing Au/ZnO particles with little aggregation using the USP method and proved that Au nanoparticles exist as single crystals in ZnO particles. Haugen *et al*. confirmed that the size of the doped Au or Ag crystals increased and the photocatalytic activity decreased after calcination of the particles. It was suggested that the photocatalytic activity of large sized Au or Ag crystals was decreased because they acted as the center of hole-electron recombination [20]. That is, through this study, competitive Au/ZnO particles were produced, and it is considered that the approach in the field of organic wastewater and application to other fields are possible.

Table 2-5 First-order reaction rate constant k and the coefficient of determination R^2 for dose.

Dose [mg]	Reaction rate constant, k [min^{-1}]	Coefficient of determination, R^2
2	0.00420	0.992
5	0.00835	0.994
10	0.01502	0.981
15	0.01629	0.989

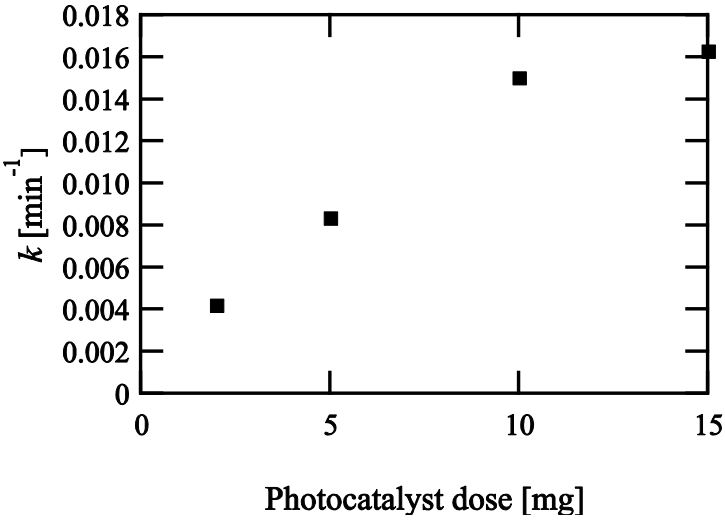

Figure 2-14 First-order reaction rate constant for RhB photolysis using different photocatalyst dose of Sample c under UV light irradiation; initial concentration of RhB: 5mg/L; solution volume: 100ml.

Table 2-6 Photocatalytic activity of Au/ZnO system.

Dye	UV Light	Initial dye conc. [M]	Catalyst conc. [mg/ml]	k [min^{-1}]	Au/ZnO [mol)	Ref.
MB	8W×2	2×10^{-5}	1.50	0.0019	0.0204	T.K. Pathak *et al*. [17]
MB	15W×2	3×10^{-5}	0.10	0.019	0.0306	P. Pawinrat *et al*. [18]
RhB	30W	3×10^{-5}	0.05	0.00206	0.0163	J. Kim *et al*. [19]
Orange II	8W	2.85×10^{-5}	1.50	0.0119	0.0096	P.K. Chen *et al*. [47]
RhB	15W	1.04×10^{-5}	0.10	0.01502	0.0222	This study

2.4 Conclusion

In this study, the USP method was used to generate ZnO and Au/ZnO particles under various conditions. All ZnO exhibited a hexagonal structure. Under the proper conditions, small, dense, and narrow sized ZnO particles were generated. XRD patterns of Au/ZnO particles revealed the structural patterns of ZnO and Au. The peak height of Au changed with the amount of supported Au. The TEM images showed dark spots dispersed throughout the Au/ZnO particles. The size of the dark spots varied with the concentration of chloroauric acid in the precursor solution. EDX mapping and STEM images confirmed that the dark spots corresponded to nano-sized Au particles dispersed throughout the ZnO particles.

The photolysis of the RhB aqueous solution was investigated under UV light irradiation. Under all conditions, Au/ZnO particles showed a better photocatalytic activity than ZnO particles. The photolysis rate constant increased as the Au loading increased from 0.025 mass% to 0.1 mass%. However, the photolysis rate constant decreased for 0.2 mass% Au. The excess Au loading may accumulate excess exciton electrons, attract holes, and promote the recombination of electron-hole due to the large contact surface with ZnO particles.

Hence, Therefore, the photolysis activity by the dose of the photocatalyst was investigated. The photocatalytic activity increased in proportion to the dose from 2 mg to 10 mg, but it did not change significantly at higher doses. In other words, UV light, which is important for electron excitation, was

blocked in the turbid suspension. Lastly, the best photocatalytic activity was observed in particles with a 0.1 mass% Au supported on ZnO particles. Moreover, the USP could simply generate particles in one step. Although decomposition experiments on actual wastewater were beyond the scope of this study, the potential of purifying organic pollutants using this material was confirmed.

2.5. References

1. T. Sauer, G. Cesconeto Neto, H.J. José, R.F.P.M. Moreira, Kinetics of photocatalytic degradation of reactive dyes in a TiO_2 slurry reactor, Journal of Photochemistry and Photobiology A: Chemistry, 149 (2002) 147-154.
2. C. Galindo, P. Jacques, A. Kalt, Photooxidation of the phenylazonaphthol AO20 on TiO_2: kinetic and mechanistic investigations, Chemosphere, 45 (2001) 997-1005.
3. K. Tanaka, K. Padermpole, T. Hisanaga, Photocatalytic degradation of commercial azo dyes, Water Research, 34 (2000) 327-333.
4. T. Welderfael, O.P. Yadav, A.M. Taddesse, J. Kaushal, Synthesis, characterization and photocatalytic activities of Ag–N-codoped ZnO nanoparticles for degradation of methyl red, The Bulletin of the Chemical Society of Ethiopia, 27 (2013) 221–232.
5. F. Han, V.S.R. Kambala, M. Srinivasan, D. Rajarathnam, R. Naidu, Tailored titanium dioxide photocatalysts for the degradation of organic dyes in wastewater treatment: A review, Applied Catalysis A: General, 359 (2009) 25–40.
6. V. Vaiano, M. Matarangolo, O. Sacco, D, Sannino, Photocatalytic treatment of aqueous solutions at high dye concentration using praseodymium-doped ZnO catalysts, Applied Catalysis B: Environmental, 209 (2017) 621–630.
7. M.J. Height, S.E. Pratsinis, O. Mekasuwandumrong, P. Praserthdam, Ag-ZnO catalysts for UV-photodegradation of methylene blue, Applied Catalysis B: Environmental, 63 (2006) 305–312.
8. D. Nipane, S.R. Thakare, N.T. Khati, Synthesis of Novel ZnO Having Cauliflower Morphology for Photocatalytic Degradation Study, Journal of Catalysts, 77 (2013) 1-8.
9. H. Wang, H.L. Wang, W.F. Jiang, Z.O. Li, Photocatalytic degradation of 2,4-dinitrophenol (DNP) by multi-walled carbon nanotubes (MWCNTs)/TiO_2 composite in aqueous solution under solar irradiation, Water Research, 43 (2009) 204-210.

10. Q. Zhou, Y.H. Zhong, X. Chen, J.H. Liu, X.J. Huang, Y.C. Wu, Adsorption and photocatalysis removal of fulvic acid by TiO_2–graphene composites, Journal of Materials Science, 49 (2014) 1066–1075.

11. R. Asahi, T. Morikawa, T. Ohwaki, K. Aoki, Y. Taga, Visible-light photocatalysis in nitrogen-doped titanium oxides, Science, 293 (2001) 269-271.

12. P. Sathishkumar, R. Sweena, J.J. Wu, S. Anandan, Synthesis of CuO-ZnO nanophotocatalyst for visible light assisted degradation of a textile dye in aqueous solution, Chemical Engineering Journal, 171 (2011) 136-140.

13. A. Franco, M.C. Neves, R. M.M.L. Ribeiro Carrott, M.H. Mendonça, M.I. Pereira, O.C. Monteiro, Photocatalytic decolorization of methylene blue in the presence of TiO_2/ZnS nanocomposites, Journal of Hazardous Materials, 161 (2009) 545-550.

14. S. Ameen, M. Shaheer Akhtar, Y.S. Kim, O.B. Yang, H.S. Shin, An effective nanocomposite of polyaniline and ZnO: preparation, characterizations, and its photocatalytic activity, Colloid and Polymer Science, 289 (2011) 415-421.

15. V. Vaiano, M. Matarangolo, J.J. Murcia, H. Rojas, J.A. Navío, M.C. Hidalgo, Enhanced photocatalytic removal of phenol from aqueous solutions using ZnO modified with Ag, Applied Catalysis B: Environmental, 225 (2018) 197-206.

16. Y.H. Lu, M. Xu, L.X. Xu, C.L. Zhang, Q.P. Zhang, X.N. Xu, S. Xu, K. Ostrikov, Enhanced ultraviolet photocatalytic activity of Ag/ZnO nanoparticles synthesized by modified polymer-network gel method, Journal of Nanoparticle Research, 17 (2015) 1-15.

17. T.K. Pathak, R.E. Kroon, H.C. Swart, Photocatalytic and biological applications of Ag and Au doped ZnO nanomaterial synthesized by combustion, Vacuum, 157 (2018) 508-513.

18. P. Pawinrat, O. Mekasuwandumrong, J. Panpranot, Synthesis of Au–ZnO and Pt–ZnO nanocomposites by one-step flame spray pyrolysis and its application for photocatalytic degradation of dyes, Catalysis Communications, 10 (2009) 1380-1385.

19. J. Kim, K. Yong, A facile, coverage controlled deposition of Au nanoparticles on ZnO nanorods by sonochemical reaction for enhancement of photocatalytic activity, Journal of Nanoparticle Research, 14 (2012) 1-10.

20. A.B. Haugen, I. Kumakiri, C. Simon, M.A. Einarsrud, TiO_2, TiO_2/Ag and TiO_2/Au photocatalysts prepared by spray pyrolysis, Journal of the European Ceramic Society, 31

(2011) 291-298.

21. B. Ebin, E. Arıg, B. Özkal, S. Gürmen, Production and characterization of ZnO nanoparticles and porous particles by ultrasonic spray pyrolysis using a zinc nitrate precursor, International Journal of Minerals, Metallurgy and Materials, 19 (2012) 651-655.

22. W.I. Lenggoro, T. Hata, F. Iskandar, An experimental and modeling investigation of particle production by spray pyrolysis using a laminar flow aerosol reactor, Journal of Materials Research, 15 (2000) 733-743.

23. T.Q. Liu, O. Sakurai, N. Mizutani, M. Kato, Preparation of spherical fine ZnO particles by the spray pyrolysis method using ultrasonic atomization techniques, Journal of Materials Science, 21 (1986) 3698-3702.

24. K. Okuyama, W.I. Lenggoro, Preparation of nanoparticles via spray route, Chemical Engineering Science, 58 (2003) 537-547.

25. K. Okuyama, D. Huang, J.H. Seinfeld, N. Tani, Y. Kousaka, Aerosol formation by rapid nucleation in the preparation of SiO_2 thin film from $SiCl_2$ and O_2 gases using CVD process, Chemical Engineering Science, 46 (1991) 1545–1560.

26. K. Kaneko, W.J. Moon, K. Inoke, Z. Horita, S. Ohara, T. Adschiri, H. Abe, M. Naito, Characterization of TiO_2–Ag nanocomposite particles prepared by spray pyrolysis process using transmission electron microscopy and three-dimensional electron tomography, Materials Science and Engineering A, 403 (2005) 32-36.

27. O. Milošević, D. Uskoković, L.J. Karanović, M. Tomašević-Čanović, M. Trontelj, Synthesis of ZnO-based varistor precursor powders by means of the reaction spray process, Journal of Materials Science, 28 (1993) 5211-5217.

28. K. Leong, Morphological control of particles generated from the evaporation of solution droplets: experiment, Journal of Aerosol Science 18 (1987) 525–552.

29. K. Masters, Spray drying handbook, Longman Scientific & Technical, London, 1994.

30. A.J. Hewitt, Droplet size spectra produced by air-assisted atomizers, Journal of Aerosol Science 24 (1993) 155–162.

31. A.B.D. Nandiyanto, K. Okuyama, Progress in developing spray-drying methods for the production of controlled morphology particles: From the nanometer to submicrometer size ranges, Advanced Powder Technology, 22 (2011) 1-19.

32. J.H. Bang, K.S. Suslick, Applications of Ultrasound to the Synthesis of Nanostructured Materials, Advanced Materials, 22 (2010) 1039-1059.

33. J.H Bang, Y.T. Didenko, R.J Helmich, K.S. Suslick, Nanostructured Materials Through Ultrasonic Spray Pyrolysis, Material Matters, 7 (2012) 15-20

34. S. Gan-Mor, G.A. Matthews, Recent Developments in Sprayers for Application of Biopesticides — an Overview, Biosystems Engineering, 84 (2003) 119-125.

35. M.B. Adali, A.A. Barresi, G. Boccardo, R. Pisano, Spray Freeze-Drying as a Solution to Continuous Manufacturing of Pharmaceutical Products in Bulk, Processes, 8 (2020) 1-27.

36. R.J. Lang, Ultrasonic atomization of liquids, Journal of the Acoustical Society of America, 34 (1962) 6-8.

37. G.L. Messing, S.C. Zhang, G.V. Jayanthi, Ceramic Powder Synthesis by Spray Pyrolysis, Journal of the American Ceramic Society, 76 (1993) 2707-2726.

38. W.H. Suh, K.S. Suslick, Magnetic and Porous Nanospheres from Ultrasonic Spray Pyrolysis, Journal of the American Chemical Society, 127 (2005) 12007-12010.

39. W.H. Suh, A.R. Jang, Y.H. Suh, K.S. Suslick, Porous, Hollow, and Ball-in-Ball Metal Oxide Microspheres: Preparation, Endocytosis, and Cytotoxicity, Advanced Materials, 18 (2006) 1832-1837.

40. W.H. Suh, K.S Suslick, Y.H. Suh, Therapeutic Agents for Alzheimer's Disease, Current Medicinal Chemistry - Central Nervous System Agents, 5 (2005) 259-269.

41. F. Iskandar, Mikrajuddin, K. Okuyama, Controllability of Pore Size and Porosity on Self-Organized Porous Silica Particles, Nano Letters, 2 (2002) 389-392.

42. Y.J. Lee, T. Fujimoto, S. Yamanaka, Y. Kuga, Formation and Evaluation of Au/ZnO Particles by Spray Pyrolysis Method, MATEC Web Conf. 333, Proc. 18th Asian Pacific Confederation of Chemical Engineering Congress (APCChE 2019), 02010 (2021).

43. W. Lu, G. Liu, S. Gao, S. Xiong, J. Wang, Tyrosine-Assisted Preparation of Ag/ZnO Nanocomposites with Enhanced Photocalytic Performance and Synergitic Antibacterial Activities, Nanotechnology, 19 (2009) 445711

44. S. Shuang, Z. Zhang, The Effect of Annealing Treatment and Atom Layer Deposition to Au/Pt Nanoparticles-Decorated TiO2 Nanorods as Photocatalysts, Molecules, 23 (2018) 1-

11.

45. B. Neppolian, H.C. Choi, S. Sakthivel, B. Arabindoo, V. Murugesan, Solar light induced and TiO2 assisted degradation of textile dye reactive blue 4, Chemosphere, 46 (2002) 1173-1181.

46. C. Lu, Y. Wu, F. Mai, W. Chung, C. Wu, W. Lin, C. Chen, Degradation efficiencies and mechanisms of the ZnO-mediated photocatalytic degradation of Basic Blue 11 under visible light irradiation, Journal of Molecular Catalysis A, 310 (2009) 159-165.

47. P.K. Chen, G.J. Lee, S.H. Davies, S.J. Masten, R. Amutha, J.J. Wu, Hydrothermal synthesis of coral-like Au/ZnO catalyst and photocatalytic degradation of Orange II dye, Materials Research Bulletin, 48 (2013) 2375-2382.

Chapter 3 Evaluation of Photocatalysis of Ag Supported ZnO Prepared by the Spray Pyrolysis Method

3.1. Introduction

In Chapter 2, it was confirmed that the Au nanoparticles doped on the ZnO particles act as electron sinks to delay the recombination of excited electrons and holes, thereby they increased the efficiency of the photocatalyst. Noble metals include Pt [1-2], Pd [3], and Ag [4-10], and are reported to act as electron sinks like Au. However, because the noble metals are expensive, industrial applications may have significant limitations. Therefore, relatively inexpensive Ag-supported research is attracting attention. In addition, several studies have shown that Ag/ZnO photocatalysts have higher photolysis efficiency than Au/ZnO. For example, Senthilraja *et al*. generated Au/ZnO, Ag/ZnO, and Au/Ag/ZnO particles by a precipitation–decomposition method, and as a result of Methylene blue (MB) dye photolysis experiments, Ag/ZnO particles showed higher photolysis efficiency than Au/ZnO particles [11]. Pathak *et al*. generated Au/ZnO and Ag/ZnO particles doped at a concentration of 2 mol% Ag and Au using a combustion method. In addition, by MB dye photolysis experiments, it was confirmed that Ag/ZnO particles have better photocatalytic efficiency than Au/ZnO particles [12]. Interestingly, Zhai *et al*. generated Au/ZnO, Ag/ZnO, Au/Ag/ZnO particles by photo-deposition procedure and low-temperature calcination method, and performed ethylene photolysis experiments for the application of preservation of fruits and vegetables. It has been proven that Ag/ZnO particles have better ethylene decomposition efficiency than Au/ZnO [13]. In addition, a study on the generation and characteristic comparison of Ag/ZnO and Au/ZnO particles using the microwave and ultrasonic combined technique [14] and the borohydride reduction method [15] have been reported.

However, as previously explained, the nanoparticles generated by those kinds of methods have a large specific surface area, so the photocatalytic efficiency is good, but it is difficult to be collected after use. Hence, the inability to recycle photocatalytic particles not only increases the cost but can lead to new pollution [16-17]. In Chapter 2, it was confirmed that the Ultrasonic Spray Pyrolysis (USP) method was used to generate submicron-level Au/ZnO particles with photocatalytic activity similar to P25 and that they could be collected simply by a gravity sedimentation. In addition, since the USP method is a continuous one-step process, the high-purity powder can be produced simply, and since there is no post-treatment, agglomeration between particles can be suppressed as much as possible [18]. Therefore, in this chapter, it is reported generation of submicron-level Ag/ZnO particle by using

the USP method and evaluations of photocatalytic efficiency. In addition, the morphology and structural properties of the obtained particles were investigated, and the reusability of particles through gravity sedimentation was investigated.

3.2. Experimental setup and Method

3.2.1. Materials

Zinc nitrate hexahydrate ($Zn(NO_3)_2$ $6H_2O$, ≥99.0%) and silver nitrate ($AgNO_3$, ≥99.8%) were purchased from FUJIFILM Wako Pure Chemical Industries, and Rhodamine-B (RhB, $C_{28}H_{31}ClN_2O_3$, >95.0%) was purchased from Tokyo Chemical Industries. Titanium dioxide nanopowder as standard photocatalyst (Evonik AEROXIDE® P25, formerly Degussa) was purchased from Sigma–Aldrich. All reagents were used as received without further purification. Distilled water was used in all experiments.

3.2.2. Synthesis of Ag/ZnO composite particles

Ag/ZnO composite particles were synthesized using the USP method as described in Chapter 2. Therefore, the device and its operation method are briefly described here. The USP apparatus was composed of a nebulizer with a resonance frequency of 1.7 MHz, a quartz glass reaction tube, four electric furnaces with a temperature controller of ±1 °C, a diffusion dryer, and an electrostatic precipitator. The Zinc nitrate hexahydrate were dissolved in 100 mL of distilled water with concentration maintained at 2.5 mass%. And silver nitrate concentration ranged between 0 and 0.4 mass% was added into the precursor solution. The rate introduced into the nebulizer of precursor solution was 15 mL/h. The generated droplets by nebulizer were introduced into the quartz glass reaction tube using a nitrogen flow at a rate of 1.0 SLM. And flow rate of sheath gas to prevent precipitation was fixed at a rate of 0.5 SLM. Four electric furnaces for heating the quartz reaction tube were used, two 80 mm preheating furnaces from the bottom were set to 40 °C and 70 °C, respectively, and two 290 nm heating furnaces were set to 150 °C and 1000 °C. The length, outer diameter, and inner diameter of the quartz glass reaction tube were 1208.50 mm, 18.25, and 15.25, respectively, and the temperature was measured between the outer wall of the quartz glass reaction tube and the inner wall of the furnace. The synthesized Ag/ZnO composite particles by the decomposition of droplets were then dried by a diffusion drier. Afterward the Ag/ZnO composite

particles were collected in the electrostatic precipitator.

3.2.3. Characterization

The size and morphology of the particles were verified using a scanning electron microscope (SEM, JEOL JSM-6380A). Crystallite size and crystalline phase of the generated particles were studied by X-ray diffraction (Rigaku, Multiflex) using Cu Kα radiation. The crystallite size of the Ag and ZnO particles was estimated using Scherrer's equation. The particle size, morphology, and elemental were recorded by a transmission electron microscope (TEM, JEOL JEM-2100F) equipped with energy-dispersive X-ray spectroscopy (EDXS). To study the optical properties, the change in concentration of the RhB solution decomposed by the Ag/ZnO composite particles was measured using a spectrometer with an absorption wavelength of 200–850 nm SIMAZU, UV-1800).

Table 3-1 Experimental concentrations of ZnO and Ag/ZnO particles and crystallite size calculated by Scherrer's equation.

Sample	Concentration [mass%]		Crystallite size of Ag (nm)	Crystallite size of ZnO (nm)
	$Zn(NO_3)_2$	$AgNO_3$		
a	2.5	-	-	35.6
b		0.05	15.7	34.2
c		0.1	16.1	31.5
d		0.2	16.3	30.6
e		0.4	22.9	31.2

3.3. Experimental Results and Discussion

3.3.1. Characteristics of Ag/ZnO particles

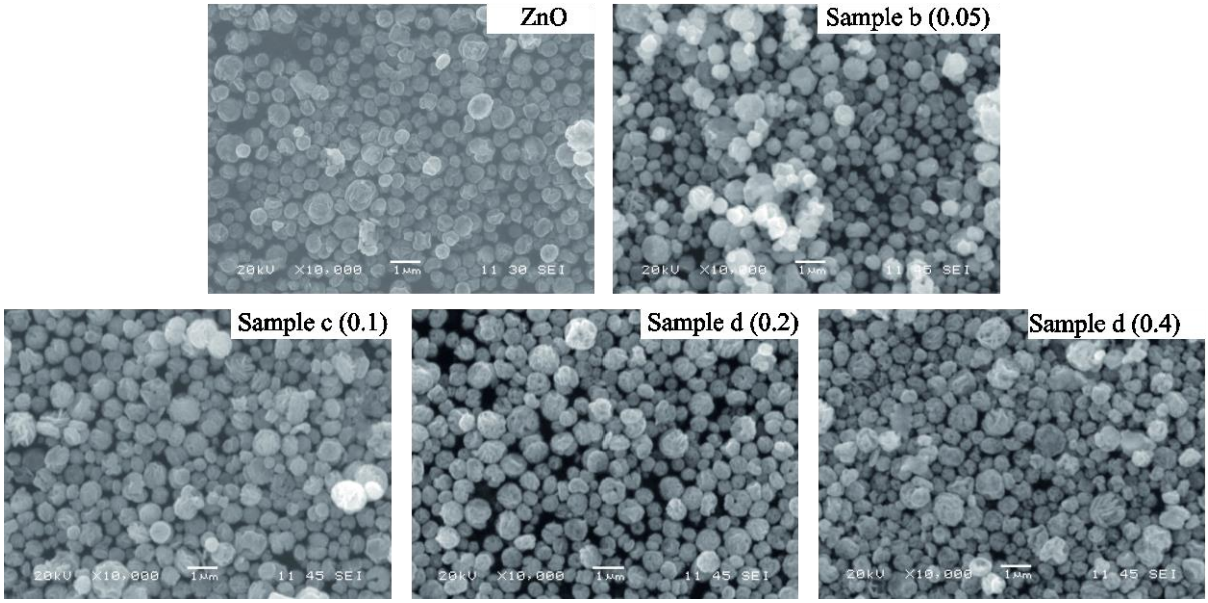

Figure 3-1 SEM images of samples a-e obtained at different conditions.

In our previous study, small and dense particles were generated using the USP method, and Au/ZnO particles were successfully generated. Figure 3-1 shows the SEM images of particles (sample a) and Ag/ZnO particles (sample b-d) generated under various conditions. The SEM images show that the generated Ag/ZnO particles are small and dense particles like the Au/ZnO particles of the previous study, and there was no change in the size and shape of the particles by the concentration of silver nitrate. In addition, the particle size has a distribution of 0.5 to 1.0 μm and has a spherical shape.

Figure 3-2 shows the XRD pattern of the obtained ZnO and Ag/ZnO particles by the USP method. Diffraction peaks of all samples [(100), (002), (101), (102), (110), (103), (200), and (112)] are characteristic of the wurtzite structure of ZnO (JCPDS Card No:36-1451). And diffraction peaks (111), (200), and (220), which are characteristic of the fcc structure of Ag (JCPDS Card No:04-0783), were identified in all samples generated with silver nitrate, and the height of the peaks increased as the addition ratio of silver nitrate increased. The peaks of Ag appear regardless of the Zn/Ag molar ratio, and the peaks of other intermediate products were not observed. Thus, it suggests that Ag exists as a

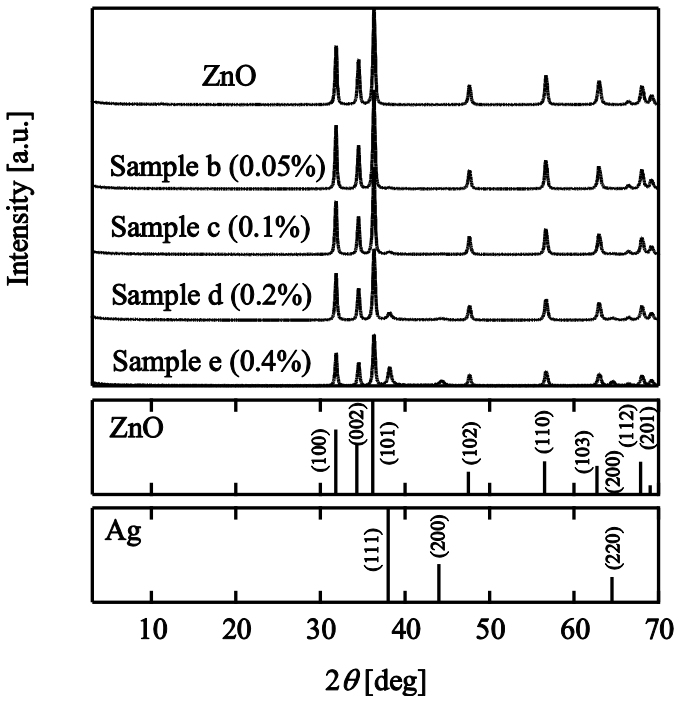

Figure 3-2 XRD pattern of ZnO and Ag/ZnO particles.

metallic form in all Ag/ZnO composite particles.

The ZnO crystallite size and Ag crystallite size of the sample were calculated using the Scherrer equation and are shown in Table 3-1. The (101) diffraction peak of ZnO and the (111) diffraction peak of Ag were used for calculation. The Ag crystallite size of the Ag/ZnO sample increased from 15.7 to 22.9 nm as the addition rate of silver nitrate increased. Conversely, the ZnO crystallite size did not change significantly with the addition of silver nitrate.

Figure 3-3 shows TEM images of pure ZnO and Ag/ZnO particles prepared by adding silver nitrate at various concentrations to the raw material solution. When ZnO is doped with Ag (silver nitrate: 0.05-0.4 mass%), dark spots were found on inside and outside of Ag/ZnO particles as shown in Fig. 3-3(b-e). The dark spots were not observed in Fig. 3-3(a), which is a TEM image of ZnO particles (Sample a) and tends to increase from Fig. 3-3 (b) to (e) due to the increase in the concentration of silver nitrate. This is a similar result to our previous study in which ZnO was doped with Au, and it could be assumed that the dark spots were a metal particle. Therefore, the particle composition was analyzed using EDX mapping to confirm whether the dark spot was an Ag nanoparticle or not.

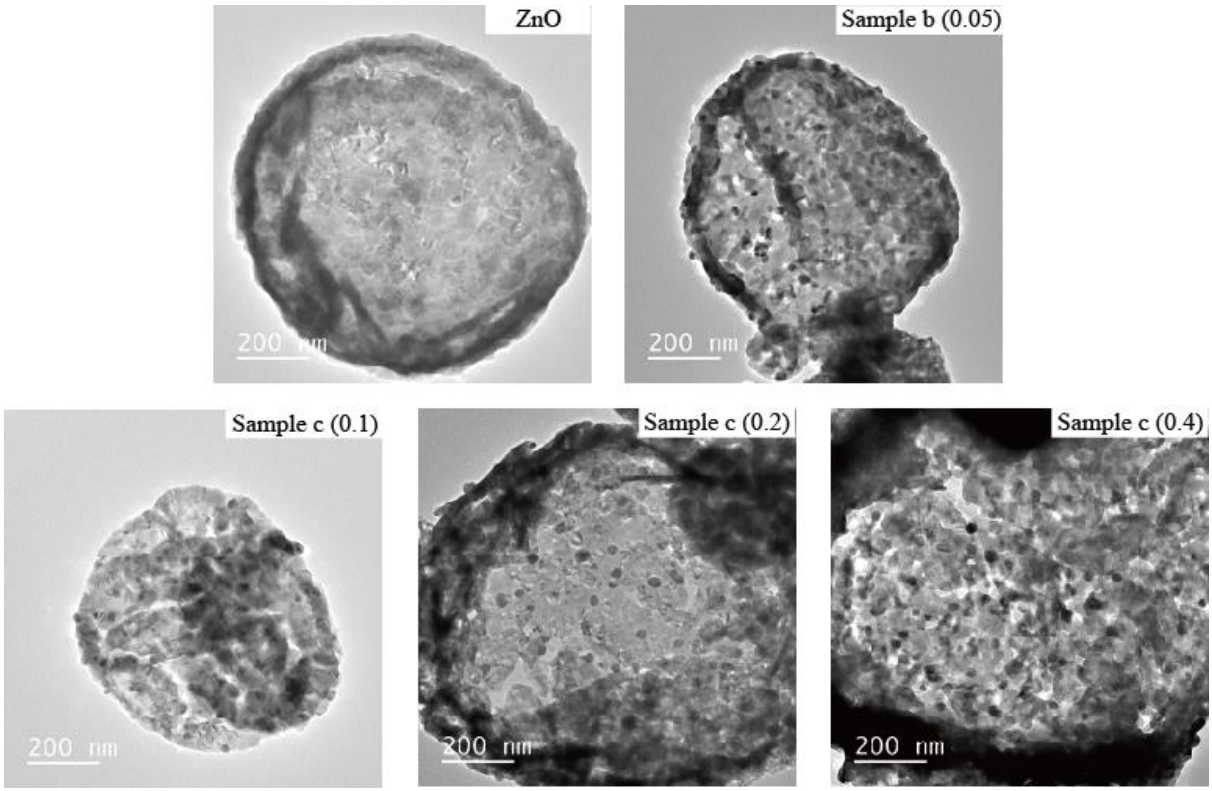

Figure 3-3 TEM images of samples a-e obtained by USP synthesis.

Figure 3-4 shows the STEM images of sample d and the elemental mapping images of Zn, O and Ag. The mapping image of the Ag element shown that the dark spots on ZnO correspond to Ag. It is clearly evident that both Zn and Ag elements were distributed uniformly at the surface, which will be beneficial for charge carrier transform between ZnO and Ag. That is, Ag nanoparticles in the metal form are dispersed throughout the ZnO particles, which suggests that excited electrons can carrier transform to Ag nanoparticles.

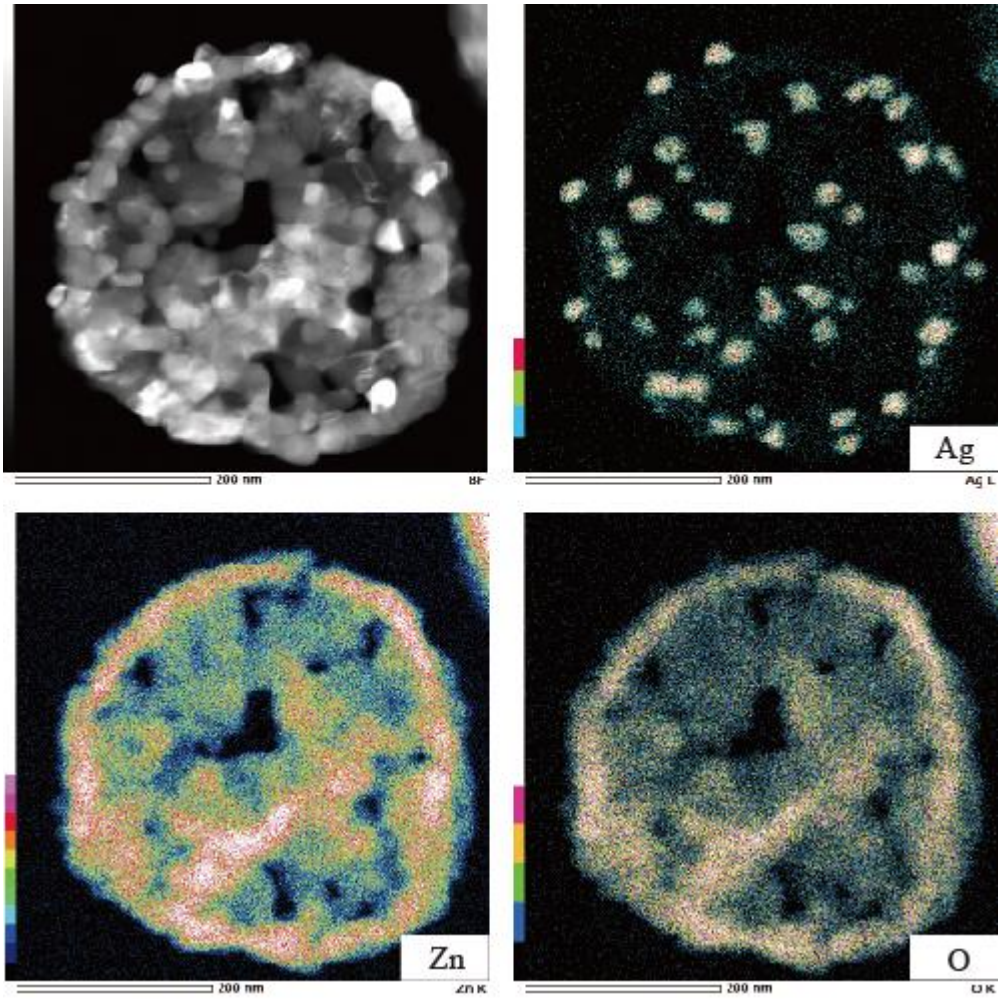

Figure 3-4 STEM image of sample d particle and the corresponding EDX mapping images of the Ag, Zn, and O, respectively.

3.3.2. Photocatalytic activity

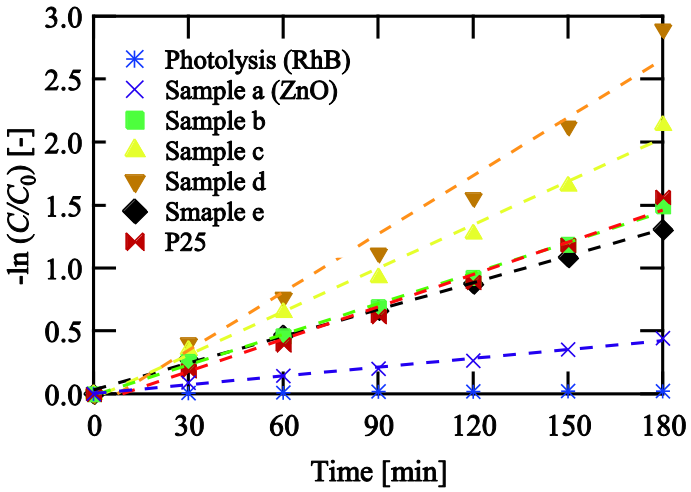

Figure 3-5 Semilogarithmic plot of changes in RhB concentration by UV light irradiation time at ZnO (Sample a), samples b-e, and P25; initial concentration of RhB: 5 mg/L; photocatalyst dose: 5 mg; solution volume: 100 mL.

Figure 3-5 shows a semilogarithmic plot of the changes in the RhB concentration of samples a-e as a function of UV light irradiation time. Each 5 mg of photocatalyst was added to RhB aqueous solution of 5 mg/L, and photocatalysis was performed under UV light irradiation for 180 minutes. P25 was included here as reference sample. Compared to pure ZnO particles, all Ag/ZnO particles have higher photocatalytic efficiency, and as the amount of doped Ag increases, the photocatalytic efficiency tends to increase. Optimal decomposition activity exhibit in sample d with 0.2 mass% Ag doped. However, in the case of sample e, which doped the silver nitrate excessively than the sample d, the photocatalytic efficiency decreased. Interestingly, samples c and d showed better results than commercial titania powder, and our submicron-sized particles showed better results than nano-sized titania.

When decomposing organic dyes using a photocatalyst, the surface-to-volume ratio of the photocatalyst is very important, and the separation of electrons and holes can be greatly improved by reducing the ZnO to nano size. However, it is difficult to retrieve the finely powdered photocatalyst from the mixed solution, which can be limited in commercial applications. In addition, since the photocatalyst may deteriorate in performance and release toxicity over time, retrieval after use of the

photocatalyst is a very important part of water purification applications [16-17]. Our Ag/ZnO particles (such as samples c-d) produced by the USP method not only showed better activity than P25 but also had a relatively large particle size, so they could be easily removed from the mixed solution by gravitational sedimentation.

Table 3-2 First-order reaction rate constant k and the coefficient of determination R^2 corresponding to the slope of the line.

Samples	Reaction rate constant, k [min^{-1}]	Coefficient of determination, R^2
ZnO (a)	0.00234	0.993
b	0.00810	0.997
c	0.01149	0.993
d	0.01539	0.978
e	0.00709	0.998
P25	0.00855	0.985

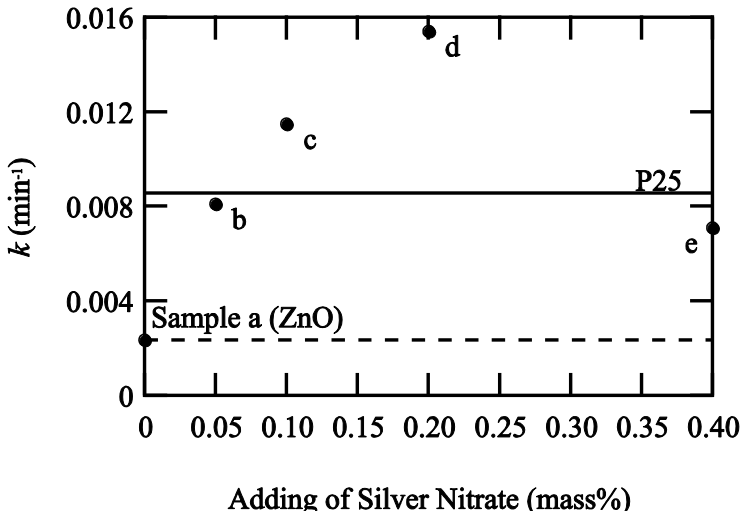

Figure 3-6 First-order reaction rate constant for RhB photolysis using ZnO (Sample a), samples b-e, and P25 under UV light irradiation; initial concentration of RhB: 5 mg/L; photocatalyst dose: 5 mg; solution volume: 100 mL.

Table 3-2 shows the first-order reaction rate constant *k* and the coefficient of determination R^2 corresponding to the slope of the line. And the first-order reaction rate constant k is graphically plotted in Figure 3-6. Compared to pure ZnO particles (sample a), the first order reaction rate constant *k* was about 3 times higher for sample b and about 4.5 times for sample c and about 6 times for sample d, and about 4 times for sample e. Sample d, which exhibited optimal decomposition activity, had a reaction rate constant of about 2 times higher than that of P25. Although more Ag particles were doped in sample e, the photolysis rate constant was lower than that of samples c and d. As a result of the analysis in Figs. 2 and 3, it was confirmed that as the amount of silver nitrate added to the raw material solution increased, the crystallite size of the Ag and the amount of Ag particles in the ZnO particles increased. This result is consistent with our previous experiments with Au doped [25], and it was found that the excessive noble metal doped act as the center of recombination of the excitation electrons. In the other words, when Ag is doped on ZnO particles, Ag receives excited electrons from ZnO particles and contributes to the formation of hydroxyl radicals, but when Ag is excessively doped, excessive excitation electrons are accumulated in Ag, which can promote electron-hole recombination.

This change in photocatalytic activity can be explained by the change in the Fermi level of ZnO and Ag nanoparticles. Figure 3-7 shows the change in Fermi level due to contact between ZnO and Ag particles. As shown in Fig. 3-7(a), the Fermi levels of ZnO and Ag particles before contact differed by -4.26 and -4.99 eV, respectively. When ZnO and Ag particles come into contact, the Fermi level is

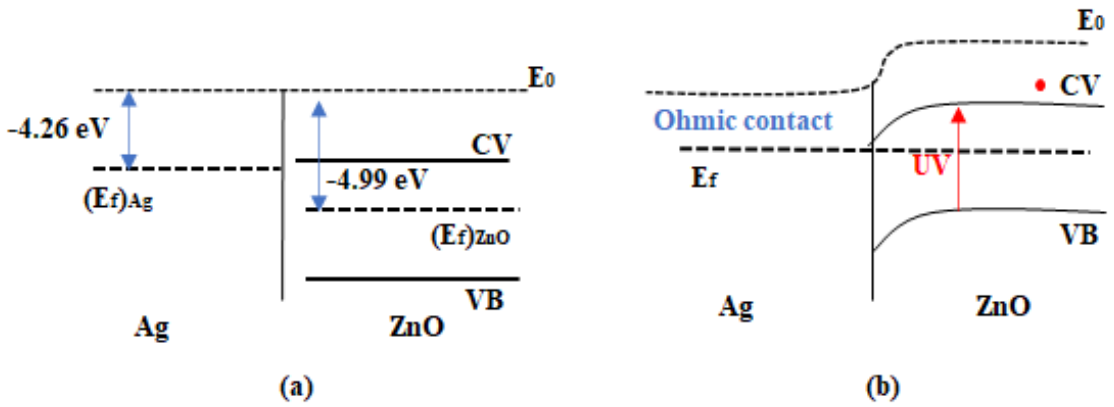

Figure 3-7 (a) Fermi level of ZnO and Ag particles before compounding, (b) Fermi level of ZnO and Ag particles after compounding. E_0:vacuum level; $(E_f)_{Ag}$, $(E_f)_{ZnO}$, E_f: Fermi levels of Ag, ZnO, and Ag/ZnO; CV and VB : conduction band and valence band of ZnO.

reached as shown in Fig. 3-7 (b), and Ohmic contact is formed because the Fermi level of ZnO is relatively lower than the Fermi level of Ag. And since excited electrons can easily move to Ag particles due to Ohmic contact, Ag particles can act as a sink of electrons. And the photolytic activity is increased because the large loading of Ag particles causes more excitation electron transfer to the Ag particles. However, when Ag particles become larger with excessive loading, the Fermi level may decrease due to the quantum size effect and become similar to that of ZnO. Therefore, excessive loading causes the Fermi level of Ag particles to decrease and the movement of excitation electrons can be suppressed. As a result, the recombination of the excited electrons increases and the activity of the photocatalyst decreases.

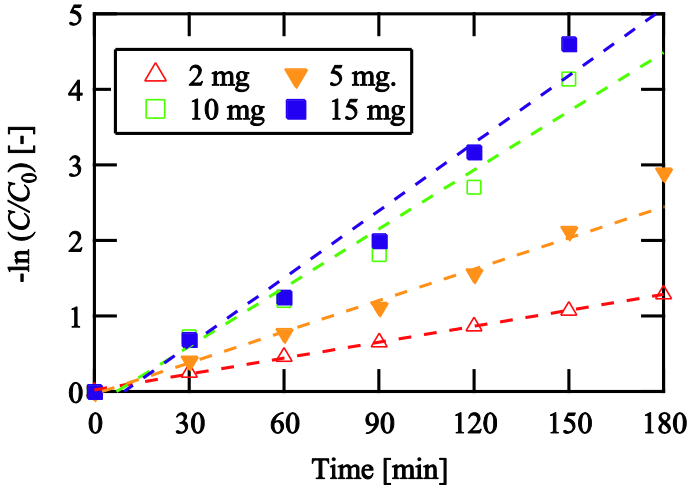

Figure 3-8 Semilogarithmic plot of changes in RhB concentration by UV light irradiation time at different photocatalyst dose of Sample d; initial concentration of RhB: 5mg/L; solution volume: 100mL.

In order to know the optimal dose of sample d, which showed the most efficient photolysis, a photolysis experiment was performed by dispersing 2–15 mg of sample d in an aqueous RhB solution. Figure 3-8 shows the semilogarithmic plot of the changes in the RhB concentration as a function of UV light irradiation time. The first-order reaction rate constant depends on the photocatalyst dose. The first-order reaction rate constant k and the coefficient of determination R^2 are shown in Figures 3-9 and 3-3.

The photocatalytic activity improved as the dose of sample d increased and increased from 2-10 mg in proportion to the amount of sample. However, when 15 mg was dose, the increase in the photolysis rate was insignificant compared to the photolysis rate of 10 mg. It means that an excessive

dose of Ag to particles increases the turbidity of the suspension and affects the photocatalytic activity. That is, the increase in turbidity of the suspension due to excessive dose of the particles may block UV light and hinder the UV light absorption of the photocatalyst [19-20].

Table 3-3 First-order reaction rate constant k and the coefficient of determination R^2 for dose.

Dose [mg]	Reaction rate constant, k [min^{-1}]	Coefficient of determination, R^2
2mg	0.00703	0.999
5mg	0.01376	0.993
10mg	0.02592	0.961
15mg	0.02973	0.965

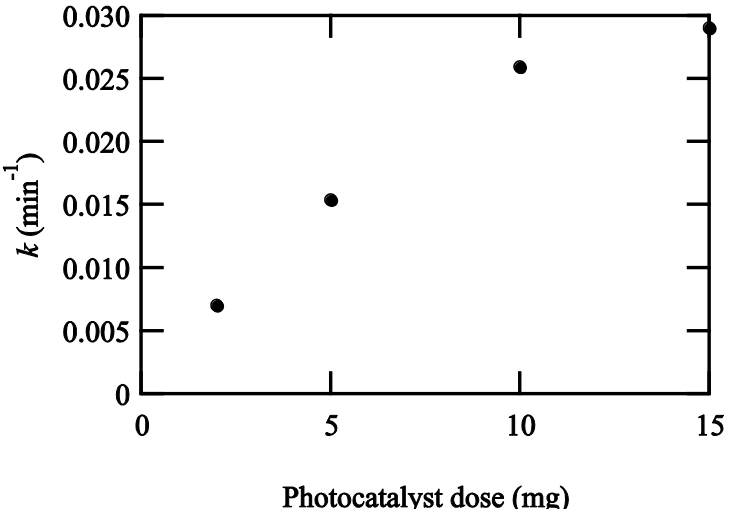

Figure 3-9 First-order reaction rate constant for RhB photolysis using different photocatalyst dose of Sample d under UV light irradiation; initial concentration of RhB: 5mg/L; solution volume: 100mL.

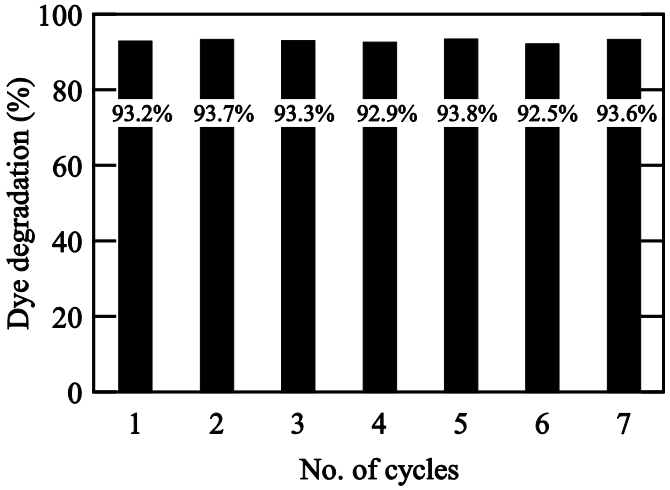

Figure 3-10 Reusability of sample d photocatalyst under UV light irradiation; initial concentration of RhB: 5mg/L; photocatalyst dose: 10mg; solution volume: 100mL; UV light irradiation time: 120min.

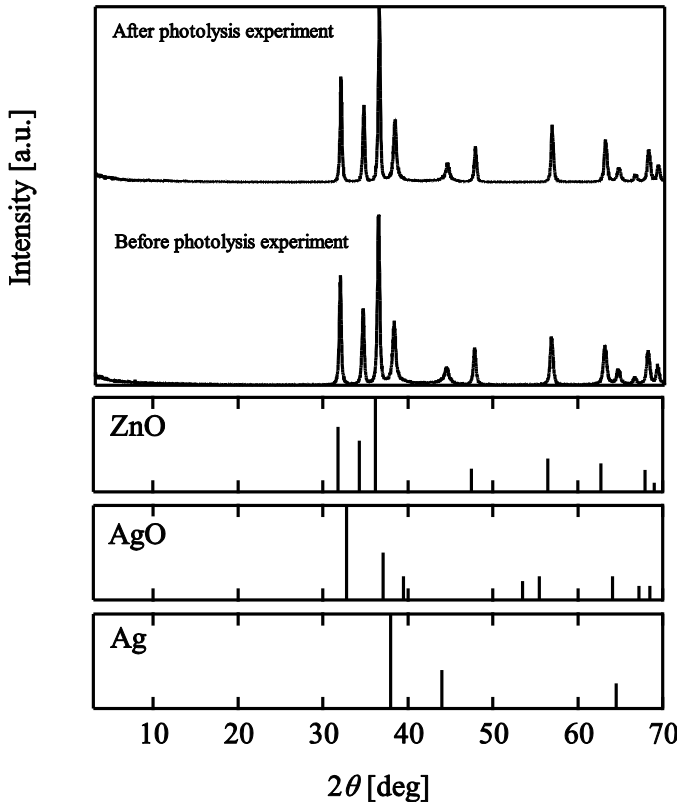

Figure 3-11 XRD peaks before and after the photolysis experiment of sample e.

In order to confirm the possibility of reusability of our particles, after the photolysis experiment, the particles were separated from the mixed solution by gravity sedimentation. And a photolysis experiment was performed by adding a new RhB solution, and the process was repeated. Sample d was added with 10 mg identified as the optimal dose in Figure 3-8. In order to observe the deterioration of the photocatalyst, a photolysis experiment was performed for 120 minutes which the dye degradation did not reach 100%. Figure 3-10 shows the reusability of photocatalyst sample d for RhB dye degradation analyzed over 7 cycles under UV irradiation. In the first cycle without reuse, it showed 93.2% of dye degradation. After that, compared to the photolysis efficiency of the first cycle, there was no significant change with an error of ± 1% for 7 cycles, suggesting that the catalyst has excellent persistence and stability.

Figure 3-11 shows the XRD peaks before and after the photolysis experiment, which can further explain the stability of the photocatalyst. There was no significant change in the XRD peaks before and after the photolysis experiment of the particles, and no Ag oxidation was observed. In other words, the Ag/ZnO particles generated in this study are very stable against oxidation and have resistance to particle deterioration because Ag particles are trapped in the ZnO particles.

3.4. Conclusion

It was possible to generate ZnO and Ag/ZnO particles using the USP method under various conditions. All particles were spherical and 0.5 to 1.0 μm in size, and there was no change in morphology by Ag support. The crystal peaks of ZnO were observed in all of the generated particles, and the Ag crystal peaks were observed in all Ag/ZnO particles. The crystal peak of Ag crystal peak was higher as the amount of silver nitrate added to the raw material solution increased, and the crystallite size of Ag also increased. In the TEM image, dark spots dispersed in Ag/ZnO particles were identified, and the size of the dark spots was different depending on the concentration of added silver nitrate. It was confirmed from EDX mapping and STEM images that this dark spot corresponds to the Ag particle nano dispersed throughout the ZnO particles.

The photocatalytic activity of the generated particles was investigated by photolysis of the RhB aqueous solution under UV irradiation. All Ag/ZnO particles showed better photocatalytic activity than ZnO particles. Particularly, the particles with 0.2 mass% silver nitrate supported on ZnO particles showed 2 times better photolysis activity than P25. As the dope amount increased, the photolysis rate constant increased, but it tended to decrease above a specific concentration. This is because excessive Ag dope accumulates excessive exciton electrons, attracts holes, and promotes electron-hole recombination due to the large contact surface with ZnO particles.

In order to investigate the optimal dose required for photolysis, photolysis experiments were performed at various doses. The photocatalytic activity increased proportionally as the dose increased from 2 mg to 10 mg, but no significant change was observed above 10 mg. This is because the ultraviolet rays, which are important for electronic excitation, have been blocked by the cloudy suspension. It also confirmed the reusability of the particles for commercial applications. It was observed that the generated particles not only can be recovered by gravity precipitation after the photolysis experiment, but also have a slow deterioration rate. In this chapter, the USP method was used to easily generate submicron complex particles and confirmed the possibility of purification and reuse of organic pollutants.

3.5. Reference

1. P. Pawinrat, O. Mekasuwandumrong, J. Panpranot, Synthesis of Au–ZnO and Pt–ZnO

nanocomposites by one-step flame spray pyrolysis and its application for photocatalytic degradation of dyes, Catalysis Communications, 10 (2009) 1380–1385.

2. H.B. Zeng, P.S. Liu, W.P. Cai, S.K. Yang, X.X. Xu, Controllable Pt/ZnO porous nanocages with improved photocatalytic activity, The Journal of Physical Chemistry C, 112 (2008) 19620–19624.
3. Y.G. Chang, J. Xu, Y.Y. Zhang, S. Ma, L.H. Xin, L. Zhu, C.T. Xu, Optical Properties and Photocatalytic Performances of Pd Modified ZnO Samples, The Journal of Physical Chemistry C, 113 (2009) 18761–18767.
4. M.J. Height, S.E. Pratsinis, O. Mekasuwandumrong, P. Praserthdam, Ag-ZnO catalysts for UV-photodegradation of methylene blue, Applied Catalysis B: Environmental, 63 (2006) 305–312.
5. Y.F. Wang, J.H. Yao, G. Jia, H. Lei, Optical Prosperities of Ag–ZnO Composition Nanofilm Synthesized by Chemical Bath Deposition, Acta Physica Polonica A, 119 (2011) 451–454.
6. W. Xie, Y.Z. Li, W. Sun, J.C. Huang, H. Xie, X.J. Zhao, Surface modification of ZnO with Ag improves its photocatalytic efficiency and photostability. Journal of Photochemistry and Photobiology A: Chemistry, 216 (2010), 149–155.
7. Y.C. Lu, Y.H. Lin, D.J. Wang, T.F. Xie, T.F. Jiang, Surface charge transfer properties of high-performance Ag-decorated ZnO photocatalysts, Journal of Physics D: Applied Physics, 44 (2011) 1-7.
8. Y.H. Zheng, L.R. Zheng, Y.Y. Zhan, X.Y. Lin, Q. Zheng, K.M. Wei, Ag/ZnO heterostructure nanocrystals: synthesis, characterization, and photocatalysis, Inorganic Chemistry, 46 (2007), 6980–6986.
9. B. Subash, B. Krishnakumar, M. Swaminathan, M. Shanthi, Synthesis and characterization of cerium–silver co-doped zinc oxide as a novel sunlight-driven photocatalyst for effective degradation of Reactive Red 120 dye. Materials Science in Semiconductor Processing, 16 (2013), 1070–1078.
10. W.W. Lu, S.Y. Gao, J.J. Wang, One-Pot Synthesis of Ag/ZnO Self-Assembled 3D Hollow Microspheres with Enhanced Photocatalytic Performance, The Journal of Physical Chemistry C, 112 (2008) 16792–16800.
11. A. Senthilraja, B. Subash, B. Krishnakumar, D. Rajamanickam, Synthesis, characterization and catalytic activity of co-doped Ag–Au–ZnO for MB dye degradation under UV-A light, Materials Science in Semiconductor Processing, 22 (2014) 83-91.

12. T.K. Pathak, R.E. Kroon, H.C. Swart, Photocatalytic and biological applications of Ag and Au doped ZnO nanomaterial synthesized by combustion, Vacuum, 157 (2018) 508-513.

13. H.S.Zhai, X.L. Liu, Z. Wang, Y.Y. Liu, Z.K. Zheng, X.Y. Qin, X.Y. Zhang, P. Wang, B.B. Huang, ZnO nanorod decorated by Au-Ag alloy with greatly increased activity for photocatalytic ethylene oxidation, Chinese Journal of Catalysis, 41 (2020) 1613-1621.

14. H. Li, E.T. Liu, F.Y.F. Chan, Z. Lu, R. Chen, Fabrication of ordered flower-like ZnO nanostructures by a microwave and ultrasonic combined technique and their enhanced photocatalytic activity, Materials Letters, 65 (2011) 3440-3443.

15. N. Güy, M. Özacar, The influence of noble metals on photocatalytic activity of ZnO for Congo red degradation, International Journal of Hydrogen Energy, 41 (2016) 20100-20112.

16. X.F. Bian, K.Q. Hong, X. Ge, R. Song, L.Q. Liu, M.X. Xu, Functional Hierarchical Nanocomposites Based on ZnO Nanowire and Magnetic Nanoparticle as Highly Active Recyclable Photocatalysts, The Journal of Physical Chemistry C, 119 (2015) 1700–1705.

17. X. Zhang, S. Xu, G.R Han, Fabrication and photocatalytic activity of TiO_2 nanofiber membrane, Materials Letters, 63 (2009) 1761-1763.

18. A.B.D. Nandiyanto, K. Okuyama, Progress in developing spray-drying methods for the production of controlled morphology particles: From the nanometer to submicrometer size ranges, Advanced Powder Technology, 22 (2011) 1-9.

19. C.S. Lu, Y.T. Wu, F. Mai, W.S. Chung, C.W. Wu, Degradation efficiencies and mechanisms of the ZnO-mediated photocatalytic degradation of Basic Blue 11 under visible light irradiation, Journal of Molecular Catalysis A, 310 (2009) 159-165.

20. B. Neppolian, H. C. Choi, S. Sakthivel, B. Arabindoo, V. Murugesan, Solar light induced and TiO_2 assisted degradation of textile dye reactive blue 4, Chemosphere, 46 (2002) 1173-1181.

Chapter 4 ZnO/Fe_3O_4 and $ZnO/Fe_3O_4/Ag$ composite particle generation process

4.1. Introduction

An issue in the application of ZnO photocatalyst to organic dye treatment is that it is difficult to recover fine photocatalyst particles from photolysis treated wastewater. Methods such as filtration or centrifugation for particle recovery can cause destruction and loss of particles, resulting in high operating costs and secondary pollution [1]. Therefore, there is a need for a study that can simply recover the particles. In Chapters 2-3, submicron-level ZnO particles carrying Au and Ag were generated using the spray pyrolysis method, and recovery and reusability were confirmed by gravity sedimentation. However, the combination of photocatalyst and magnetic particles may be a more reliable solution. By combining the photocatalyst and magnetic particles, not only can the particles be easily recovered through magnetic separation processes, but they can also be recycled [2-4].

Among the many types of iron oxide, magnetite (Fe_3O_4), maghemite (γ-Fe_2O_3), and hematite (α-Fe_2O_3) are the most common in nature [5]. Since hematite (α-Fe_2O_3) is stable and exists most often in rocks and soils, there are many applications [6]. And due to its semiconductor properties, it can also be used in photocatalytic applications [7]. Therefore, hematite (α-Fe_2O_3) is attracting attention in the fields of advanced magnetic materials, catalysts, colored pigments, high-density magnetic recording media, and medical diagnosis because of its stability, low cost, and bandgap (2.1eV) [8- 13]. However, since the magnetic strength is in the order of Fe_3O_4 > γ-Fe_2O_3 > α-Fe_2O_3 [14-15], recovery of the photocatalyst through hematite complexation may be very difficult. In particular, magnetite (Fe_3O_4) has attracted more attention over the past 10 years due to its strong superparamagnetic properties, low toxicity, and easy production method [16]. Magnetite forms a central cubic (FCC) lattice and has a spinel structure with the same number of Fe^{2+} and Fe^{3+}. However, due to the disadvantage that magnetite is easily oxidized and agglomerated under acidic conditions, the application of organic dyes may be limited. Therefore, the combination of ZnO photocatalyst and magnetite can be a good way to overcome the shortcomings.

For the synthesis of ZnO/Fe_3O_4 composites, precipitation [17], co-precipitation [18], deposition [19], wet milling [20], solvothermal [21], and wet chemical route [22] are used. Since co-precipitation is the cheapest and easiest method, it is well suited for commercial applications. Therefore, in this chapter,

the synthesis conditions of ZnO/Fe_3O_4 and ZnO/Fe_3O_4/Ag composite materials were investigated using the gas-phase ultrasonic spray pyrolysis method and the liquid phase co-precipitation method, and the characteristics of the generated particles were confirmed.

4.2. Experimental setup and Method

4.2.1. Materials

Zinc nitrate hexahydrate ($Zn(NO_3)_2\,6H_2O$, ≥99.0%), and Silver nitrate ($AgNO_3$, ≥99.8%), Iron (II) sulfate heptahydrate ($FeSO_4\,7H_2O$, ≥99.0%), Iron (III) chloride hexahydrate ($FeCl_3\,6H_2O$, ≥99.0%), and Trisodium citrate ($C_6H_5Na_3O_7$) were purchased from FUJIFILM Wako Pure Chemical Industries. And Rhodamine-B ($C_{28}H_{31}ClN_2O_3$, >95.0%) was purchased from Tokyo Chemical Industries. Sodium hydroxide (NaOH, >95.0%) was purchased from Kanto Chemical Industries. Titanium dioxide nanopowder as standard photocatalyst (Evonik AEROXIDE® P25, formerly Degussa) was purchased from Sigma–Aldrich. All reagents were used as received without further purification. Distilled water was used in all experiments.

4.2.2. Generation of ZnO/Fe_3O_4 particles using USP method

The generation of ZnO/Fe_3O_4 composite particles was attempted using the USP method described in Chapter 2. Therefore, the device and its operation method are briefly described here. The USP apparatus was composed of a nebulizer with a resonance frequency of 1.7 MHz, a quartz glass reaction tube, four electric furnaces with a temperature controller of ±1 °C, a diffusion dryer, and an electrostatic precipitator. The Zinc nitrate hexahydrate was dissolved in 100 mL of distilled water with concentration maintained at 10 mass%. And Iron (III) chloride hexahydrate concentration 2.5 mass% was added into the precursor solution. The rate introduced into the nebulizer of precursor solution was 15mL/h. The generated droplets by nebulizer were introduced into the quartz glass reaction tube using a nitrogen or air flow at a rate of 1.0 or 0.65 SLM. And flow rate of sheath gas to prevent gravity sedimentation was fixed at a rate of 0.5 or 0.15 SLM. Four electric furnaces for heating the quartz reaction tube were used, two 80 mm preheating furnaces from the bottom were set to 40 °C and 70 °C, respectively, and two 290 nm heating furnaces were set to 1000 °C. The composite particles synthesized by droplet decomposition were dried with a diffusion dryer. After that, the composite particles were collected in the electrostatic precipitator. The experimental parameters for

the synthesis of ZnO/Fe_3O_4 composite particles are listed in Table 4-1.

Table 4-1 Experimental parameters of the ZnO/Fe_3O_4 composite particles by USP method.

Sample	Concentration		Rate of flow (SLM)	
	$Zn(NO_3)_2$	$FeCl_3$	Carrier gas	Sheath gas
a	10 (mass%)	2.5 (mass%)	1.00 (N_2)	0.50 (N_2)
b			0.65 (N_2)	0.15 (N_2)
c			1.00 (N_2)	0.50 (Air)
d			0.65 (Air)	0.15 (Air)
e	Zn: 1 (Molar ratio)	Fe: 2 (Molar ratio)	0.65 (Air)	0.15 (Air)

4.2.3. Generation of ZnO/Fe_3O_4 composite particles using USP and co-precipitation method

Many studies have been reported on coating ZnO on Fe_3O_4 using a co-precipitation method. In particular, sodium citrate is used as a surface modification material for the complexation of Fe_3O_4 and ZnO [18,23-24]. For example, Hong *et al*. generated Fe_3O_4 by co-precipitation method and synthesized ZnO/Fe_3O_4 nanoparticles by coating ZnO after surface modification of Fe_3O_4 with sodium citrate [18]. However, ZnO generated by the co-precipitation method requires post-processing of calcination and sintering, which has the disadvantage of causing particle agglomeration. Therefore, in this study, Fe_3O_4 was generated by the co-precipitation method, the surface was modified with sodium citrate, and the ZnO produced by the USP method was attempted to form a complex.

Figure 4-1 shows the procedure of formation of Fe_3O_4 by co-precipitation method. The Fe_3O_4 particles were synthesized by the co-precipitation of Fe^{+2} and Fe^{+3} ions with molar ratio 1:2 in the presence of NaOH as a precipitate agent according to the following chemical reaction:

$$FeSO_4+2FeCl_3+8NaOH \rightarrow Fe_3O_4 + Na_2SO_4 + 6NaCl \qquad (4\text{-}1)$$

$FeSO_4 \cdot 7H_2O$ and $FeCl_3 \cdot 6H_2O$ were dissolved in distilled water, and heated and stirred at 80°C. Thereafter, the NaOH solution was added dropwise while stirring, and the resulting particles were washed three times with distilled water. The particles were dried in a dryer, and the obtained powder was pulverized using a mortar.

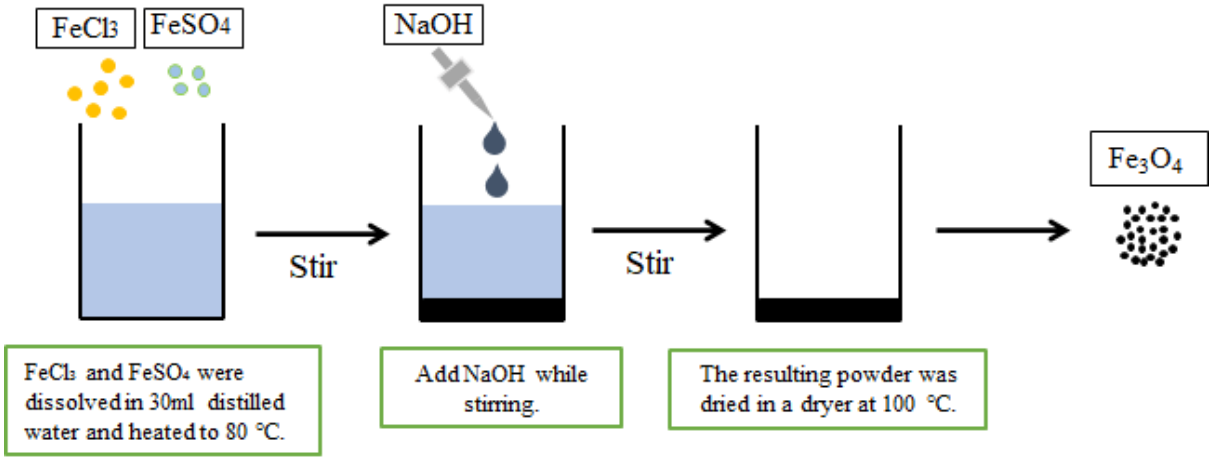

Figure 4-1 Procedure of formation of Fe_3O_4 by co-precipitation method.

Figure 4-2 shows the procedure of formation of ZnO/Fe_3O_4 composite particles. First, 0.4 g of Fe_3O_4 particles obtained by the co-precipitation method were added to 20 g of a 0.5 M aqueous solution of trisodium citrate and stirred for 3 hours. Then, it washed twice with distilled water, and adjusted by adding distilled water. In addition, 0.4 g, 0.8 g, and 1.2 g of ZnO particles produced by the spray pyrolysis method were added, respectively, so that the mass ratio of ZnO and Fe_3O_4 was 1:1, 2:1, 4:1, and stirred for 24 hours. The obtained particles were washed three times with distilled water, and dried with a dryer at 100°C. The obtained composite powder was pulverized using a mortar, and finally ZnO/Fe_3O_4 particles were obtained.

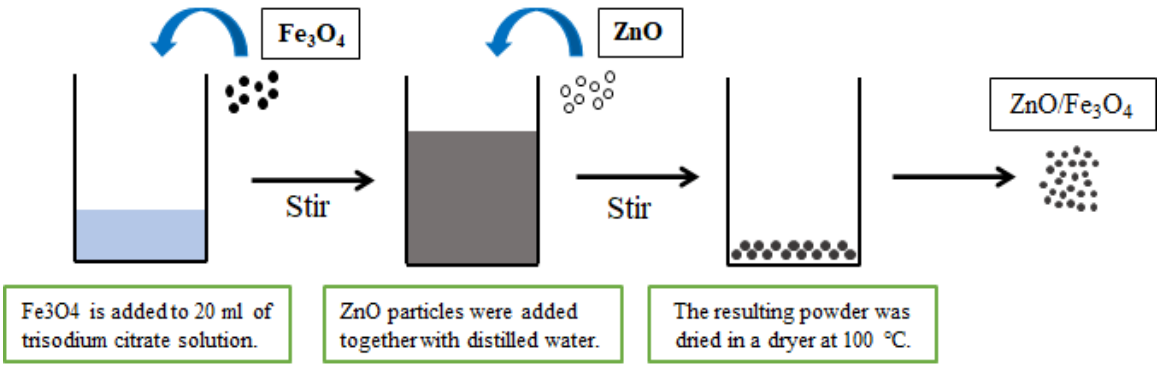

Figure 4-2 Procedure of formation of ZnO/Fe_3O_4 composite particles.

4.2.4. Generation of ZnO/Fe_3O_4 and ZnO/Fe_3O_4/Ag composite particles using co-precipitation method

Synthesis of ZnO/Fe_3O_4 and ZnO/Fe_3O_4/Ag was attempted using the co-precipitation method. The Fe_3O_4 particles were generated by the method described previously and coated with ZnO and Ag using the co-precipitation method. Figure 4-3 shows the procedure of formation of ZnO/Fe_3O_4 and ZnO/Fe_3O_4/Ag composite particles. Zinc nitrate was dissolved in 300 ml of distilled water and heated to 90 °C. Fe_3O_4 particles generated by the co-precipitation method were added, and NaOH solution was added dropwise to PH8.5 while stirring. Here, the mass ratio of ZnO and Fe_3O_4 is set to be 2:1. The chemical reaction formula for ZnO is as follows:

$$Zn(NO_3)_2 + 2NaOH \rightarrow Zn(OH)_2 \downarrow + 2NaNO_3 \quad (4\text{-}2)$$

$$Zn(OH)_2 \rightarrow ZnO + H_2O \quad (4\text{-}3)$$

Silver nitrate and NaOH were added to support Ag. Silver nitrate was added 0.05, 0.1, 0.2, and 0.4 mass% compared to zinc oxide, and the reaction formula is as follows:

$$2AgNO_3 + 2NaOH \rightarrow Ag_2O \downarrow + H_2O + 2NaNO_3 \quad (4\text{-}4)$$

$$2Ag_2O \rightarrow 4Ag + O_2 \quad (4\text{-}5)$$

Finally, the product was dried and calcined at 250 °C after washing with distilled water, and the resulting product was pulverized with a mortar to obtain the target powder. The experimental parameters of the ZnO/Fe_3O_4 and $ZnO/Fe_3O_4/Ag$ composite particles are listed in Table 4-2.

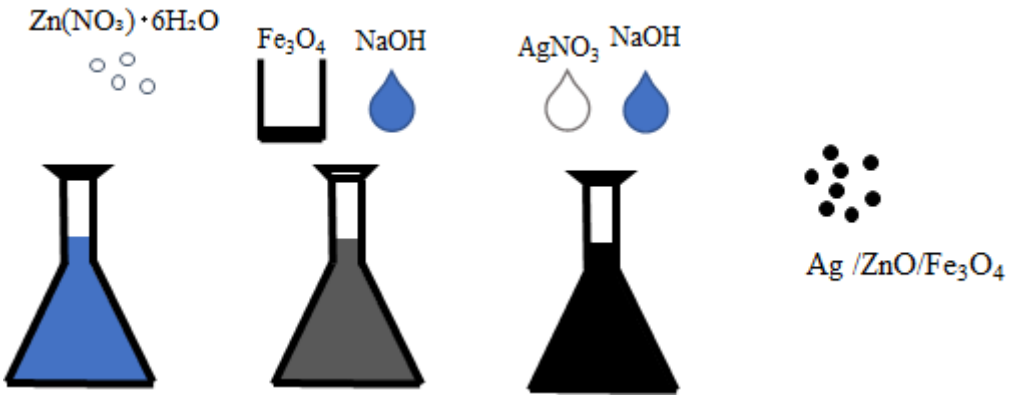

Figure 4-3 Procedure of formation of ZnO/Fe_3O_4 and $ZnO/Fe_3O_4/Ag$ composite particles.

Table 4-2 Experimental parameters of the ZnO/Fe_3O_4 and $ZnO/Fe_3O_4/Ag$ composite particles by co-precipitation method.

Sample	Mass ratio [g] ($ZnO:Fe_3O_4$)	$AgNO_3$ [mass%]
A	2:1	-
B		0.05
C		0.1
D		0.2
E		0.4

4.3. Experimental Results and Discussion

4.3.1. Characteristics of ZnO/Fe_3O_4 composite particles generated using USP method

Particles generated using the USP method under different conditions were analyzed using XRD, and the results are shown in Figure 4-4. In sample a generated under nitrogen flow conditions, peaks of the target products, ZnO and Fe_3O_4, were not observed. Sample b was generated by reducing the amount of nitrogen introduced for sufficient pyrolysis. Although the amount of nitrogen introduced was reduced to increase the residence time of the droplets in the reaction tube, the target product could not be obtained. However, compared to sample a, the peak of Fe was large in sample b. Therefore, samples c and d were generated under oxygen flow for sufficient oxidation. Although sufficient reaction time was given under oxygen flow, the target product was not obtained in samples c and d. In addition, in the sample e generated with a Zn:Fe molar ratio of 1:2, only the peak of $ZnFe_2O_4$ was observed.

Certainly, the generation of iron oxide (Fe_3O_4, γ-Fe_2O_3, α-Fe_2O_3) [25-27] or ZnO single unit by spray pyrolysis has been reported. However, it was confirmed that the generation of the ZnO/Fe_3O_4 composite using the spray pyrolysis method was difficult. In a similar way, Nunome *et al*. produced n- and p-type $ZnFe_2O_4$ and evaluated their properties [28]. $ZnFe_2O_4$ is a paramagnetic material and is known to have a band gap of 1.9 eV [29]. However, its low magnetism and bandgap are not suitable for organic matter treatment. The generation of $ZnFe_2O_4$ is thought to be related to metal reactivity. Since the metal reactivity of Zn and Fe is similar, it can be precipitated as one crystal during the pyrolysis process. On the contrary, since Au and Ag have a large metal reactivity difference and small reactivity compared to Zn, they can be precipitated as different crystals during the pyrolysis process.

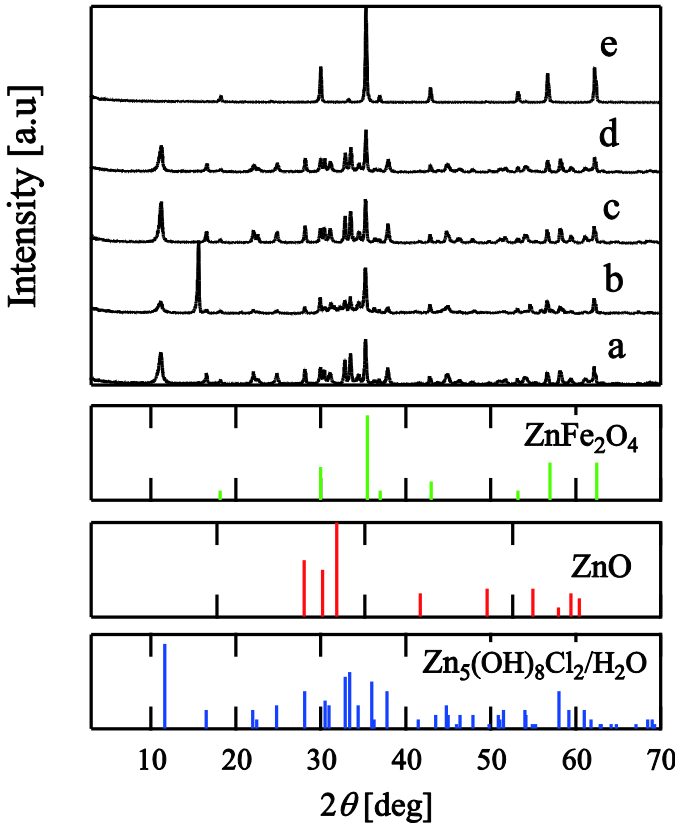

Figure 4-4 XRD result of composite particles generated using USP method.

4.3.2. Characteristics of ZnO/Fe_3O_4 composite particles generated using USP and co-precipitation method

Mass ratio [g] ($ZnO:Fe_3O_4$)	Distributed	No magnet (1 minute later)	Magnet (1 minute later)
1:1			
2:1			
4:1			

Figure 4-5 Magnetism of ZnO/Fe_3O_4 composite particles generated using USP and co-precipitation method.

The observation result of the presence or absence of magnetism of the generated particles is shown in Figs. 4-5. 2 mg of the generated particles were dispersed in 5 ml of water, and the sedimentation rate of the generated particles was observed with a magnet. In any condition, there was a difference in the sedimentation rate of the generated particles depending on the presence or absence of a magnet. In addition, the higher the ratio of ZnO, the slower the particle sedimentation rate. Therefore, the case of the mass ratio ($ZnO:Fe_3O_4$) 1:1 is considered to have the greatest magnetism.

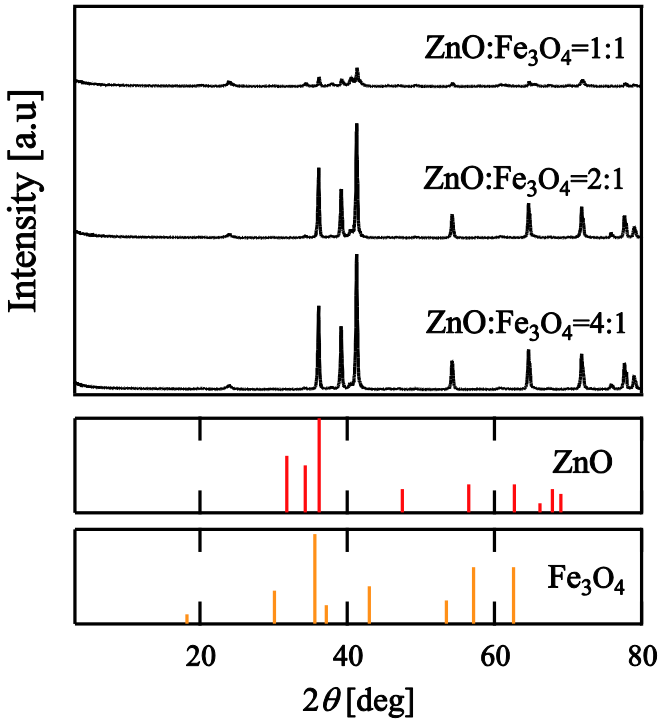

Figure 4-6 XRD result of ZnO/Fe_3O_4 composite particles generated using USP and co-precipitation method.

Figure 4-6 shows the XRD measurement results of the generated particles. Under any conditions, the peaks of ZnO and Fe_3O_4 were confirmed together. The peak of ZnO increased as the mass ratio of ZnO increased. In addition, a small peak was detected in the vicinity of $2\theta = 22$ °, and neither ZnO nor Fe_3O_4. A similar peak was not detected in the XRD measurement of ZnO produced by spray pyrolysis and Fe_3O_4 produced by co-precipitation method, so it is presumed to be a by-product produced in the surface modification process.

Figure 4-7 shows the SEM images of the generated particles. In all conditions, the ZnO/Fe_3O_4 composite material was confirmed through SEM images. However, large-scale aggregates were formed due to the agglomeration of the particles, and the majority of uncoated ZnO particles were also identified. In particular, the formation of such large-scale aggregates can degrade photolysis properties. In addition, uncoated ZnO particles cannot be recovered after photolysis treatment and may cause secondary contamination. Therefore, it was confirmed that the surface modification using sodium citrate was unsuitable for coating ZnO particles produced with USP.

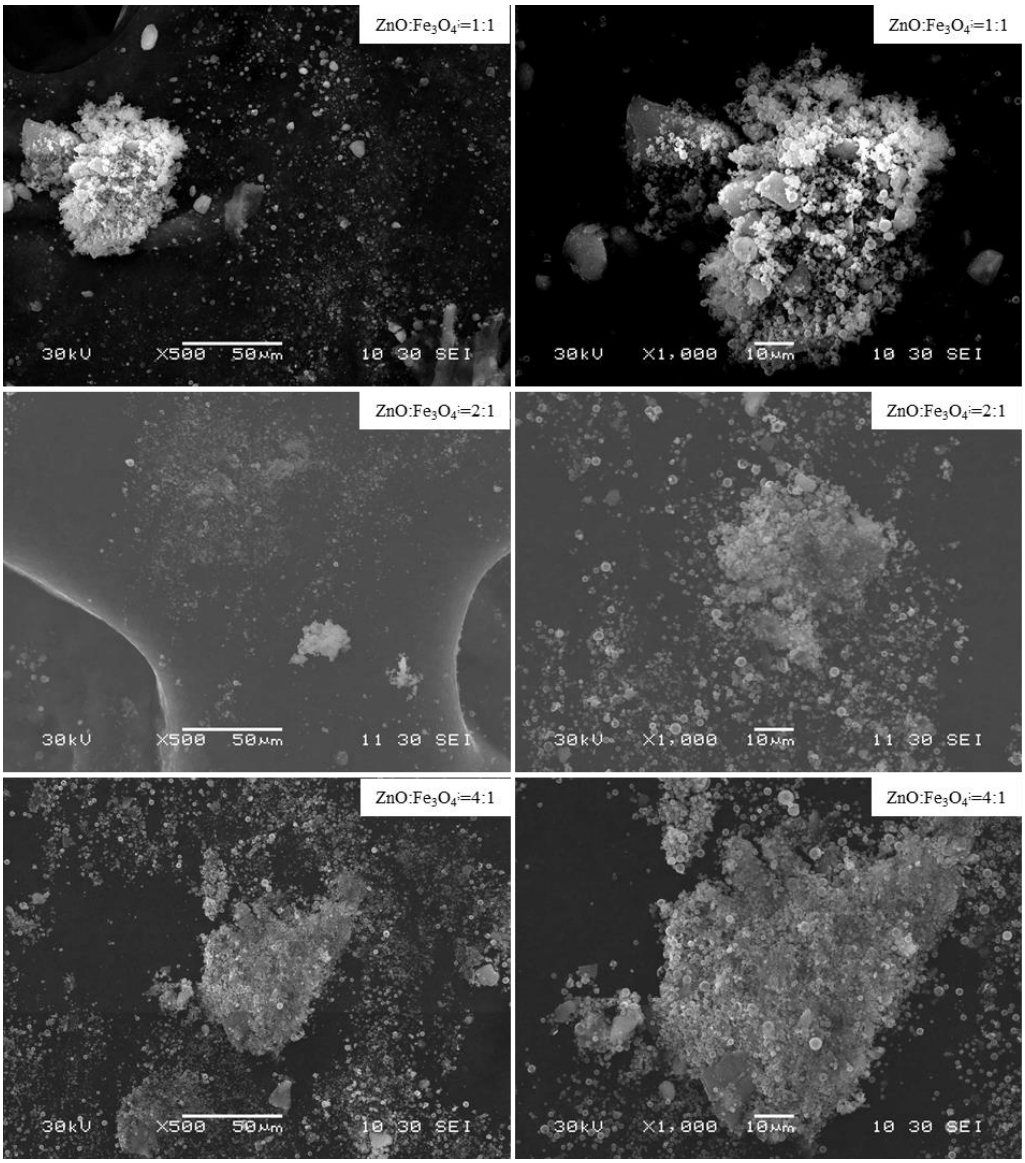

Figure 4-7 SEM images of ZnO/Fe_3O_4 composite particles generated using USP and co-precipitation method.

The photolysis experiment was carried out in the same manner as described in Chapter 2, the concentration of RhB aqueous solution was set to 2 mg/L, and 20 mg of the resulting particles were added. Figure 4-8 shows the photolysis test results of the obtained ZnO/Fe_3O_4 composite material. The decomposition of the RhB solution by ultraviolet rays only decomposed 4% for 300 minutes, whereas the addition of the ZnO/Fe_3O_4 composite material showed remarkable photolysis. In the photolysis experiment for 300 minutes, about 90% in the case of ZnO, about 24% in the mass ratio ZnO: Fe3O4 = 4: 1, about 34% in the mass ratio ZnO: Fe_3O_4 = 2: 1, and about 77% in the mass ratio ZnO: Fe_3O_4 = 1: 1 photolysis was observed. That is, as the mass ratio of ZnO increases, the

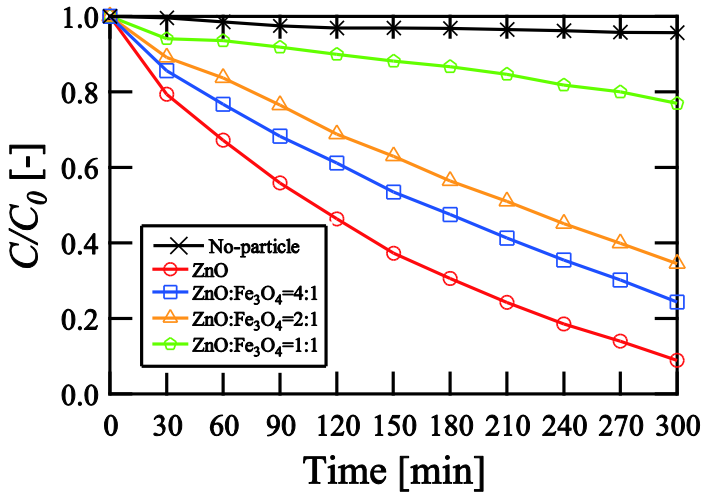

Figure 4-8 Changes in RhB concentration by UV light irradiation time at ZnO/Fe_3O_4 and ZnO generated using USP and co-precipitation method; initial concentration of RhB: 2 mg/L; photocatalyst dose: 20 mg; solution volume: 100 mL.

decomposition rate of RhB also increases. When ZnO and Fe_3O_4 are combined, recovery is possible due to magnetism, but the photocatalytic surface area decreases, resulting in a decrease in photolysis efficiency. Therefore, there is a need for a new synthetic method capable of showing high photocatalytic activity even after complexation.

4.3.3. Characteristics of ZnO/Fe_3O_4 and ZnO/Fe_3O_4/Ag particles generated using co-precipitation method

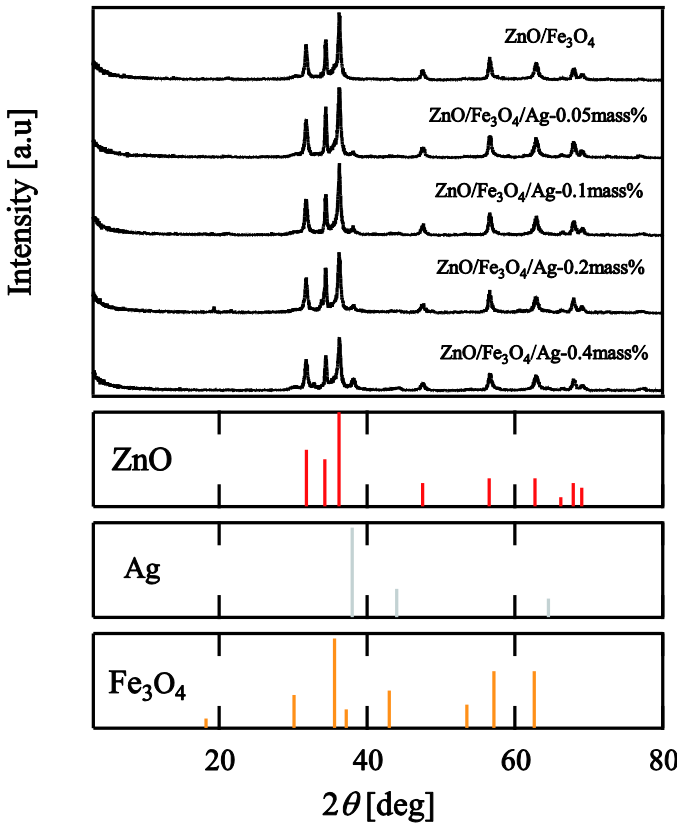

Figure 4-9 XRD result ZnO/Fe_3O_4 and ZnO/Fe_3O_4/Ag particles generated using co-precipitation method.

The XRD pattern of the composite material obtained by this experiment is shown in Figure 4-9. In the XRD pattern, a hexagonal peak of ZnO was observed in all samples. In addition, the crystal peaks of Ag were confirmed at $2\theta = 38$, 44, and 65 °, and it can be seen that ZnO and metallic Ag exist in the obtained composite material. It was confirmed that the Ag peak increased as the ratio of silver nitrate added to the raw material solution increased. However, the peak of Fe_3O_4 overlapped with the peak of ZnO, making it difficult to confirm. Figure 4-10 shows the crystal peaks of Fe_3O_4 and ZnO/Fe_3O_4 produced by the co-precipitation method. Before the complexation, the Fe3O4 crystal peak was observed in the Fe_3O_4 single unit, and it was confirmed that the peaks of ZnO overlap. Therefore, the presence or absence of Fe_3O_4 in the product was investigated by observing the magnetic reaction of the product. 10 mg of the product was dispersed in distilled water and a magnet was placed at the bottom of the sample bottle. And for comparison, a comparison sample without

magnets was prepared. Figure 4-11 shows the appearance of dispersion solution after 1 minute with or without magnets. Certainly, it was observed that the settling speed of the product was high when the magnet was placed on the bottom of the sample bottle. It was confirmed that the resulting composite material contained Fe_3O_4 and had magnetic properties.

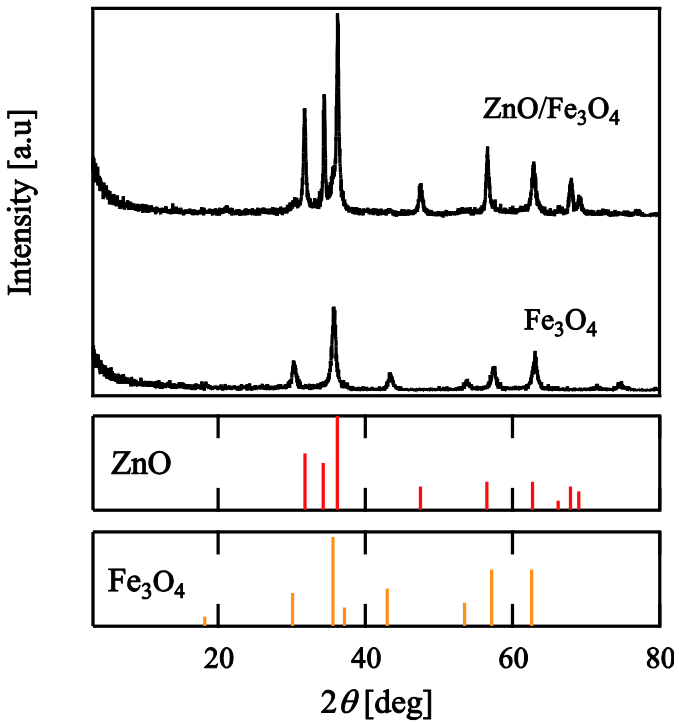

Figure 4-10 Crystal peaks of Fe_3O_4 and ZnO/Fe_3O_4 produced using co-precipitation method.

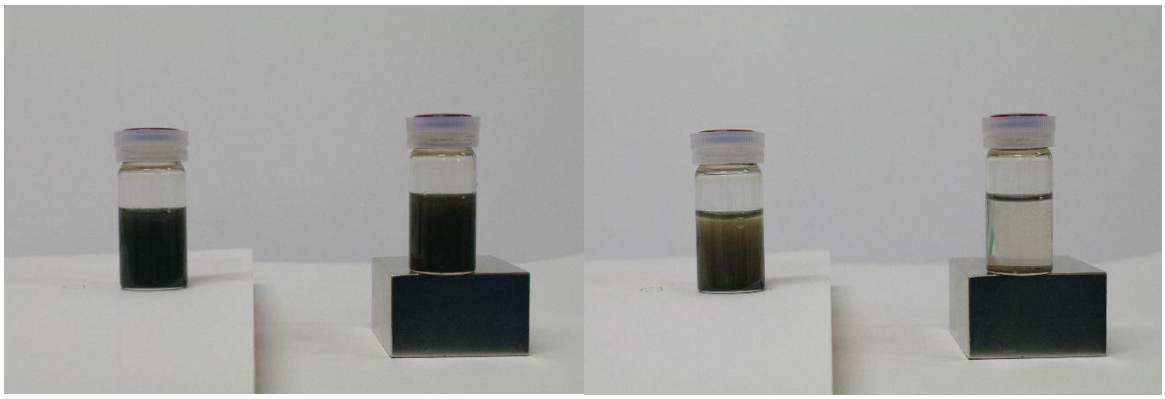

Figure 4-11 Magnetism of ZnO/Fe_3O_4 composite particles generated using co-precipitation method: (Left) before experiment and (Right) 1 minute later

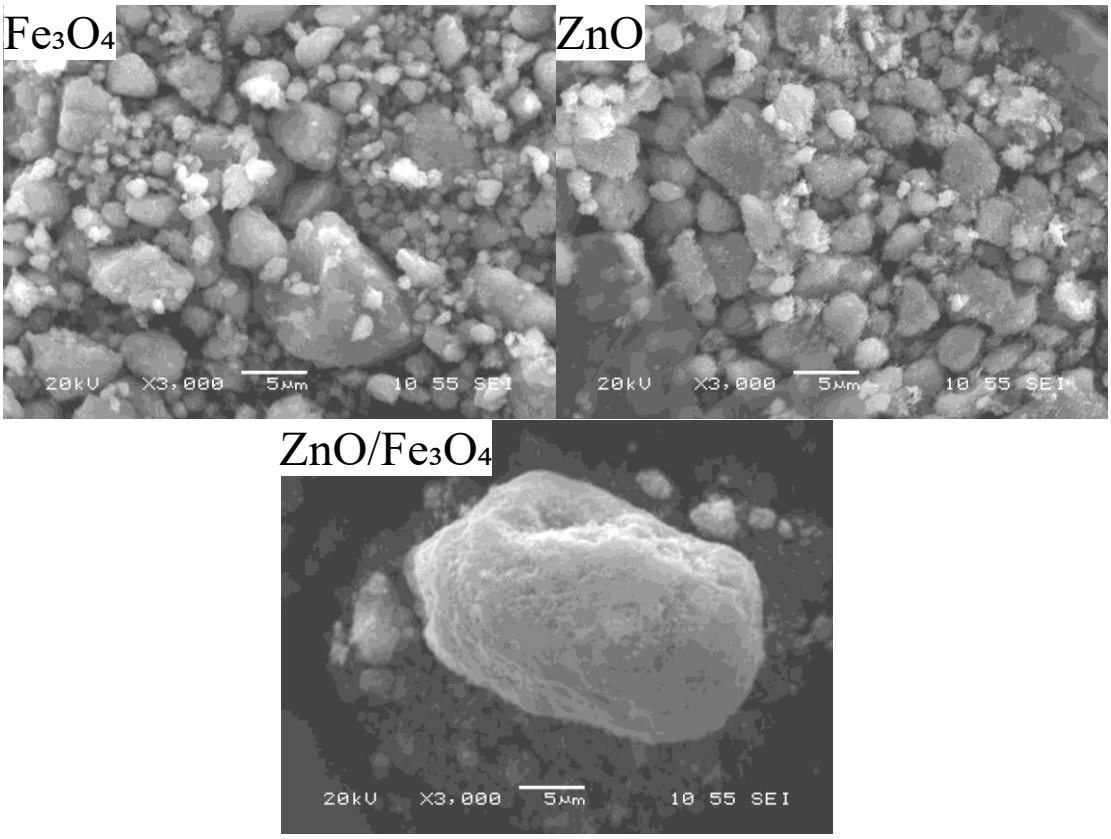

Figure 4-12 SEM images of ZnO, Fe_3O_4, and ZnO/Fe_3O_4 composite particles generated using co-precipitation method.

Figure 4-12 is an SEM picture of the obtained composite. Large and small ZnO and Fe_3O_4 particles of less than 5 μm were identified, and large and small particles of less than 20 μm in the ZnO/Fe_3O_4 composite were identified. Therefore, it is thought that large ZnO/Fe_3O_4 particles are formed by chemical bonding between large and small ZnO and Fe_3O_4 particles. Figure 4-13 shows the backscattered electron images of ZnO/Fe_3O_4 and ZnO/Fe_3O_4/Ag composite particles. The backscattered electron image (b) of the composite obtained by adding silver nitrate is brighter than the image (a) of the composite obtained without adding silver nitrate. Since the reflective electrons of Ag, which have an atomic number larger than that of O, Zn, and Fe, are strong, a bright image appears. Therefore, it was confirmed that Ag in a metallic state was dispersed on the surface of the composite with the measurement result of XRD.

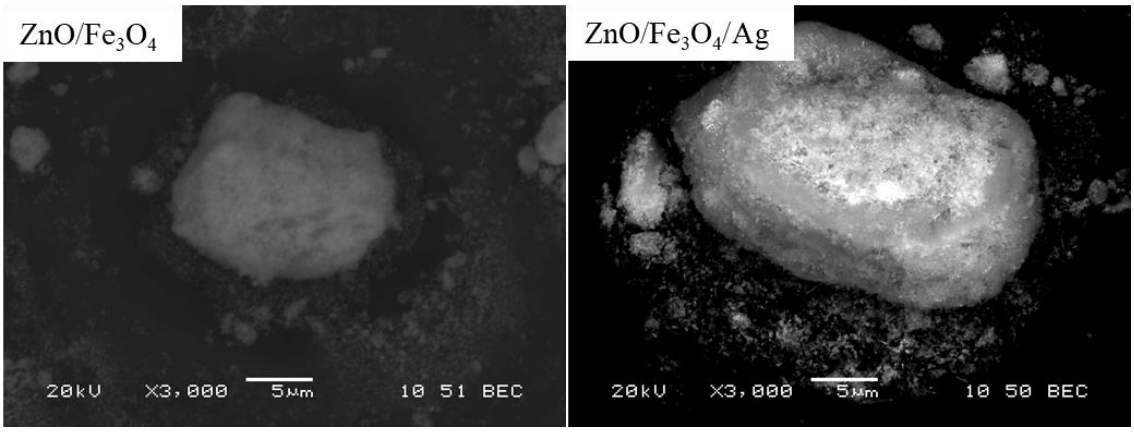

Figure 4-13 Backscattered electron images of (a) ZnO/Fe_3O_4 and (b) ZnO/Fe_3O_4/Ag composite particles generated using co-precipitation method.

The photolysis experiment was carried out in the same manner as described in Chapter 2, the concentration of RhB aqueous solution was set to 5 mg/L, and 15 mg of the resulting particles were added. Figure 4-14 shows the changes in the RhB concentration of obtained composite as UV light irradiation time. As a result of photolysis, it was confirmed that the dye was decomposed by about 21% for ZnO and about 44% for the ZnO/Fe_3O_4 composite material. In addition, the photodecomposition rate of the Ag-supported ZnO/Fe_3O_4/Ag composite was increased compared to that of the ZnO/Fe_3O_4 particles. All ZnO/Fe_3O_4/Ag composite particles show higher photocatalytic

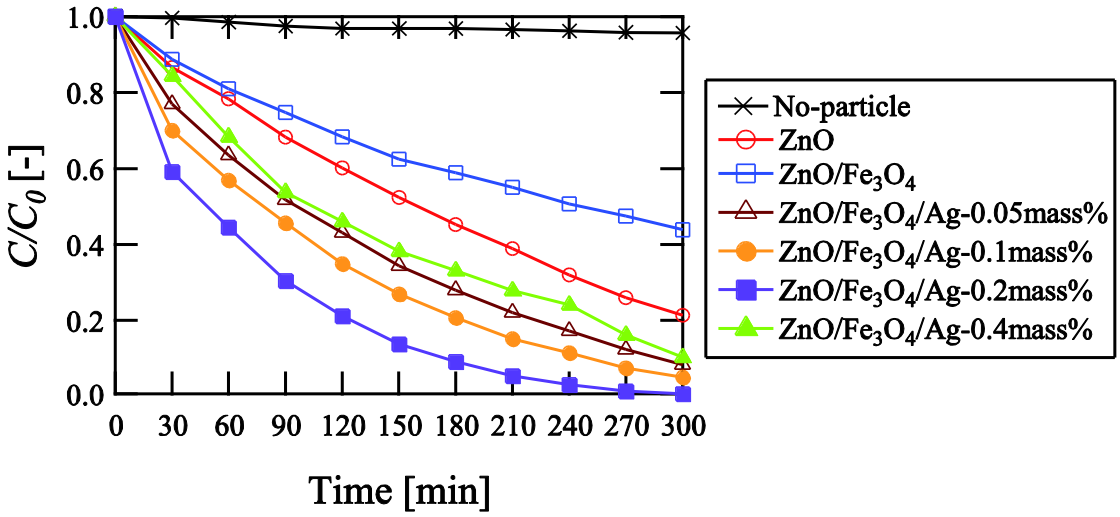

Figure 4-14 Changes in RhB concentration by UV light irradiation time at ZnO, ZnO/Fe_3O_4, and ZnO/Fe_3O_4/Ag generated using co-precipitation method; initial concentration of RhB: 5 mg/L; photocatalyst dose: 15 mg; solution volume: 100 mL.

activity than pure ZnO and ZnO/Fe_3O_4 particles. However, 0.4 mass% of added silver nitrate, shows a decreased photocatalytic activity. Paradoxically, an increase in the amount of supported Ag particles may decrease the photocatalytic activity. Increasing the amount of supported Ag promotes both the separation of electron-hole and the transfer of excited electrons to Ag nanoparticles. However, when excess Ag is supported on ZnO particles, the excess excitons in the Ag nanoparticles accumulate and attract holes. In particular, the excessive supported Ag can promote electron-hole recombination due to the large contact area with ZnO particles. Thus, the number of excitons decreases, leading to a decrease in photocatalytic activity.

Figure 4-15 show the changes in RhB concentration by UV light irradiation time as the sample D dose. In order to know the optimal dose of sample D, which showed the most efficient photolysis, a photolysis experiment was performed by dispersing 5–20 mg of sample D in an aqueous RhB solution. The photocatalytic activity improved as the dose of sample D increased and increased from 5-15 mg in proportion to the amount of sample. However, when 20 mg was dose, the increase in the photolysis rate was insignificant compared to the photolysis rate of 15 mg. It means that an excessive dose of particles increases the turbidity of the suspension and affects photocatalytic activity. That is, the increase in turbidity of the suspension due to excessive dose of the particles may block UV light and hinder the UV light absorption of the photocatalyst.

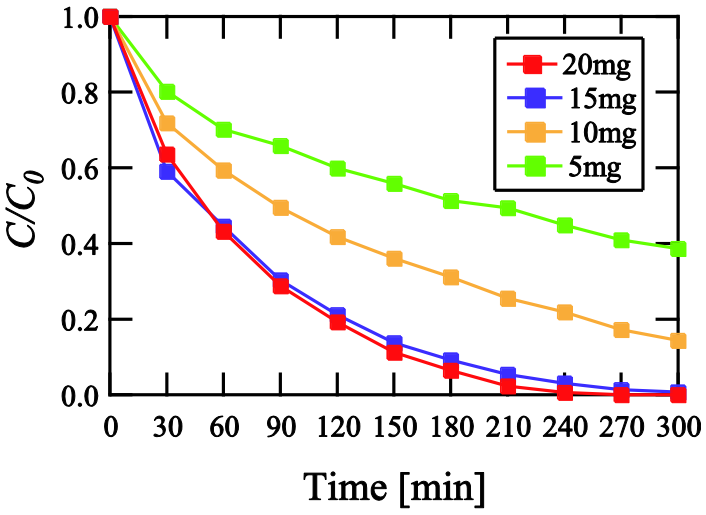

Figure 4-15 Changes in RhB concentration by UV light irradiation time as the sample D dose.

Table 4-3 Comparison of treatment rates by photolysis and recovery rates of Ag/ZnO (USP method) and $ZnO/Fe_3O_4/Ag$ (co-precipitation method) particles; initial concentration of RhB: 5 mg/L; photocatalyst dose: 15 mg; solution volume: 100 mL, dope amount of silver nitrate: 0.2 mass%.

	Ag/ZnO	$Ag/ZnO/Fe_3O_4$
Photolysis time	2h 30min	4h 30min
Particle recovery time	10h	3h 30min
Number of photolysis cycles	5	5
Total time	62h 30min	40h

Table 4-3 compares the treatment rates of Ag/ZnO and $Ag/ZnO/Fe_3O_4$ particles generated by the USP and co-precipitation method. Compared with $Ag/ZnO/Fe_3O_4$ particles generated by the co-precipitation method, the Ag/ZnO particles generated by the USP method had a faster photolysis rate but a slower recovery rate. In particular, the recovery process using magnetism showed a very fast speed compared to gravity sedimentation, and it was found that it was an important factor in the overall treatment rates. As a result, the total photolysis time of $Ag/ZnO/Fe_3O_4$ particles was faster than that of Ag/ZnO particles in the 5th recycling experiment.

4.4. Conclusion

This experiment tried to synthesize ZnO/Fe_3O_4 composite particles using the USP and co-precipitation method under various conditions. When the USP method was used as a single method, the crystal peaks of the target products ZnO and Fe_3O_4 were not observed. The target product was not observed even under oxygen conditions and changes in gas flow rate to establish sufficient thermal decomposition and oxidation conditions. However, under certain conditions, a single crystal peak of $ZnFe_2O_4$ was confirmed. Research on $ZnFe_2O_4$ particles has been reported, but due to the low band gap, it is not suitable for organic matter treatment. The generation of $ZnFe_2O_4$ is related to metal reactivity, and since the metal reactivity of Zn and Fe is similar, it can be precipitated as a single crystal during the pyrolysis process.

When particles were generated using the USP and co-precipitation method together, crystals of the target products, ZnO and Fe_3O_4, were observed. In addition, it was possible to confirm the magnetism

of the generated composite particles. However, large-scale agglomerates were formed due to the agglomeration of the particles, and most of the uncoated ZnO particles were also identified. Therefore, problems of photolysis and secondary pollution may occur. In the photolysis experiment, as the amount of Fe_3O_4 added increased, it was observed that the photolysis properties decreased. Therefore, it was confirmed that the surface modification using sodium citrate is not suitable for the formation of ZnO/Fe_3O_4 composite particles.

When co-precipitation was used as a single method, crystals of the target products ZnO, Ag, and Fe_3O_4 were observed. In the XRD crystal peak, it was difficult to observe the Fe_3O_4 crystal peak due to the overlapping of the ZnO and Fe_3O_4 peaks, but the magnetic experiment showed Fe_3O_4 in the composite particles. Ag particles dispersed in the particles could be confirmed with backscattered electron images. In the photolysis experiment, it was confirmed that the photolysis properties of the ZnO/Fe_3O_4 composite particles were not good compared to the pure ZnO particles. However, although the ZnO/Fe_3O_4/Ag composite particles contained Fe_3O_4, the photodecomposition properties were superior to those of pure ZnO particles. The optimal condition was when 0.2 mass% silver nitrate was added, which is consistent with the results of Chapter 3. The co-precipitation single method confirmed some agglomeration of particles, but it was judged to be most suitable for the generation of ZnO/Fe_3O_4 and ZnO/Fe_3O_4/Ag composite particles.

4.5. Reference

1. J.F. Guo, B. Ma, A. Yin, K. Fan, W.L. Dai, Photodegradation of rhodamine B and 4-chlorophenol using plasmonicphotocatalyst of Ag–AgI/Fe_3O_4@SiO_2magnetic nanoparticle under visible light irradiation, Applied Catalysis B: Environmental, 101 (2011) 580–586.
2. P.G. Tratnyek, R.L. Johnson, Nanotechnologies for environmental cleanup, Nano Today, 1 (2006) 44–48.
3. S.C.N. Tang, I.M.C. Lo, Magnetic nanoparticles: essential factors for sustainable environmental applications, Water Research, 47 (2013) 2613–2632.
4. Y.F. Shen, J. Tang, Z.H. Nie, Y.D. Wang, Y. Ren, L. Zuo, Tailoring size and structural distortion of Fe_3O_4 nanoparticles for the purification of contaminated water, Bioresource Technology, 100 (2009) 4139–4146.
5. R.M. Cornell, U. Schwertmann, The Iron Oxides: Structure, Properties, Reactions, Occurrences

and Uses, 2nd Edition (Wiley-VCH, Weinheim, 2003).

6. R. Dieckmann, Point defects and transport in haematite (Fe_2O_3-ε), Philosophical Magazine A, 68 (1993) 725-745.

7. H. H. Kung, Transition Metal Oxides: Surface Chemistry and Catalysis (Elsevier, New York, 1989).

8. F. Caruso, M. Spasova, A. Susha, M. Giersig, R.A. Caruso, Magnetic Nanocomposite Particles and Hollow Spheres Constructed by a Sequential Layering Approach, Chemistry of Materials, 13 (2001) 109-116.

9. T.G. Hyeon, S.S. Lee, J.N. Park, Y.H. Chung, H B. Na, Synthesis of Highly Crystalline and Monodisperse Maghemite Nanocrystallites without a Size-Selection Process, Journal of the American Chemical Society, 123 (2001) 12798-12801.

10. Y. Xiong, Y. Xie, S. Chen, Z. Li, Fabrication of Self-Supported Patterns of Aligned β-FeOOH Nanowires by a Low-Temperature Solution Reaction, Chemistry—European Journal, 9 (2003) 4991-4996.

11. K. Woo, H.J. Lee, J.P. Ahn, Y.S. Park, Sol–Gel Mediated Synthesis of Fe_2O_3 Nanorods, Advanced Materials. 15 (2003) 1761-1764.

12. Y. Wang, X. Teng, J. Wang, H. Yang, Solvent-Free Atom Transfer Radical Polymerization in the Synthesis of Fe_2O_3@Polystyrene Core−Shell Nanoparticles, Nano Letters, 3 (2003) 789-793.

13. Y.F. Chong, K.L. Pey, A.T.S. Wee, M.O. Thompson, C.H. Tung, A. See, Laser-induced amorphization of silicon during pulsed-laser irradiation of TiN/Ti/polycrystalline silicon/SiO_2/silicon, Applied Physics Letters, 81 (2002) 3768-3788.

14. P. Kumar, H.N. Lee, R. Kumar, Synthesis of phase pure iron oxide polymorphs thin films and their enhanced magnetic properties, Journal of Materials Science: Materials in Electronics, 25 (2014) 4553-4561.

15. M.S. Isiam, J. Kurawaki, Y. Kusumoto, M. Abdulla-Al-Mamun, M.Z. Bin Mukhlish, Hydrothermal Novel Synthesis of Neck-structured Hyperthermia-suitable Magnetic (Fe_3O_4, γ-Fe_2O_3 and α-Fe_2O_3) Nanoparticles, Journal of Scientific Research, 4 (2012) 99-107.

16. M. Helmi-Rashid-Farimani, N. Shahtahmasebi, M. Rezaee Roknabadi, N. Ghows, A. Kazemi, Study of structural and magnetic properties of superparamagnetic Fe_3O_4/SiO_2 core–shell nanocomposites synthesized with hydrophilic citrate-modified Fe_3O_4 seeds via a sol–gel

approach, Physica E, 53 (2013) 207–216.

17. A. Bahari, M. Roeinfard, A. Ramzannezhad, Characteristics of Fe_3O_4/ZnO nanocomposite as a possible gate dielectric of nanoscale transistors in the field of cyborg, Journal of Materials Science: Materials in Electronics, 27 (2016) 9363–9369.
18. R.Y. Hong, S.Z. Zhang, G.Q. Di, H.Z. Li, Y. Zheng, J. Ding, D.G. Wei, Preparation, characterization and application of Fe_3O_4/ZnO core/shell magnetic nanoparticles, Materials Research Bulletin, 43 (2008) 2457–2468.
19. M. Paul, D. Kufer, A. Muller, S. Brück, E. Goering, M. Kamp, J. Verbeeck, H. Tian, G.V. Tendeloo, N.J.C. Ingle, M. Sing, R. Claessen, Fe_3O_4/ZnO : A high-quality magnetic oxide-semiconductor heterostructure by reactive deposition, Applied Physics Letters, 98 (2011) 1–3.
20. D.S. Winatapura, S.H. Dewi, W.A. Adi, Synthesis, Characterization, and Photocatalytic Activity of Fe_3O_4@ZnO Nanocomposite, International Journal of Technology, 3 (2016) 78-85.
21. M. Machovsky, I. Kuritka, Z. Kozakova, Microwave assisted synthesis of nanostructured Fe_3O_4/ZnO microparticles, Materials Letters,86 (2012) 136-138.
22. A. Roychowdhury, S.P. Pati, A.K. Mishra, S. Kumar, D. Das, Journal of Physics and Chemistry of Solids Magnetically addressable fluorescent Fe_3O_4/ZnO nanocomposites : Structural , optical and magnetization studies, Journal of Physics and Chemistry of Solids, 74 (2013) 811-818.
23. A.A. Shal, A. Jafari, Study of Structural and Magnetic Properties of Superparamagnetic Fe_3O_4–ZnO Core–Shell Nanoparticles, J Supercond Nov Magn, 27 (2014) 1531-1538.
24. M. Safari, M.H. Rostami, M. Alizadeh, A. Alizadehbirjandi, S.A.A. Nakhli, R. Aminzadeh, Response surface analysis of photocatalytic degradation of methyl tert-butyl ether by core/shell Fe_3O_4/ZnO nanoparticles, Journal of Environmental Health Sciences & Engineering, 12 (2014) 1-10.
25. R. Strobel, S.E. Pratsinis, Direct synthesis of maghemite, magnetite and wustite nanoparticles by flame spray pyrolysis, Advanced Powder Technology, 20 (2009) 190-194.
26. J.W. Zheng, K.H. Liu, W. Cai, L. Qiao, Y. Ying, W.C. Li, J. Yu, M. Lin, S.L. Che, Effect of chloride ion on crystalline phase transition of iron oxide produced by ultrasonic spray pyrolysis, Advanced Powder Technology, 29 (2018) 1953-1959.
27. A. Kato, F. Tokunaga, Fine Powders by Spray-pyrolysis Technique II. Iron Oxide Powders, Journal of Japanese Society of Powder and Powder Metallurgy, 24 (1977) 219 (in Japanese)

28. T. Nunome, H. Irie, N. Sakamoto, O. Sakurai, K. Shinozaki, H. Suzuki, N. Wakiya, Magnetic and photocatalytic properties of n- and p-type $ZnFe_2O_4$ particles synthesized using ultrasonic spray pyrolysis, Journal of the Ceramic Society of Japan, 121 (2013) 26-30.

29. M.A. Valenzuela, P. Bosch, J. Jiménez-Becerrill, O. Quiroz, A.I. Páez, Preparation, characterization and photocatalytic activity of ZnO, Fe_2O_3 and $ZnFe_2O_4$, Journal of Photochemistry and Photobiology A: Chemistry, 148 (2002) 177-182.

Chapter 5 Conclusions

Existing wastewater treatment methods such as adsorption, filtration, coagulation, membranes, etc. have a problem in that pollutants cannot be decomposed, and organic pollutant molecules are simply transferred to another medium to cause secondary pollution. Therefore, in this study, the photocatalyst ZnO was studied for the oxidation treatment of organic dyes. However, the main drawbacks of ZnO are that the efficiency decreases due to the rapid recombination of the excited electron-hole pairs, and the recovery of the photocatalyst after photolysis treatment is very difficult and reuse is greatly limited. In order to compensate for the shortcomings of ZnO, a study on the loading of Au and Ag, which acts as an electron sink, and the complexation of Fe_3O_4 were conducted.

In Chapter 2-3, Ag/ZnO and Au/ZnO particles were generated using the USP method. All particles were spherical and the size of between 0.5 μm and 1.0 μm, and there was no change in shape due to the support of Ag and Au. In all of the generated particles, crystal peaks of Ag or Au were observed along with a crystal peak of ZnO. TEM images showed dark spots scattered throughout the Au/ZnO and Ag/ZnO particles. EDX mapping and STEM images confirmed that these dark spots correspond to Ag or Au nanoparticles dispersed throughout the ZnO particles.

The photocatalytic activity of the resulting particles was investigated by photolysis of the aqueous RhB solution under UV irradiation. All Au/ZnO and Ag/ZnO particles showed higher photocatalytic activity than pure ZnO particles. In addition, Au/ZnO particles supporting 0.1 mass% $HAuCl_4$ had a photolysis rate constant about 4 times higher than that of pure ZnO particles, and Au/ZnO particles supporting 0.2 mass% $AgNO_3$ were about 8 times higher than that of pure ZnO particles. And interestingly, some particles showed better photolysis activity than P25. However, when $HAuCl_4$ and $AgNO_3$ were supported by 0.2 mass% and 0.4 mass %, respectively, the photocatalytic activity was greatly reduced. That is, as the amount of Au and Ag increased, the photodecomposition activity increased, but when the noble metal nanoparticles were excessively supported, the photocatalytic activity decreased. It is thought that this is because if excess Au or Ag nanoparticles are supported on ZnO, excessive excitation electrons are accumulated and recombination of electron-holes is promoted by electrostatic attraction.

In order to investigate the optimal dose required for photolysis, photolysis experiments were performed with various doses. The photocatalytic activity of both Au/ZnO and Ag/ZnO particles

increased in proportion to the dose from 2 mg to 10 mg, but did not change significantly at higher doses. This is because the ultraviolet rays, which are important for electronic excitation, have been blocked by the cloudy suspension. It also confirmed the reusability of Ag/ZnO particles for commercial applications. It was observed that the generated particles could not only be recovered by gravity precipitation after photolysis experiments, but also had a slow deterioration rate. Decomposition experiments on actual wastewater were outside the scope of this study, but the possibility of using this material to purify organic pollutants was confirmed.

In Chapter 4, the synthesis of ZnO/Fe_3O_4 composite particles was attempted by using USP and coprecipitation method for simple recovery of magnetic particles. When the USP method was used as a single method, crystal peaks of the target products ZnO and Fe_3O_4 were not observed, and only crystal peaks of $ZnFe_2O_4$ were observed. When particles were generated using the USP and coprecipitation method along with surface modification using sodium citrate, crystals of the target products, ZnO and Fe_3O_4, were observed, and the magnetic properties of the particles were confirmed. However, agglomeration of most of the uncoated ZnO particles and particles was observed. When the coprecipitation method was used as a single method, crystals of the target products ZnO, Ag, and Fe3O4 were observed. In the photolysis experiment, it was confirmed that the photolysis properties of the ZnO/Fe_3O_4 composite particles were not as good as those of pure ZnO particles. However, the ZnO/Fe_3O_4/Ag composite particles contain Fe_3O_4, but the photolysis properties were superior to those of pure ZnO particles. Therefore, the ZnO/Fe_3O_4/Ag composite particles produced by the co-precipitation method can be considered as a promising material for organic dye treatment.

APPENDIX

Nomenclature

C_0	initial concentration of the RhB	[mg/L]
$C_{Zn(NO_3)_2\,aq.}$	raw material concentration	[g/L]
$D_{droplet}$	droplet size	[µm]
D_{ZnO}	ZnO particle diameter	[m]
f	frequency of the ultrasonic transducer	[MHz]
k	rate constant	[min^{-1}]
$MW_{Zn(NO_3)_2}$	molecular weight of zinc nitrate	[kg/kmol]
MW_{ZnO}	molecular weight of ZnO	[kg/kmol]
$O_2 \bullet^-$	superoxide radical anions	[-]
$\bullet OH$	hydroxyl radicals	[-]
ρ_{ZnO}	density of ZnO	[kg/m^3]
t	time	[min]
ρ	density of the solution	[kg/m^3]
γ	surface tension of the solution	[N/m]
R^2	Coefficient of determination	[-]

List of Figures

Chapter 1

Chapter 2

Chapter 3

Chapter 4

particles generated using co-precipitation method.

Figure 4-14 Changes in RhB concentration by UV light irradiation time at ZnO, ZnO/Fe_3O_4, and ZnO/Fe_3O_4/Ag generated using co-precipitation method; initial concentration of RhB: 5 mg/L; photocatalyst dose: 15 mg; solution volume: 100 mL.

Figure 4-15 Changes in RhB concentration by UV light irradiation time as the sample D dose.

List of Tables

Chapter 1

Chapter 2

Chapter 3

Chapter 4

Table 4-2 Experimental parameters of the ZnO/Fe_3O_4 and $ZnO/Fe_3O_4/Ag$ composite particles by co-precipitation method.

Table 4-3 Comparison of treatment rates by photolysis and recovery rates of Ag/ZnO (USP method) and $ZnO/Fe_3O_4/Ag$ (co-precipitation method) particles; initial concentration of RhB: 5 mg/L; photocatalyst dose: 15 mg; solution volume: 100 mL, dope amount of silver nitrate: 0.2 mass%.

Acknowledgment

I would like to express my sincere gratitude to my supervisor, Associate Professor Toshiyuki Fujimoto, for continuing to support my doctorate with his research knowledge and advice. In addition to his extensive research knowledge, I was able to learn persistence, perseverance, Japanese culture, insight, etc., which made my Ph.D. study in his laboratory unforgettable and very meaningful. Above all, his guidance through seminars and discussions in the laboratory helped me a lot in researching and solving this thesis.

Sincere thanks to my thesis committee members, Professor Hideyuki Nakano and Associate Professor Shinya Yamanaka. Their advice and insightful questions allowed me to think about my research from more diverse perspectives and improved the quality of my research. And I would like to thank Professor Takafumi Seto, who gave me a lot of advice during my internship period at Kanazawa University. Without his consideration, I would not have been able to do my internship during these very difficult times due to COVID-19. Also, I would like to express my sincere gratitude to the kindness and courtesy of the people involved in the research lab at Kanazawa University.

I would also like to thank all members of the Aerosol Chemical Engineering Lab. First of all, I would like to thank Watanuki, who was my tutor and classmate. Her kindness helped me adjust to the lab and sometimes taught me Japanese. I also would would like to express my gratitude to my lab juniors, Hashimoto, Takahashi, and Kawashima. Takoyaki, nabe, curry, and Christmas parties in the laboratory became great memories during my life of studying abroad.

I would like to sincerely thank my seniors Wonsig Jin and Juhyeon Yu for recommending me to study abroad and for always giving me advice. They always gave me a lot of advice through my study abroad experience and helped me to finish my study abroad life successfully. And I am also grateful to my graduate school classmate and friend Jongil Kim. He is my drinking buddy, and because of him, we were able to finish our difficult study abroad life together.

Finally, I am especially grateful to my family for supporting me during this long and sometimes difficult journey. Although there were many difficult times during my study abroad life, graduation would not have been possible without their encouragement and love. And I am really grateful to my late grandmother who loved me and always supported me in my study abroad life. I am really grateful

to everyone who supported me during my study abroad life.

***Muroran, September* 2021**

Youngjun Lee